Progress in Polymer Science 48 (2015) 111–121

Contents lists available at ScienceDirect

Progress in Polymer Science

journal homepage: www.elsevier.com/locate/ppolysci

Conformation–function relationships for the comb-shaped polymer pOEGMA

Mi Liu[a], Jean-Christophe Leroux[a], Marc A. Gauthier[b,*]

[a] Swiss Federal Institute of Technology Zurich (ETHZ), Department of Chemistry and Applied Biosciences, Institute of Pharmaceutical Sciences, Vladimir-Prelog-Weg 1–5/10, 8093 Zurich, Switzerland
[b] Institut National de la Recherche Scientifique (INRS), 1650 boul. Lionel-Boulet, Varennes, QC, Canada J3X 1S2

ARTICLE INFO

Article history:
Available online 30 April 2015

Keywords:
Thermosensitivity
LCST
Non-fouling
Bio-conjugate
PEGylation
pOEGMA

ABSTRACT

Poly(oligo(ethylene glycol) methyl ether methacrylate) (pOEGMA) is a highly versatile polymer because manipulation of the dimensions of its comb-type structure has a predictable effect on the conformation of its main-chain and side-chains which can, together or independently, be either extended or collapsed. This control, and the distinctive physical–chemical characteristics of pOEGMA, are the common driving forces behind its tunable thermosensitivity properties, supramolecular assembly characteristics, and efficient protein repellency. Because of these interesting properties, pOEGMA is increasingly being used within functional coatings, biosensors, drug delivery systems, biomaterials, etc. This Trend article highlights the how to control (and factors influencing) pOEGMA main/side-chain conformations, and consequently exploit this polymer in several emerging areas of importance. This discussion integrates all current areas of application (i.e., in solution, within complex (bio)conjugates, and grafted to solids), in order to provide a common and general perspective on how this polymer can be most efficiently used in future applications.

Contents

Abbreviations: ATRP, atom transfer radical polymerization; DMAEMA, *N*,*N*-dimethylaminoethyl methacrylate; DNA, deoxyribonucleic acid; LCST, lower critical solution temperature; PBIEM, poly(2-(2-bromoisobutyroyloxy)ethyl methacrylate); PBPEM, poly(2-(2-bromopropionyloxy)ethyl methacrylate); pOEGMA, poly((oligo(ethylene glycol) methyl ether methacrylate); RNA, ribonucleic acid; UCST, upper critical solution temperature.

* Corresponding author.
E-mail address: gauthier@emt.inrs.ca (M.A. Gauthier).

http://dx.doi.org/10.1016/j.progpolymsci.2015.03.001
0079-6700/

1. Introduction

Since the first reports of the controlled synthesis of poly(oligo(ethylene glycol) methyl ether methacrylate) (pOEGMA), starting in the 1990s [1–5], and the discovery of its thermosensitivity and protein-repellant properties in the early 2000s [6,7], interest in pOEGMA from both the polymer and biotech communities has continued to gain momentum [8–16]. With the convenience of a number of modern controlled/"living" polymerization techniques [17–21], as well as the commercial availability of a number of OEGMA monomers, well-defined homo- and co-polymers of pOEGMA are easily accessible (Fig. 1a) [13,22]. Additionally, the polymerization reaction can take place in aqueous media which enables interfacing with biomaterials [12,21,23], and pOEGMA can be directly grown from initiator-functionalized (bio)macromolecules and solid substrates, providing access to bio-hybrid materials relevant for a variety of sectors [17,18,21,23,24].

From a physical–chemical standpoint, this comb-shaped polymer is particular because its backbone is hydrophobic and its side-chains are amphiphilic (Fig. 1a). Modifying side-chain length alters hydrophilicity, which can in turn influence hydration state and conformation, at a given temperature. This phenomenon has formed the basis for a number of comprehensive reviews discussing how the molecular dimensions of pOEGMA influence its thermoresponsive properties in solution and within (bio)materials [9,14–16]. In addition, the relative lengths of the main- versus side-chains can affect the conformation of the main-chain, because of repulsion between the potentially long side-chains (i.e., steric effect). Despite being known for other comb-shaped polymers, this second phenomenon has been rarely been discussed for pOEGMA [25] (or other oligo(ethylene glycol) side-chain polymers) [26], and has only recently started to receive attention as a design parameter for tuning the properties of functional biomaterials [27,28]. The purpose of this trend article is to highlight how pOEGMA side- and main-chain conformations can (together or separately) be manipulated, what factors affect them, and how this control can be used to exploit this polymer in three emerging areas of importance (Fig. 1b). This contribution therefore successively discusses the thermosensitivity of pOEGMA in aqueous and alcohol solutions, pOEGMA-guided supramolecular assembly, and the protein-repellant properties of pOEGMA when grafted to solid substrates and to (bio)macromolecules. For simplicity, the term "pOEGMA" is used irrespectively of nature of the main-chain (i.e., acrylate or methacrylate) or the termini of the side-chains (i.e., hydroxyl, methyl ether, etc.). When the polymer differs specifically from poly(oligo(ethylene glycol) methyl ether methacrylate), the relevant differences are mentioned in the text.

2. Solution thermosensitivity

2.1. Thermosensitivity in aqueous solution

The most widely advertised solution property of pOEGMA is its thermosensitivity, as first described by Han et al. [6] At low temperature, pOEGMA is soluble in water due to the hydration of its side-chains. However, with increasing temperature, the latter dehydrate which causes them to collapse, leading to polymer aggregation and ultimately precipitation. The temperature at which this process begins is referred to as the lower critical solution temperature (LCST) [8,10]. The transition from soluble-to-insoluble, termed a cloud-point when measured by turbidimetry, is sharp, reversible, and displays little hysteresis. Narrow molecular weight P2 and P3 showed that cloud-points decreased slightly (~2 °C) with increasing total molecular weight. Higher molecular weight polymers showed sharper transitions, suggesting that the longer polymer chains more easily form inter-molecular and/or intra-molecular entanglements that promote more rapid aggregation, and thus phase separation. Polymer stereoregularity only had a small effect on cloud-point. It should be noted that because turbidity measurements rely on inter-molecular aggregation, cloud-points can differ from the LCST, the thermodynamic temperature at which phase change occurs. Ishizone et al. [29] showed a clear relationship between the side-chain length and the cloud-point of P2, P3, P4 prepared by anionic polymerization. Further increasing the side-chain length raises the cloud-point, and the highest reported values are for P9, which has a cloud-point at around 90 °C [30]. Using automated parallel synthesis, Becer et al. [31] synthesized a library of pOEGMA homo-polymers and confirmed within this very large parameter space that main-chain length had only a slight effect on cloud-point, while the effect of side-chain length was large. It is straightforward to prepare pOEGMA displaying thermosensitivity over a large temperature range. However, owing to the insensitivity of LCST to main-chain length, it is difficult to finely adjust the cloud-point around the value intrinsically dictated by side-chain length.

2.2. Influence of chemical alteration on thermosensitivity in aqueous solution

Chemical modification of the pOEGMA platform has been investigated as a means of addressing this

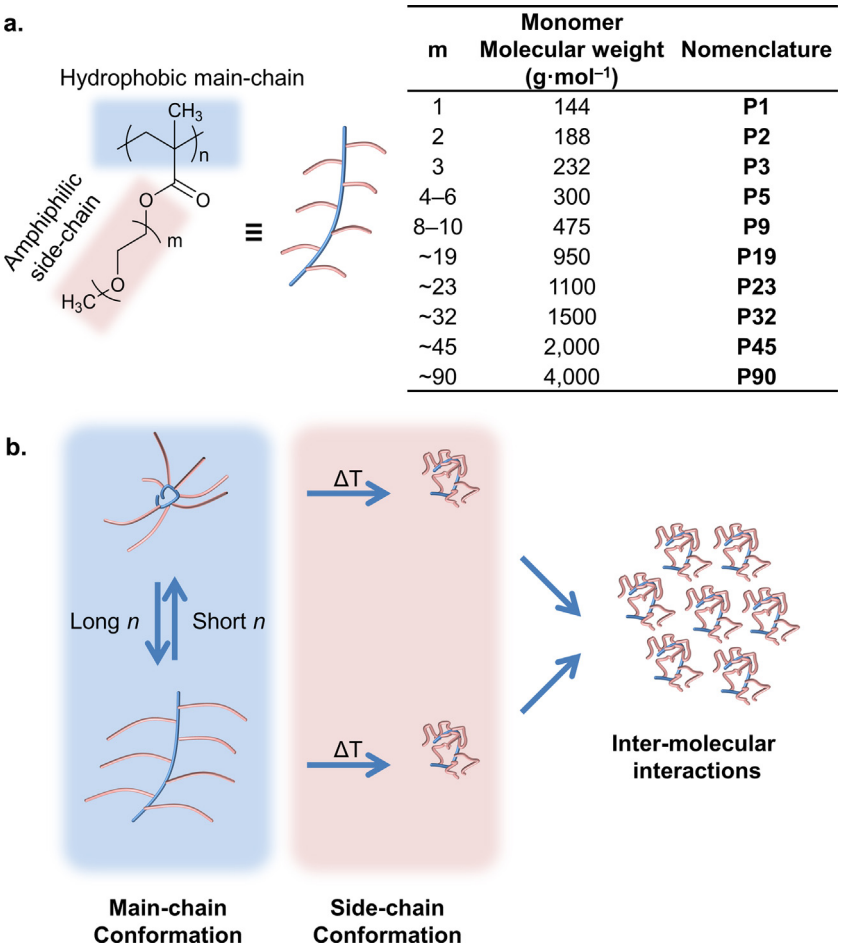

m	Monomer Molecular weight ($g \cdot mol^{-1}$)	Nomenclature
1	144	**P1**
2	188	**P2**
3	232	**P3**
4–6	300	**P5**
8–10	475	**P9**
~19	950	**P19**
~23	1100	**P23**
~32	1500	**P32**
~45	2,000	**P45**
~90	4,000	**P90**

Fig. 1. Structure of pOEGMA and illustration of its extended and collapsed conformations. (a) Chemical structure of pOEGMA, nomenclature, and selected commercially-available monomers discussed herein. (b) The molecular dimensions of pOEGMA influence the conformation of the main-chain, due to steric repulsion between the side-chains. External factors, such as temperature, influence side-chain conformation and consequently solution properties, supramolecular assembly, etc.

challenge. For instance, replacing the terminal methyl group on the side-chain by an ethyl reduced the cloud-points of the polymers by 20–25 °C because of the lower expected hydration of the side-chain [29,31]. Furthermore, alteration of both the α- and ω-termini of the main-chain had a substantial effect on thermosensitivity. For instance, Roth et al. [32] systematically modified both termini of P5 (3 kDa), which modulated its cloud-point over a 20 °C range. Hydrophobic groups at either end of the polymer main-chain depressed the cloud-point, and this effect was additive for modification at both ends. Charged groups increased the cloud-point and could compensate for the effect of hydrophobic groups at the other end. Similar observations were made by Soeriyadi et al. [24] This effect, however, was observed for short polymers and it is reasonable to assume that it may become negligible once the main-chain increases beyond a certain length, though this remains to be validated. Other means of altering this parameter are necessary.

2.3. Co-monomer composition

An important development in this area came from the work of Lutz and Hoth [33] in 2006 by establishing that the cloud-point of pOEGMA could be predictably altered by statistical co-polymerization of monomers with different side-chain lengths. For instance, while P2 and P9 exhibit cloud-points of 26 and ~90 °C, respectively, the cloud-points of P2-stat-P9 (i.e., statistical co-polymers of P2 and P9) were between the aforementioned limits and scaled linearly with co-monomer composition (Fig. 2a). In 2008, Yamamoto et al. [34] prepared statistical copolymers of P2 and P3 by atom transfer radical polymerization (ATRP) and observed that the LCST of the co-polymers increased with the mole fraction of P3 from 26 °C to 52 °C. Furthermore, the LCST of corresponding block copolymers shifted towards the LCST of the major segment, compared to the value measured for the statistical copolymers of same composition. The cloud-points of P2-stat-P3 produced by anionic

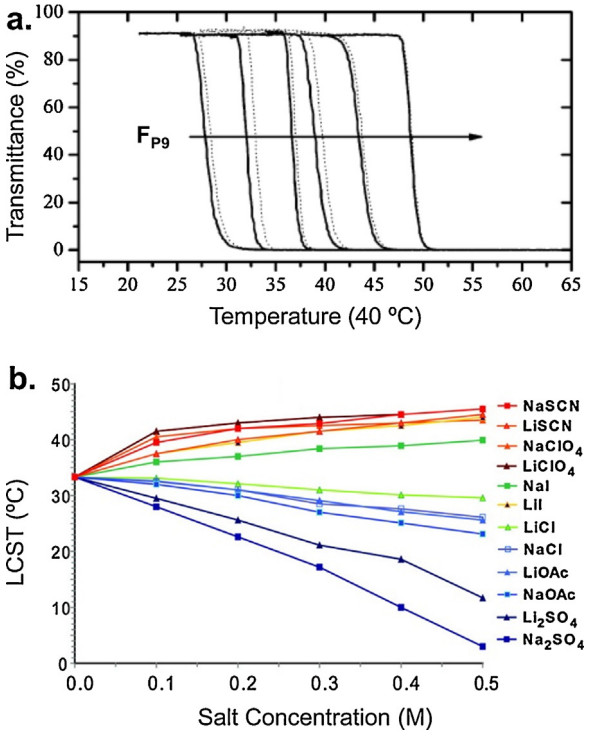

Fig. 2. Tunable thermosensitivity of pOEGMA. (a) Plots of transmittance as a function of temperature (670 nm, 1 °C min^{-1}) measured for aqueous solutions (3 mg mL^{-1}) of a series of P2-stat-P9 co-polymers with increasing P9 content (F_{P9} in the figure). Solid lines: heating cycles, dotted lines: cooling cycles.[33] (b) Influence of the concentration of Li+ and Na+ salts of Hofmeister series ions on the LCST of P3 [36]. Sources: [33,36], Copyright 2006, 2008, respectively. Sources: Adapted with permission from the American Chemical Society.

polymerization also showed similar behavior, pointing to the general nature of the phenomenon within the pOEGMA family [29]. With the new ability to finely tune the thermosensitivity of pOEGMA around 37 °C, interest has emerged in using this polymer in biomedical applications. In line with this, the influence of a number of relevant external factors on the LCST of pOEGMA have been investigated such as concentration and salts. Between 1 and 10 g L^{-1} in water, pOEGMA concentration was shown to not exert a very large influence on LCST [35]. For instance, a decrease of concentration from 5 to 0.5 g L^{-1} increased the LCSTs of P2, P3, P5, P9, and P2-stat-P9 by only ~6 °C [8]. Furthermore, the cloud-point of P2-stat-P9 exhibited a salting-out effect when the concentration of sodium chloride was increased from 0 to 11 g L^{-1} due to partial dehydration of the macromolecules [35]. A ~4 °C depression of the cloud-point was observed within this salt concentration range, and a depression of the LCST of ~3 °C was also observed between pure water and physiological salt concentrations. In addition, cloud-points in bovine plasma were 2 °C lower than in phosphate buffered saline, possibly indicating the involvement of serum proteins in the phase transition [8]. Magnusson et al. [36] screened the influence of several salts of the Hofmeister series (a classification of ions known for their ability to salt-in or -out proteins) on the thermosensitivity of pOEGMA co-polymers. Very strong changes in cloud-points were observed for strong chaotropes such as NaSCN, which increased their values, and for kosmotropes such as Na_2SO_4, which lowered them (Fig. 2b). In fact, Na_2SO_4 altered the turbidity curve from a one-step process in water (or NaCl) to a two-step one. The authors attributed this phenomenon to the sulfate ions altering the association state of the co-polymers, though the precise mechanism remains to be established.

2.4. Complex structures

It is interesting to note that the observations made in the preceding paragraph have been used to guide the design of more complex thermoresponsive systems. For instance, when P2 was cross-linked to form a microgel, the latter displayed a volume transition temperature which was identical to the LCST of P2 homo-polymer. This suggests an insensitivity of LCST towards the molecular weight between cross-links, at least within the examined range [37]. In contrast, Dong et al. [38] observed that the comparable transition temperature of a more hydrophilic microgel, composed of P2-stat-P5, was slightly lower than the LCST of a linear polymer of similar composition. The authors attribute this finding to the relatively greater hydrophobicity of the cross-link compared to the specific pOEGMA employed.

Bebis et al. [8] observed that the cloud-point of a bioconjugate composed of two P2-stat-P3 chains conjugated to salmon calcitonin was higher than that of the equivalent unconjugated polymer. This shift was attributed to the small protein behaving as a hydrophilic end-group. Liu et al. [28] have evaluated the thermosensitivity of a library of pOEGMA-α-chymotrypsin conjugates. The lack of influence of main-chain length and strong effect of side-chain length were obvious features of this dataset (Fig. 3a). In addition, increasing grafting density of P9 from two to twelve pOEGMA chains per protein lead to an strong depression of the cloud-point by ~20 °C (Fig. 3b), which the authors relate to a high local concentration of pOEGMA [8]. High local pOEGMA concentration increases the probability of adjacent pOEGMA chains interacting and initiating an aggregation process. When grafted to the hydrophobic polymer poly(arylene oxindole), the cloud-point of either P2 or P2-stat-P5 decreased, in line with the hydrophobicity of this polymer [39]. Contrary to the trends above, Mertoglu et al. [30] observed that the assembly of P9-block-poly(*n*-butyl acrylate) into polymeric micelles caused a shift of the cloud-point of the P9 segment from 83 to 93 °C, as measured by dynamic light scattering. This discordant observation was rationalized to result from the confinement of pOEGMA in the polymeric shell, which hinders its collapse.

Because of the versatility of ATRP, pOEGMA can also be incorporated into substantially more architecturally-complex structures by synthesis from well-defined multifunctional macro-initiators, thereby producing so-called "bottlebrush" or double-branched architectures [40–43]. Yamamoto et al. [44] have performed a detailed investigation of the temperature-responsiveness of such bottlebrush polymers composed of pOEGMA homo-/co-polymers grafted to poly(2-(2-bromoisobutyryloxy)ethyl

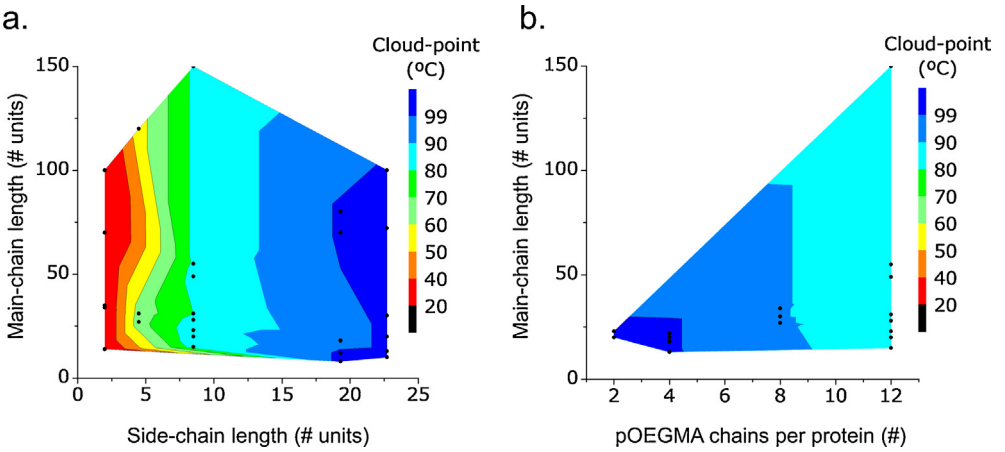

Fig. 3. Thermosensitivity of a library of pOEGMA–protein conjugates. (a) The cloud-point of the conjugates decreased with increasing side-chain length, though was largely insensitive to main-chain length. The conjugates all possess 12 pOEGMA chains per protein. (b) The cloud-points of P9–protein conjugates decreased with grafting density. Color maps established as linear projections between data-points (black dots are the mean of $n = 3$). [28], Copyright 2015. Adapted with permission from John Wiley & Sons Inc.

methacrylate) (PBIEM) (Fig. 4a). P2-graft-PBIEM bottlebrushes displayed a soluble-to-insoluble transition at 22 °C, which was slightly lower than expected for the comparable linear P2 (26 °C). Increasing the molecular weight of P2 within the bottlebrush did not significantly change the temperature at which the transition occurred, though generated a hysteresis between the heating and cooling cycles. The authors attributed this phenomenon to the P2 grafts not efficiently disaggregating close to the PBIEM backbone due to steric hindrance. When P2 was replaced by P2-stat-P3, a similar hysteresis was observed, and the LCSTs were comparable to those reported for linear pOEGMA analogs of similar composition. When the statistical pOEGMA segments were altered to block structures, interesting properties were observed. For P2-block-P3 (P2 is closer to PBIEM core), a cloud-point of ~50 °C was observed. This suggests that when P2 is the inner segment of the block co-polymer, its collapse upon heating does not cause de-solvation of the entire bottlebrush because the outer P3 block remains hydrated (Fig. 4b). In contrast, P3-block-P2 (P3 closer to PBIEM core) started to cloud at 26 °C (the LCST of the P2 block) and transmittance displayed a plateau until 40 °C, at which point transmittance decreased rapidly. Analysis by dynamic light scattering suggested that collapse of the outer P2 block yielded a shell-like structure, ultimately leading to intermolecular aggregation at higher temperature.

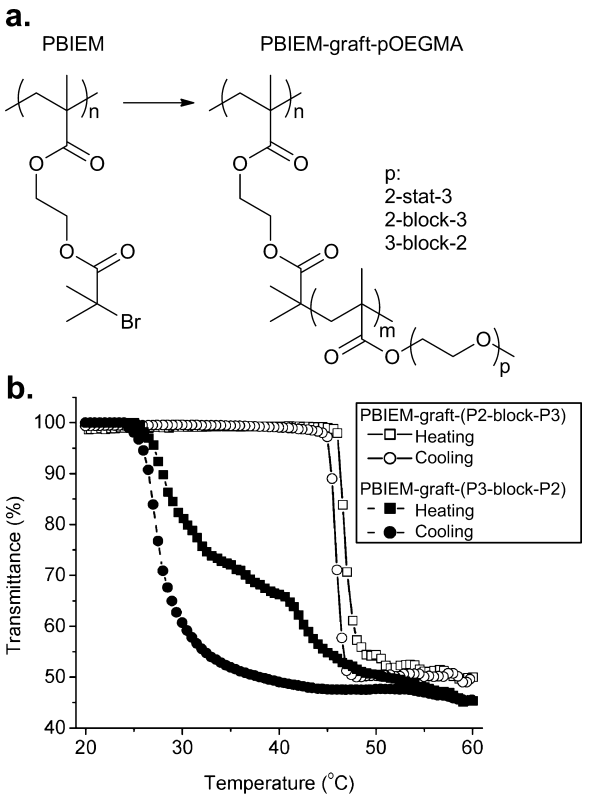

Fig. 4. Synthesis and thermosensitivity of pOEGMA bottlebrushes. (a) pOEGMA bottlebrushes can be prepared by ATRP of OEGMA from a multifunctional macro-initiator such as PBIEM. (b) The structure of the block pOEGMA grafts influences when the soluble-to-insoluble transition occurs. [44], Copyright 2007. Adapted with permission from the American Chemical Society.

2.5. Thermosensitivity in alcohol

In addition to displaying thermosensitivity in aqueous media, pOEGMA also exhibits an upper critical solution temperature (UCST) in both polar water-miscible alcohols (e.g., ethanol) as well as in non-polar alcohols (e.g., dodecanol). The UCST is defined as the critical temperature below which pOEGMA collapses onto itself and ultimately aggregates and precipitates. A linear dependence was observed between the UCST and the number of carbons in 1-alkanol solvents. The soluble-to-insoluble transition measured by turbidimetry, also referred to as a cloud-point as above, and associated with the UCST is sharp and reversible. However, the molecular parameters of pOEGMA that influence this transition are different.

For instance, the cloud-point of P5 in isopropanol was found to increase with molecular weight from 12.3 °C (5.4 kDa) to 35.6 °C (23.2 kDa), which contrasts to the insensitivity of the LCST to this parameter in aqueous media [45]. Functional groups appended to the α- and ω-termini altered the UCST of 5.4 kDa pOEGMA between −6.7 °C and 15.1 °C, depending on the chemical nature of the end groups. Trends are unclear and were sometimes different than those established for the LCST. Analysis of the UCST transition by proton nuclear magnetic resonance spectroscopy between 30 and 0 °C indicated a gradual collapse of the side-chains onto the main-chain, beginning at the ester linkage [46]. Polymer de-solvation was found to be a material property and thus independent of concentration, though macroscopic phase separation, which involves inter-chain aggregation was strongly dependent on concentration (UCST increased with increasing concentration).

3. Supramolecular assembly

As seen in the preceding section, the soluble-to-insoluble transition of pOEGMA is a reliable and tunable process. Interestingly, this transition can be exploited to guide the self-assembly of either itself or other moieties into supramolecular structures. Lutz et al. [47] have characterized this phenomenon for P2-stat-P9 by proton nuclear magnetic resonance spectroscopy and dynamic light scattering measurements. The authors observed that, shortly after dehydration, the collapsed macromolecules rearrange by collision into stable mesoglobules. These nanoparticles composed entirely of pOEGMA are stabilized by weak intermolecular associations and re-dissolve readily upon cooling without any noticeable hysteresis. Slow gradual heating through the LCST produced large mesoglobules (100–1000 nm), while smaller ones with narrow size distributions were obtained when the solutions were heated abruptly [48]. Larger mesoglobules were formed at higher concentration, though no clear trend between diameter and pOEGMA composition was observed. In complementary work, Hussain et al. [49] studied the micellization behavior of P9 and P23 below the LCST. The critical aggregation concentration in water depended on the length of the side-chain, but not on the overall molecular weight of the polymer. The hydrodynamic radius of the micelles did not depend on polymer concentration, suggesting that the micelles formed via the closed association model. While micelles of P9 were insensitive to heating, those formed with P23 shrank slightly between 25 and 60 °C. In an interesting example, Trzcinska et al. [50] showed that heating a solution of P2 bearing a terminal hydrophilic pentapeptide unit resulted in the formation of spherical mesoglobules. The sizes of the aggregates were easily controlled by changing the concentration and heating rate. The peptides were fully accessible to enzymatic digestion, indicating that they formed the external shell of the mesoglobule.

In addition to guiding its own self-assembly, the phase separation of pOEGMA has been used to drive the self-assembly of more complex systems, including other polymers and inorganic nanoparticles. For instance, Roth et al. [46,51] have reported the formation of hydrophilic-core micelles from block co-polymers

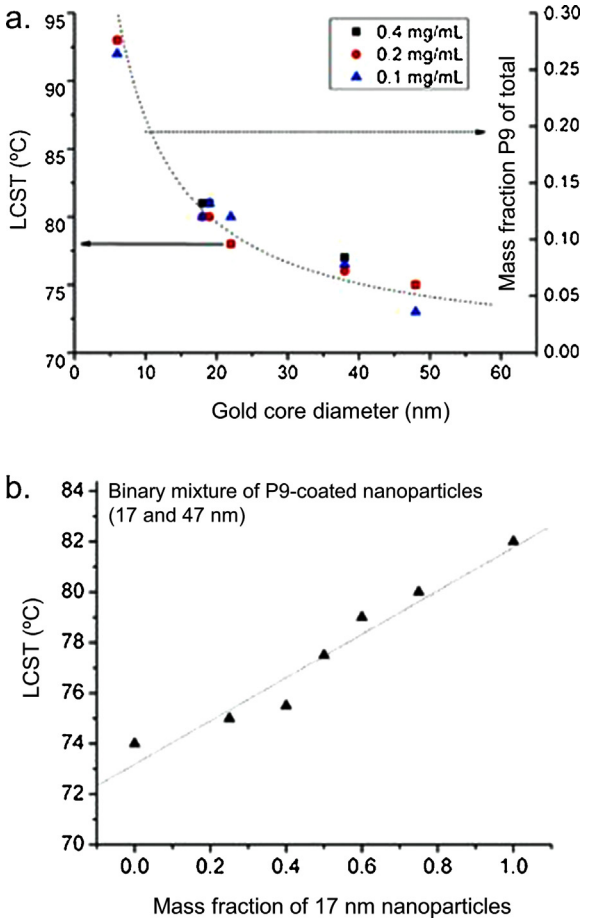

Fig. 5. Supramolecular assembly induced by pOEGMA. (a) The LCSTs of P9-coated gold nanoparticles decreases with gold core diameter. (b) Variation of the LCST of binary mixtures of P9-coated 17 nm gold nanoparticles and P9-coated 47 nm gold nanoparticles. A single LCST was observed between the values observed for either nanoparticle alone. This LCST scaled linearly with the composition of the binary mixture. [53], Copyright 2010. Adapted with permission from John Wiley & Sons Inc.

of P5 and either poly(*N*-isopropylacrylamide), poly(*N*,*N*-diethylacrylamide), or poly(pentafluorophenyl acrylate) in isopropanol by cooling below the UCST. In the latter case, cross-linking of the shell led to a system that could be transferred into water while maintaining its hydrophilic core. In contrast, in aqueous media, the size of polymer micelles formed from P5-block-peptide-block-poly(*N*-isopropylacrylamide) was influenced by the pOEGMA segment [52]. Increasing P5 main-chain length led to a larger surface area requirement per polymer chain, and thus to a smaller micelle size. Addition of salt partially dehydrated pOEGMA, which subsequently changed the aspect ratio of the polymer and lead to an increased micelle size. In an elegant example of the influence of the supramolecular assembly characteristics of pOEGMA on the assembly of gold nanoparticles, Gibson et al. [53] demonstrated that the LCST of P9 could be controlled by the size of the gold nanoparticles onto which it was grafted (Fig. 5a). The authors suggested that this could be related to the fact that the ratio of polymer to gold is greater

for smaller particles. The latter could potentially influence local concentration, a parameter known to impact the cloud-point in solution, as seen above. Interestingly, they showed that binary mixtures of pOEGMA-coated gold nanoparticles, each with distinct LCSTs, exhibited cooperative thermosensitivity and a single LCST that could be fine-tuned by adjusting the weight fraction of the constituent nanoparticles (Fig. 5b). This phenomenon was exploited to selectively capture and bind pOEGMA-coated nanoparticles to a surface modified with a complementary pOEGMA brush. Selective assembly was achieved at a temperature above the LCST of the surface, but below the LCST of the nanoparticles in solution.

Neugebauer et al. [54] have examined the bulk properties of P5 and P23, as well as bottlebrushes prepared by grafting P5 or P23 from a well-defined multifunctional macroinitiator poly(2-(2-bromopropionyloxy)ethyl methacrylate) (PBPEM). Bulk P5 was amorphous while bulk P23 was crystalline. The corresponding bottlebrushes displayed similar characteristics, with the added observation that shorter P23 grafts produced a better developed crystalline structure. The modulus of these materials was strongly dependent on the architecture of the bottlebrush. Cross-linking resulted in the formation of elastomers that were very soft ($G' \sim 10^4$ Pa) in comparison to conventional networks.

4. Non-fouling

4.1. Shielding of bulk solids

After thermosensitivity, the second most investigated property of pOEGMA lies in its ability to effectively repel protein adsorption. This property has been exploited to impart so-called "non-fouling" properties to a variety of substrates, including inorganic solids, biomolecules, etc. The influence of the molecular structure of pOEGMA on its non-fouling properties has been most thoroughly characterized in the form of non-fouling coatings, or "brushes", for bulk solid substrates. Ma et al. [7] first reported that a 15-nm thick P9 brush grown directly from the surface of gold displayed very low protein adsorption. Since this report, a number of additional inorganic solids, including silicon(1 0 0), gold, mesoporous silica, silicon oxide, cellulose paper, etc., have been protected with pOEGMA brushes [55–63]. In a systematic evaluation of the molecular parameters of pOEGMA influencing non-fouling, Ma et al. [25] made the interesting observation that the conformation of the main-chain changed from a collapsed to an extended state above a certain main-chain length. This manifested itself during synthesis as brush thickness growing more rapidly at longer polymerization times (Fig. 6a) because, after the transition from collapsed to extended, the active ω-terminus of pOEGMA is projected away from the surface, where it reacted more quickly. Indeed, it is known for other comb polymers that when the main-chain is short compared to the side-chain, repulsion between the side-chains causes them to project in 3D, producing an ellipsoidal shape in solution. Once the main-chain is of sufficient length, it becomes extended, yielding a (potentially flexible) cylindrical structure. These conformational changes

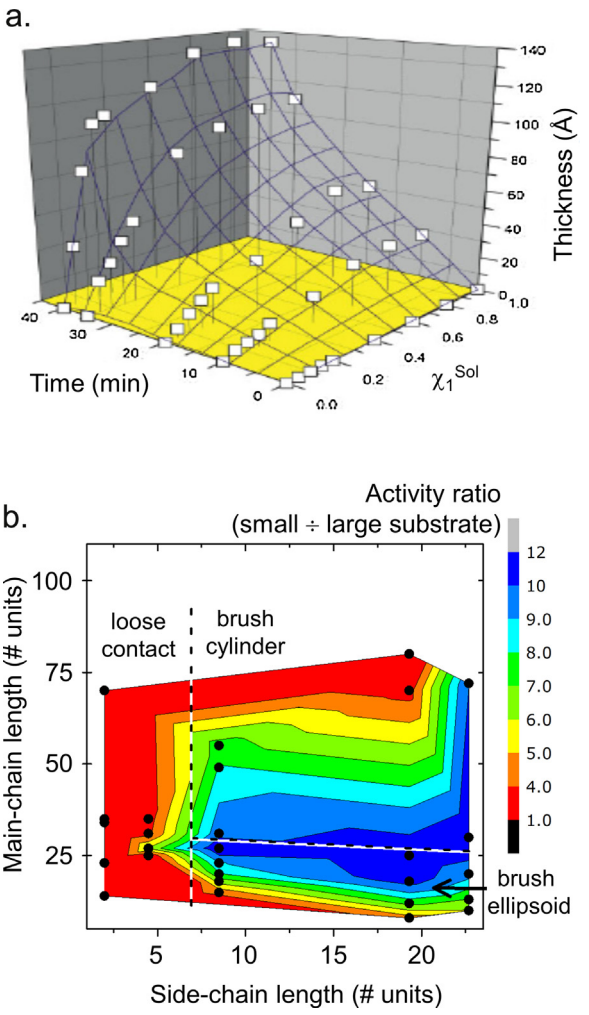

Fig. 6. pOEGMA main-chain conformation within non-fouling brushes. (a) Kinetics of pOEGMA brush growth (thickness) from mixed self-assembled monolayers (containing a certain fraction of polymerization initiators χ_1^{Sol}) on gold. Ellipsometry thickness plotted against χ^{Sol} and time shows that the rate of brush grown increases more rapidly at longer polymerization times. This was attributed to a change from a collapsed to an extended main-chain conformation [25]. (b) Regions of preferential activity towards the small substrate benzoyl-L-tyrosine *p*-nitroanilide compared to large substrates casein, were observed. This selective permeability was optimal when pOEGMA chains were collapsed on the surface of the protein and behaved as ellipsoids, and was attenuated when the main-chain adopted an extended conformation. The conjugates all possess 12 pOEGMA chains per protein. Color maps established as linear projections between datapoints. Sources [25,28], Copyright 2006, 2015, respectively. Adapted with permission from John Wiley & Sons Inc.

as a function of main-chain length have been observed in solution by small-angle neutron scattering for other comb polymers such as poly(styrene)-graft-oligo(ethylene glycol) [26]. Ma et al. [25] observed that the threshold for achieving efficient protein repellency using pOEGMA films appears to lie before the transition from collapsed to extended (based on our interpretation of film growth kinetics), though these specific experiments were unable to distinguish the relative protein-repellency of these two structures of pOEGMA.

Gao et al. [64] examined the conformation of P2-stat-P9 brushes on silicon surfaces in water by neutron reflectometry. Below the LCST of the polymer, the volume fraction of water inside the brush was greater than 50%. However, above the LCST, the brush collapsed and partially expelled water, yielding a distinct interface between the polymer layer and water. Nevertheless, the fraction of water remained high, at ~30 vol%. Of particular interest, and in line with the observations of others [65], effective non-fouling properties were observed in both the extended and collapsed states. These combined results suggest that a hydration layer is probably still present at the polymer–water interface even when the main-chain is collapsed, and still effectively preventing the adsorption of proteins. However, Tugulu and Klok [58] have observed that modification of the hydration layer can have an impact on brush stability. Partial detachment of P9 (note: hydroxyl not methyl ether) from silicon oxide occurred when immersed in cell culture medium, even though the brushes were stable in water. Possible explanations of the authors were osmotic stress on the brush that would add to the entropically disfavored stretched chain conformation and promote detachment. This could be circumvented by decreasing grafting density without compromising non-fouling characteristics.

When dried, solid-grafted pOEGMA films can crystallize in a side-chain and film-thickness-dependent manner. Zheng et al. [66] have observed that surface-grafted P5 and P9 remain amorphous, while P23 crystallized at room temperature. Analysis by atomic force microscopy and infrared spectroscopy were consistent with lamellae oriented perpendicular to the substrate for films with thicknesses >100 nm, implying that the helical axis of the side-chains is parallel to the surface. Crystallization of P23 could be prevented by co-polymerization with P9 [67]. Limiting crystallinity of the films by controlling the molecular characteristics of pOEGMA was exploited by the authors for achieving enhanced ion conduction and gas permeability.

4.2. Shielding of biomolecules

To the extent of our knowledge, Lele et al. [68] were the first to synthesize a well-defined conjugate of pOEGMA and a protein, α-chymotrypsin. Since then, pOEGMA has been used to extend the circulation lifetime of several proteins by increasing their hydrodynamic radius and preventing opsonisation/enzymatic digestion [69,70]. Indeed, the protein-repellant characteristics of pOEGMA have been exploited for disfavoring interaction with binding proteins such as antibodies as well as reactive proteins such as enzymes. Ryan et al. [71] demonstrated that P23 conjugated to the N-terminus of the small protein salmon calcitonin increased its resistance to digestion by intestinal enzymes. Interestingly, pOEGMA conjugation did not impart a large loss of bioactivity, despite the fact that the latter involves binding to a large receptor [72]. Magnusson et al. [73] conjugated 6–8 chains of P9 to human growth hormone and observed enhanced stability under stress conditions such as magnetic stirring (to induce aggregation) and enzymatic digestion by pepsin. In addition to providing a steric barrier to protein adsorption, the hydrophobicity of the pOEGMA main-chain has been found in some cases to enhance activity, possibly by creating a hydrophobic microenvironment that promotes the sequestration of hydrophobic substrates. This was notably observed for a bio-conjugate of P2-stat-P9 and trypsin [74]. pOEGMA has also been used for similar purposes to protect DNA (or RNA) within self-assembled supramolecular structures such as complex coacervate core micelles or by covalent conjugation [75–77]. For example, Averick et al. [77] modified siRNA with two copies of either P9, P2-stat-P5, or P9-stat-*N*,*N*-dimethylaminoethyl methacrylate (DMAEMA), one at each extremity. Interestingly, the authors demonstrated that the polymer–siRNA architecture simultaneously imparted protection from nucleases as well as cell permeability. Understanding the underlying mechanism of these results may provide the means for establishing optimal characteristics of the polymer that are necessary to achieve the desired effect. In another example Uzgun et al. [78] complexed plasmid DNA with a series of block co-polymers of pDMAEMA and pOEGMA (P9, P23, and P45) of variable composition but of equal total number of monomeric repeat units (~120). Experimentally, the authors were able to distinguish that pOEGMA largely reduced binding to the surface of cells, while internalization was less affected. The surface charge gradually decreased with increasing pOEGMA main-chain length, which the authors attributed to its shielding effect. Compared to the polycation homo-polymer, the efficacy of DNA complexation was also negatively affected by pOEGMA main-chain length. However, as the polycation segment is responsible for DNA complexation via ionic interactions, this result could also be related to the polycation segment becoming shorter within the library of polymers tested. Further, complexation was efficient for short side-chains, but failed in the case of P45, though the mechanism behind this remains to be elucidated.

In addition to effectively repelling proteins, there has been some evidence in the literature that pOEGMA coatings can be selectively permeable to smaller molecules. For instance, Trmcic-Cvitas et al. [79] observed that molecular infiltration into P5 and P12 brushes (note: hydroxyl not methyl ether) on gold surfaces was dictated by size. That is, smaller proteins such as streptavidin (52.8 kDa) could diffuse throughout the brush whereas bulky antibodies (~150 kDa) could only penetrate the upper layer. Recently, our group [28] has investigated this concept and systematically examined the relationship between molecular characteristics of pOEGMA brushes grafted to the protein α-chymotrypsin, their conformation, and their permeability to molecules of different sizes. Employing solution ^{1}H NMR spectroscopy to determine whether the main-chain was collapsed or extended, the authors observed that the transition from collapsed-to-extended occurred at shorter main-chain length when the polymer grafting density was high, or with increasing side-chain length. These results suggest that crowding of pOEGMA on the surface of the protein could be an influential parameter on the transition. Efficient protein-repellency was observed both above and below this transition, though, interestingly, in the collapsed state, just below the transition to extended, substantial permeability of the coating to small versus large molecules was

observed, as evidenced by high catalytic activity towards a small substrate and a very low activity towards a large substrate (Fig. 6b). This result suggests that pOEGMA occupies a small footprint when the main-chain is collapsed, leading to the formation of small gaps that remain large enough for small molecules to pass. Irrespective of the conformation of the main-chain (collapsed or extended) the conjugates also displayed LCSTs at higher temperatures, which indicated that this observation is not related to temperature-induced collapse of the side-chains, as this occurred at higher temperature. Exploiting pOEGMA main-chain conformation for controlling the properties of bioconjugates was recently used to reduce the in vivo immunogenicity of the enzyme L-asparaginase [27]. Indeed, using solution ^{1}H NMR spectroscopy to guide the choice of molecular dimensions of pOEGMA so that it remained in the desired ellipsoidal conformation led to a bio-conjugate with immunogenicity that was several orders of magnitude lower than the native protein, with a relatively small effect on its catalytic activity towards its small substrate L-asparagine.

5. Summary and outlook

pOEGMA is an extremely versatile polymer because control of its molecular dimensions has a predictable effect on the conformation of its main-chain and side-chains, which can be, independently, either extended or collapsed. This contribution has highlighted how the control over the conformations of pOEGMA is the common driving force behind its thermosensitivity properties in solution, its supramolecular assembly features, and can influence its protein-repellency and permeability characteristics. Unfortunately, comparatively little information is available on the long-term toxicity and metabolism of pOEGMA in vivo. This important information is crucial considering that many of the applications of pOEGMA are within the biomedical area. Future work should thus concentrate on evaluating the biological properties of pOEGMA, with emphasis on the influence of co-monomer composition and chemical modification, which are commonly exploited parameters to alter its properties. Finally, considering the non-specific nature of the physical driving force behind of the conformation changes observed for pOEGMA, which mostly involve steric hindrance and amphiphilicity of the side-chains, findings presented in this Trend article may nucleate the development of new platforms of responsive and functional comb-type polymers based on other types of monomers.

Acknowledgments

M.L. recognizes a doctoral scholarship from the Chinese Scholarship Council (CSC). The Sassella foundation is gratefully acknowledged for funding of our research program on comb-shaped polymers.

References

[1] Vamvakaki M, Billingham NC, Armes SP. Synthesis of water-soluble statistical copolymers and terpolymers containing pendent oligo(ethylene glycol derivatives). Polymer 1999;40:5161–71.
[2] Bütün V, Vamvakaki M, Billingham NC, Armes SP. Synthesis and aqueous solution properties of novel neutral/acidic block copolymers. Polymer 2000;41:3173–82.
[3] Wang XS, Armes SP. Facile atom transfer radical polymerization of methoxy-capped oligo(ethylene glycol) methacrylate in aqueous media at ambient temperature. Macromolecules 2000;33:6640–7.
[4] Luo N, Hutchison JB, Anseth KS, Bowman CN. Surface-initiated photopolymerization of poly(ethylene glycol) methyl ether methacrylate on a diethyldithiocarbamate-mediated polymer substrate. Macromolecules 2002;35:2487–93.
[5] Wang XS, Lascelles SF, Jackson RA, Armes SP. Facile synthesis of well-defined water-soluble polymers via atom transfer radical polymerization in aqueous media at ambient temperature. Chem Commun 1999;18:1817–8.
[6] Han S, Hagiwara M, Ishizone T. Synthesis of thermally sensitive water-soluble polymethacrylates by living anionic polymerizations of oligo(ethylene glycol) methyl ether methacrylates. Macromolecules 2003;36:8312–9.
[7] Ma HW, Hyun JH, Stiller P, Chilkoti A. "Non-fouling" oligo(ethylene glycol)-functionalized polymer brushes synthesized by surface-initiated atom transfer radical polymerization. Adv Mater 2004;16:338–41.
[8] Bebis K, Jones MW, Haddleton DM, Gibson MI. Thermoresponsive behaviour of poly[(oligo(ethyleneglycol methacrylate)]s and their protein conjugates: importance of concentration and solvent system. Polym Chem 2011;2:975–82.
[9] Gibson MI, O'Reilly RK. To aggregate, or not to aggregate? Considerations in the design and application of polymeric thermally-responsive nanoparticles. Chem Soc Rev 2013;42:7204–13.
[10] Hu Z, Cai T, Chi C. Thermoresponsive oligo(ethylene glycol)-methacrylate-based polymers and microgels. Soft Matter 2010;6:2115–23.
[11] Hucknall A, Rangarajan S, Chilkoti A. In pursuit of zero: polymer brushes that resist the adsorption of proteins. Adv Mater 2009;21:2441–6.
[12] Lutz JF. Polymerization of oligo(ethylene glycol) (meth)acrylates: toward new generations of smart biocompatible materials. J Polym Sci A: Polym Chem 2008;46:3459–70.
[13] Neugebauer D. Graft copolymers with poly(ethylene oxide) segments. Polym Int 2007;56:1469–98.
[14] Roy D, Brooks WLA, Sumerlin BS. New directions in thermoresponsive polymers. Chem Soc Rev 2013;42:7214–43.
[15] Vancoillie G, Frank D, Hoogenboom R. Thermoresponsive poly(oligo ethylene glycol acrylates). Prog Polym Sci 2014;39:1074–95.
[16] Weber C, Hoogenboom R, Schubert US. Temperature responsive bio-compatible polymers based on poly(ethylene oxide) and poly(2-oxazoline)s. Prog Polym Sci 2012;37:686–714.
[17] Keddie DJ. A guide to the synthesis of block copolymers using reversible-addition fragmentation chain transfer (RAFT) polymerization. Chem Soc Rev 2014;43:496–505.
[18] Matyjaszewski K. Atom transfer radical polymerization: from mechanisms to applications. Isr J Chem 2012;52:206–20.
[19] Moad G, Rizzardo E, Thang SH. RAFT polymerization and some of its applications. Chem Asian J 2013;8:1634–44.
[20] O'Donnell JM. Reversible addition–fragmentation chain transfer polymerization in microemulsion. Chem Soc Rev 2012;41:3061–76.
[21] Siegwart DJ, Oh JK, Matyjaszewski K. ATRP in the design of functional materials for biomedical applications. Prog Polym Sci 2012;37:18–37.
[22] Oh JK, Min K, Matyjaszewski K. Preparation of poly(oligo(ethylene glycol) monomethyl ether methacrylate) by homogeneous aqueous AGET ATRP. Macromolecules 2006;39:3161–7.
[23] Averick S, Simakova A, Park S, Konkolewicz D, Magenau AJD, Mehl RA, Matyjaszewski K. ATRP under biologically relevant conditions: grafting from a protein. ACS Macro Lett 2011;1:6–10.
[24] Soeriyadi AH, Li GZ, Slavin S, Jones MW, Amos CM, Becer CR, Whittaker MR, Haddleton DM, Boyer C, Davis TP. Synthesis and modification of thermoresponsive poly(oligo(ethylene glycol) methacrylate) via catalytic chain transfer polymerization and thiol-ene Michael addition. Polym Chem 2011;2:815–22.
[25] Ma HW, Wells M, Beebe TP, Chilkoti A. Surface-initiated atom transfer radical polymerization of oligo(ethylene glycol) methyl methacrylate from a mixed self-assembled monolayer on gold. Adv Funct Mater 2006;16:640–8.
[26] Cheng G, Melnichenko YB, Wignall GD, Hua F, Hong K, Mays JW. Small angle neutron scattering study of conformation of oligo(ethylene glycol)-grafted polystyrene in dilute solutions: effect of the backbone length. Macromolecules 2008;41:9831–6.

[27] Liu M, Johansen P, Zabel F, Leroux JC, Gauthier MA. Semi-permeable coatings fabricated from comb-polymers efficiently protect proteins in vivo. Nat Commun 2014;5 (5526/1-8).
[28] Liu M, Tirino P, Radivojevic M, Phillips DJ, Gibson MI, Leroux JC, Gauthier MA. Molecular sieving on the surface of a protein provides protection without loss of activity. Adv Funct Mater 2013;23:2007–15.
[29] Ishizone T, Seki A, Hagiwara M, Han S, Yokoyama H, Oyane A, Deffieux A, Carlotti S. Anionic polymerizations of oligo(ethylene glycol) alkyl ether methacrylates: effect of side chain length and omega-alkyl group of side chain on cloud point in water. Macromolecules 2008;41:2963–7.
[30] Mertoglu M, Garnier S, Laschewsky A, Skrabania K, Storsberg J. Stimuli responsive amphiphilic block copolymers for aqueous media synthesised via reversible addition fragmentation chain transfer polymerisation (RAFT). Polymer 2005;46:7726–40.
[31] Becer CR, Hahn S, Fijten MWM, Thijs HML, Hoogenboom R, Schubert US. Libraries of methacrylic acid and oligo(ethylene glycol) methacrylate copolymers with LCST behavior. J Polym Sci A: Polym Chem 2008;46:7138–47.
[32] Roth PJ, Jochum FD, Forst FR, Zentel R, Theato P. Influence of end groups on the stimulus-responsive behavior of poly[oligo(ethylene glycol) methacrylate] in water. Macromolecules 2010;43:4638–45.
[33] Lutz JF, Hoth A. Preparation of ideal PEG analogues with a tunable thermosensitivity by controlled radical copolymerization of 2-(2-methoxyethoxy)ethyl methacrylate and oligo(ethylene glycol) methacrylate. Macromolecules 2006;39:893–6.
[34] Yamamoto SI, Pietrasik J, Matyjaszewski K. The effect of structure on the thermoresponsive nature of well-defined poly(oligo(ethylene oxide) methacrylates) synthesized by ATRP. J Polym Sci A: Polym Chem 2008;46:194–202.
[35] Lutz JF, Akdemir O, Hoth A. Point by point comparison of two thermosensitive polymers exhibiting a similar LCST: is the age of poly(NIPAM) over? J Am Chem Soc 2006;128:13046–7.
[36] Magnusson JP, Khan A, Pasparakis G, Saeed AO, Wang W, Alexander C. Ion-sensitive "Isothermal" responsive polymers prepared in water. J Am Chem Soc 2008;130:10852–3.
[37] Dong H, Mantha V, Matyjaszewski K. Thermally responsive PM(EO)2MA magnetic microgels via activators generated by electron transfer atom transfer radical polymerization in miniemulsion. Chem Mater 2009;21:3965–72.
[38] Dong H, Matyjaszewski K. Thermally responsive P(M(EO)2MA-*co*-OEOMA) copolymers via AGET ATRP in miniemulsion. Macromolecules 2010;43:4623–8.
[39] Kowalczuk A, Mendrek B, Zymelka-Miara I, Libera M, Marcinkowski A, Trzebicka B, Smet M, Dworak A. Solution behavior of star polymers with oligo(ethylene glycol) methyl ether methacrylate arms. Polymer 2012;53:5619–31.
[40] He L, Huang J, Chen Y, Xu X, Liu L. Inclusion interaction of highly densely PEO grafted polymer brush and α-cyclodextrin. Macromolecules 2005;38:3845–51.
[41] Kleine A, Altan CL, Yarar UE, Sommerdijk NAJM, Bucak S, Holder SJ. The polymerisation of oligo(ethylene glycol methyl ether) methacrylate from a multifunctional poly(ethylene imine) derived amide: a stabiliser for the synthesis and dispersion of magnetite nanoparticles. Polym Chem 2014;5:524–34.
[42] Liu Y, Chen P, Li Z. Molecular bottlebrushes with polypeptide backbone prepared via ring-opening polymerization of NCA and ATRP. Macromol Rapid Commun 2012;33:287–95.
[43] Zhou D, Xiang L, Zeng R, Cao F, Zhu X, Wang Y. Graft copolymer composed of cationic backbone and bottle brush-like side chains as a physically adsorbed coating for protein separation by capillary electrophoresis. J Sep Sci 2011;34:3441–50.
[44] Yamamoto Si, Pietrasik J, Matyjaszewski K. ATRP synthesis of thermally responsive molecular brushes from oligo(ethylene oxide) methacrylates. Macromolecules 2007;40:9348–53.
[45] Roth PJ, Jochum FD, Theato P. UCST-type behavior of poly[oligo(ethylene glycol) methyl ether methacrylate] (POEGMA) in aliphatic alcohols: solvent, co-solvent, molecular weight, and end group dependences. Soft Matter 2011;7:2484–92.
[46] Roth PJ, Davis TP, Lowe AB. Comparison between the LCST and UCST transitions of double thermoresponsive diblock copolymers: insights into the behavior of POEGMA in alcohols. Macromolecules 2012;45:3221–30.
[47] Lutz JF, Weichenhan K, Akdemir Ö, Hoth A. About the phase transitions in aqueous solutions of thermoresponsive copolymers and hydrogels based on 2-(2-methoxyethoxy)ethyl methacrylate and oligo(ethylene glycol) methacrylate. Macromolecules 2007;40:2503–8.
[48] Trzebicka B, Szweda D, Rangelov S, Kowalczuk A, Mendrek B, Utrata-Wesolek A, Dworak A. (Co) polymers of oligo(ethylene glycol) methacrylates-temperature-induced aggregation in aqueous solution. J Polym Sci A: Polym Chem 2013;51:614–23.
[49] Hussain H, Mya KY, He C. Self-assembly of brush-like poly[poly(ethylene glycol) methyl ether methacrylate] synthesized via aqueous atom transfer radical polymerization. Langmuir 2008;24:13279–86.
[50] Trzcinska R, Szweda D, Rangelov S, Suder P, Silberring J, Dworak A, Trzebicka B. Bioactive mesoglobules of poly(di(ethylene glycol) monomethyl ether methacrylate)–peptide conjugate. J Polym Sci A: Polym Chem 2012;50:3104–15.
[51] Roth PJ, Davis TP, Lowe AB. UCST-driven self-assembly and crosslinking of diblock copolymer micelles. Polym Chem 2012;3:2228–35.
[52] De Graaf AJ, Mastrobattista E, Vermonden T, van Nostrum CF, Rijkers DTS, Liskamp RMJ, Hennink WE. Thermosensitive peptide-hybrid ABC block copolymers obtained by ATRP: synthesis, self-assembly, and enzymatic degradation. Macromolecules 2012;45:842–51.
[53] Gibson MI, Paripovic D, Klok HA. Size-dependent LCST transitions of polymer-coated gold nanoparticles: cooperative aggregation and surface assembly. Adv Mater 2010;22:4721–5.
[54] Neugebauer D, Zhang Y, Pakula T, Sheiko SS, Matyjaszewski K. Densely-grafted and double-grafted PEO brushes via ATRP. A route to soft elastomers. Macromolecules 2003;36:6746–55.
[55] Xu FJ, Zhong SP, Yung LYL, Kang ET, Neoh KG. Surface-active and stimuli-responsive polymer-Si(1 0 0) hybrids from surface-initiated atom transfer radical polymerization for control of cell adhesion. Biomacromolecules 2004;5:2392–403.
[56] Ma HW, Li DJ, Sheng X, Zhao B, Chilkoti A. Protein-resistant polymer coatings on silicon oxide by surface-initiated atom transfer radical polymerization. Langmuir 2006;22:3751–6.
[57] Singh N, Cui XF, Boland T, Husson SM. The role of independently variable grafting density and layer thickness of polymer nanolayers on peptide adsorption and cell adhesion. Biomaterials 2007;28:763–71.
[58] Tugulu S, Klok HA. Stability and nonfouling properties of poly(poly(ethylene glycol) methacrylate) brushes under cell culture conditions. Biomacromolecules 2008;9:906–12.
[59] Lee BS, Chi YS, Lee KB, Kim YG, Choi IS. Functionalization of poly(oligo(ethylene glycol) methacrylate) films on gold and Si/SiO_2 for immobilization of proteins and cells: SPR and QCM studies. Biomacromolecules 2007;8:3922–9.
[60] Müllner M, Cui J, Noi KF, Gunawan ST, Caruso F. Surface-initiated polymerization within mesoporous silica spheres for the modular design of charge-neutral polymer particles. Langmuir 2014;30:6286–93.
[61] Deng X, Smeets NMB, Sicard C, Wang J, Brennan JD, Filipe CDM, Hoare T. Poly(oligoethylene glycol methacrylate) dip-coating: turning cellulose paper into a protein-repellent platform for biosensors. J Am Chem Soc 2014;136:12852–5.
[62] Jia Z, Yuan W, Zhao H, Hu H, Baker GL. Composite electrolytes comprised of poly(ethylene oxide) and silica nanoparticles with grafted poly(ethylene oxide)-containing polymers. RSC Adv 2014;4:41087–98.
[63] Zheng Y, Bruening ML, Baker GL. Crystallization kinetics of polymer brushes with poly(ethylene oxide) side chains. J Polym Sci B: Polym Phys 2010;48:1955–9.
[64] Gao X, Kucerka N, Nieh MP, Katsaras J, Zhu SP, Brash JL, Sheardown H. Chain conformation of a new class of PEG-based thermoresponsive polymer brushes grafted on silicon as determined by neutron reflectometry. Langmuir 2009;25:10271–8.
[65] Boyer C, Whittaker MR, Luzon M, Davis TP. Design and synthesis of dual thermoresponsive and antifouling hybrid polymer/gold nanoparticles. Macromolecules 2009;42:6917–26.
[66] Zheng Y, Bruening ML, Baker GL. Crystallization of polymer brushes with poly(ethylene oxide) side chains. Macromolecules 2007;40:8212–9.
[67] Grajales ST, Dong X, Zheng Y, Baker GL, Bruening ML. Effects of monomer composition on CO_2–selective polymer brush membranes. Chem Mater 2010;22:4026–33.
[68] Lele BS, Murata H, Matyjaszewski K, Russell AJ. Synthesis of uniform protein-polymer conjugates. Biomacromolecules 2005;6:3380–7.
[69] Gao WP, Liu WG, Mackay JA, Zalutsky MR, Toone EJ, Chilkoti A. In situ growth of a stoichiometric PEG-like conjugate at a protein's N-terminus with significantly improved pharmacokinetics. Proc Natl Acad Sci USA 2009;106:15231–6.
[70] Gao WP, Liu WG, Christensen T, Zalutsky MR, Chilkoti A. In situ growth of a PEG-like polymer from the C terminus of an intein fusion protein improves pharmacokinetics and tumor accumulation. Proc Natl Acad Sci USA 2010;107:16432–7.

[71] Ryan SM, Frias JM, Wang XX, Sayers CT, Haddleton DM, Brayden DJ. PK/PD modelling of comb-shaped PEGylated salmon calcitonin conjugates of differing molecular weights. J Controlled Release 2011;149:126–32.
[72] Ryan SM, Wang XX, Mantovani G, Sayers CT, Haddleton DM, Brayden DJ. Conjugation of salmon calcitonin to a combed-shaped end functionalized poly(poly(ethylene glycol) methyl ether methacrylate) yields a bioactive stable conjugate. J Controlled Release 2009;135:51–9.
[73] Magnusson JP, Bersani S, Salmaso S, Alexander C, Caliceti P. In situ growth of side-chain PEG polymers from functionalized human growth hormone—a new technique for preparation of enhanced protein-polymer conjugates. Bioconjugate Chem 2010;21:671–8.
[74] Zarafshani Z, Obata T, Lutz JF. Smart PEGylation of trypsin. Biomacromolecules 2010;11:2130–5.
[75] Pirotton S, Muller C, Pantoustier N, Botteman F, Collinet B, Grandfils C, Dandrifosse G, Degee P, Dubois P, Raes M. Enhancement of transfection efficiency through rapid and noncovalent post-PEGylation of poly(dimethylaminoethyl methacrylate)/DNA complexes. Pharm Res 2004;21:1471–9.
[76] Kong WH, Sung DK, Shim YH, Bae KH, Dubois P, Park TG, Kim JH, Seo SW. Efficient intracellular siRNA delivery strategy through rapid and simple two steps mixing involving noncovalent post-PEGylation. J Controlled Release 2009;138:141–7.
[77] Averick SE, Paredes E, Dey SK, Snyder KM, Tapinos N, Matyjaszewski K, Das SR. Autotransfecting short interfering RNA through facile covalent polymer escorts. J Am Chem Soc 2013;135:12508–11.
[78] Uzgun S, Akdemir O, Hasenpusch G, Maucksch C, Golas MM, Sander B, Stark H, Imker R, Lutz JF, Rudolph C. Characterization of tailor-made copolymers of oligo(ethylene glycol) methyl ether methacrylate and *N*,*N*-dimethylaminoethyl methacrylate as nonviral gene transfer agents: influence of macromolecular structure on gene vector particle properties and transfection efficiency. Biomacromolecules 2010;11:39–50.
[79] Trmcic-Cvitas J, Hasan E, Ramstedt M, Li X, Cooper MA, Abell C, Huck WTS, Gautrot JE. Biofunctionalized protein resistant oligo(ethylene glycol)-derived polymer brushes as selective immobilization and sensing platforms. Biomacromolecules 2009;10:2885–94.

nature COMMUNICATIONS

ARTICLE

Received 19 May 2014 | Accepted 10 Oct 2014 | Published 19 Nov 2014

DOI: 10.1038/ncomms6526

Semi-permeable coatings fabricated from comb-polymers efficiently protect proteins *in vivo*

Mi Liu[1], Pål Johansen[2], Franziska Zabel[2], Jean-Christophe Leroux[1] & Marc A. Gauthier[1,3]

In comparison to neutral linear polymers, functional and architecturally complex (that is, non-linear) polymers offer distinct opportunities for enhancing the properties and performance of therapeutic proteins. However, understanding how to harness these parameters is challenging, and studies that capitalize on them *in vivo* are scarce. Here we present an *in vivo* demonstration that modification of a protein with a polymer of appropriate architecture can impart low immunogenicity, with a commensurably low loss of therapeutic activity. These combined properties are inaccessible by conventional strategies using linear polymers. For the model protein L-asparaginase, a comb-polymer bio-conjugate significantly outperformed the linear polymer control in terms of lower immune response and more sustained bioactivity. The semi-permeability characteristics of the coatings are consistent with the phase diagram of the polymer, which will facilitate the application of this strategy to other proteins and with other therapeutic models.

[1] Institute of Pharmaceutical Sciences, Department of Chemistry and Applied Biosciences, Swiss Federal Institute of Technology Zurich (ETH Zurich), Zurich 8093, Switzerland. [2] Department of Dermatology, University Hospital Zurich, Zurich 8091, Switzerland. [3] Institut National de la Recherche Scientifique (INRS), EMT Research Center, Varennes, Quebec J3X 1S2, Canada. Correspondence and requests for materials should be addressed to M.A.G. (email: gauthier@emt.inrs.ca).

Many advances in biotechnology can be linked to the development of robust methods for producing well-defined functional polymers. For instance, anionic polymerization has yielded one of the first well-defined linear polymers, α-methoxy-poly(ethylene glycol) (mPEG), variants of which have profoundly marked the pharmaceutical sector as protective coatings for protein drugs[1–3]. Controlled radical polymerization has also permitted the design of numerous macromolecular drugs, polymer–drug and polymer–protein conjugates[4]. The state-of-the-art of tailored polymer synthesis is currently evolving, the controlled polymerization of functional monomers has become commonplace[5] and new tools for preparing polymers with defined sequences and topologies continue to emerge[6,7]. In comparison to neutral linear polymers, functional and architecturally complex, that is, nonlinear, polymers offer numerous additional opportunities for enhancing the potential of therapeutic proteins, but have only recently drawn attention in therapeutics. Maynard and co-workers have shown that basic fibroblast growth factor could be stabilized by covalent conjugation with a heparin-mimicking polymer containing styrene sulfonate and oligo(ethylene glycol) monomethyl ether methacrylate (OEGMA) units[8]. The conjugate was stable to a variety of environmentally and therapeutically relevant stressors such as heat, acid, storage and proteases. Keefe and Jiang showed how a poly(zwitterionic) polymer grafted to α-chymotrypsin strongly stabilized the latter, even towards strong denaturants, via non-covalent interactions between the polymer and the protein[9]. Unfortunately, *in vivo* studies are scarce. Leroux and co-workers recently demonstrated that the functionality of different polymers grafted to proline-specific endopeptidases could be manipulated to stabilize and alter the dwell time of orally administered enzymes at different locations in the gastrointestinal tract[10]. Such studies are crucial because trends and observations made *in vitro* often do not correlate with *in vivo* observations[11]. This is in part due to the complex and potentially unpredictable nature of the interactions between the conjugate and components of the body.

Our group has recently discovered that comb-shaped poly-OEGMA (pOEGMA) chains with well-defined aspect ratios could generate a molecular sieving effect *in vitro* when grafted to the surface of a protein[12]. Within a certain regime of polymer characteristics, small molecules could easily diffuse through the coating towards the catalytic site of an enzyme (that is, maintaining high activity), whereas macromolecules were simultaneously blocked. This selective permeability phenomenon, which cannot be emulated with linear mPEG, could be of exceptional value for reducing the immunogenicity of recombinant, non-human-derived therapeutic enzymes without hindering catalytic processing of small molecules. One protein that falls into this category is L-asparaginase (ASNase), an enzyme that is used for treating acute lymphoblastic leukaemia. This protein was one of the first to be modified with mPEG because of its propensity to cause severe hypersensitivity reactions (up to 20–30% of patients)[13] or suffer from 'silent inactivation' by the neutralizing or opsonizing antibodies[14,15]. Modification of ASNase with mPEG in part overcomes these problems[16], however, a key problem is that antibody responses against mPEG–ASNase continue to occur in ~18% of patients[17–19].

In this study, a molecular sieving pOEGMA coating is optimized for ASNase. In a head-to-head comparison with mPEG–ASNase, pOEGMA–ASNase is ~100-fold less recognized by anti-ASNase antibodies than mPEG–ASNase and 3,000-fold less than the native protein, with a commensurably low loss of activity. In addition, pOEGMA extends the circulation time of ASNase even in mice previously sensitized to ASNase. The semi-permeability characteristics of the coatings are consistent with the phase diagram of protein-bound pOEGMA, which demonstrates that one can design optimal pOEGMA coatings for proteins with little trial-and-error. Polymer architecture, via the comb-shaped nature of pOEGMA, is a potent parameter for optimizing the bioactivity of therapeutic proteins.

Results

Molecular sieving pOEGMA–ASNase bio-conjugates. ASNase, Fig. 1a, is a tetrameric protein that possesses four identical catalytic sites that transform L-asparagine (Asn) into L-aspartic acid (Asp). As seen in Fig. 1, the solvent-exposed amino groups (lysine and *N*-termini in red) are uniformly distributed on the surface of the protein and were converted into initiators for atom transfer radical polymerization. Three ASNase macro-initiators bearing on average $x = 24$, 32 and 36 initiators per protein tetramer were obtained. The degree of modification was assessed by matrix-assisted laser desorption/ionization–time of flight mass spectrometry, which showed symmetric distributions near ~35 kDa (ASNase disassembles into its monomeric form in this experiment; Fig. 1b). The centre of these distributions was taken as the average degree of modification and correlated well with the feed ratios of reactants (Supplementary Fig. 1). Assuming ASNase to be a sphere with a 3.4-nm radius[20], these values of x were targeted based on the expectation that a polymer density of at least one pOEGMA chain per ~4 nm^2 of protein surface is required to observe the sieving effect[12]. The polymerization of an OEGMA monomer with eight to ten oxyethylene units was initiated from these sites. Growing polymers directly from proteins is a powerful approach for generating complex bio-conjugates[21–25] and offers the advantage of producing a series of comparable bio-conjugates differing uniquely in the length of the polymer backbone (n). The length of the polymer backbone was varied by allowing the polymerizations to proceed for different times between 30 min and 4 h. The 19 unique bio-conjugates obtained showed monomodal size-exclusion chromatograms (Fig. 1c). The molecular weight characteristics of the pOEGMA chains were determined by three complementary methods and can be found in Supplementary Table 1. One ASNase conjugate bearing ca 42 chains of mPEG (5 kDa), determined by ^{1}H NMR spectroscopy (Supplementary Fig. 2), was produced for comparison. This grafting ratio is in the range expected of commercially available mPEG–ASNase conjugates (Sigma-Aldrich).

To characterize the molecular sieving characteristics of the conjugates, the conformation of pOEGMA was analysed by ^{1}H NMR spectroscopy (Fig. 2a,b) and correlated to the catalytic activity of the conjugates (aspartyl transferase assay; Fig. 2c) and their anti-ASNase-binding affinity (sandwich ELISA; Fig. 2d). As a comb-shaped polymer, pOEGMA can adopt either an ellipsoidal or a cylindrical shape as a function of increasing backbone length n (ref. 26). These two states result from the backbone being either in an collapsed or in an extended conformation, a parameter that can be probed by ^{1}H NMR spectroscopy via peaks 'A' and 'B' (Figs 1a and 2a). As 'A' is in close proximity to the polymer backbone (Fig. 1a), its integrated value, which becomes less than expected in a rigid un-solvated environment, can be used to estimate its mobility. For this, a reference mobile and solvent-exposed group whose integral is expected to be least affected by de-solvation of the main-chain, such as 'B', is required (Fig. 2a). Indeed, Roth *et al.* have shown that 'B' retained >92% of its integrated value during pOEGMA's soluble-to-insoluble transition in alcohol, whereas peak 'A' was strongly affected[27]. Herein, peak 'B' remained sharp over a wide range of n (12–48; Supplementary Fig. 3). Figure 2b plots the dimensionless flexibility factor F, calculated from A and B

($F = 3A \div 2B$), which varies between 1 when the backbone is fully solvated and flexible to 0 when it is un-solvated and rigid. The abrupt decrease of F followed by an increase as a function of n is characteristic of protein-bound pOEGMA undergoing an ellipsoid-to-cylinder transition. The increase at high n is observed because F reflects the average flexibility of the entire polymer chain, which increases as it extends away from the protein. The transition, identified by arrows in Fig. 2b, is then projected as a dashed line in Fig. 2c,d, which plot catalytic activity and anti-ASNase-binding affinity, respectively, as a function of x and n. Optimal molecular sieving characteristics were previously observed at n just below the transition between these two conformations[12]. Compared with the first values measured at low n, no statistically significant difference in the catalytic activity of the bio-conjugates was observed in the ellipsoidal regime. A decrease was then observed beyond the transition (Fig. 2c; full analysis of variance (ANOVA) table in Supplementary Table 2; fitted parameters in Supplementary Table 3). Shielding of epitopes, assayed via the ability of anti-ASNase antibodies to bind the conjugates, followed a single exponential decay with n (Fig. 2d; fitted parameters in Supplementary Fig. 4). Increasing the complexity of the fit to a double exponential did not improve the quality of the fit. The rate of decay was more pronounced at higher x, although no obvious manifestation of the change of conformation of pOEGMA was evident in these curves. In comparison to native ASNase, mPEG–ASNase was 1.5 times less catalytically active and 25-fold less recognized by anti-ASNase antibodies. A pOEGMA–ASNase conjugate with optimal semi-permeability characteristics ($x = 32$, $n = 17$) was only three times less active than the native protein, but was 3,000-fold less recognized by anti-ASNase. Thus, in relation to the small decrease of activity observed between the mPEG and pOEGMA bio-conjugates, the gain in epitope shielding *in vitro*, and potential for lower immunogenicity *in vivo* (*vide infra*), is enormous. This pOEGMA–ASNase conjugate ($x = 32$, $n = 17$) was selected for *in vivo* analysis because it offered the best compromise between loss of catalytic activity and efficient epitope shielding (Fig. 2c,d).

Circulation time and bioactivity of ASNase *in vivo*. Having demonstrated that grafting of pOEGMA did not eliminate catalytic activity, pharmacokinetic experiments were performed. Here 800 IU kg^{-1} of ASNase, mPEG–ASNase or pOEGMA–ASNase ($x = 32$, $n = 17$) were administered in saline by intra-peritoneal injection to groups of three BALB/c mice. Blood was withdrawn

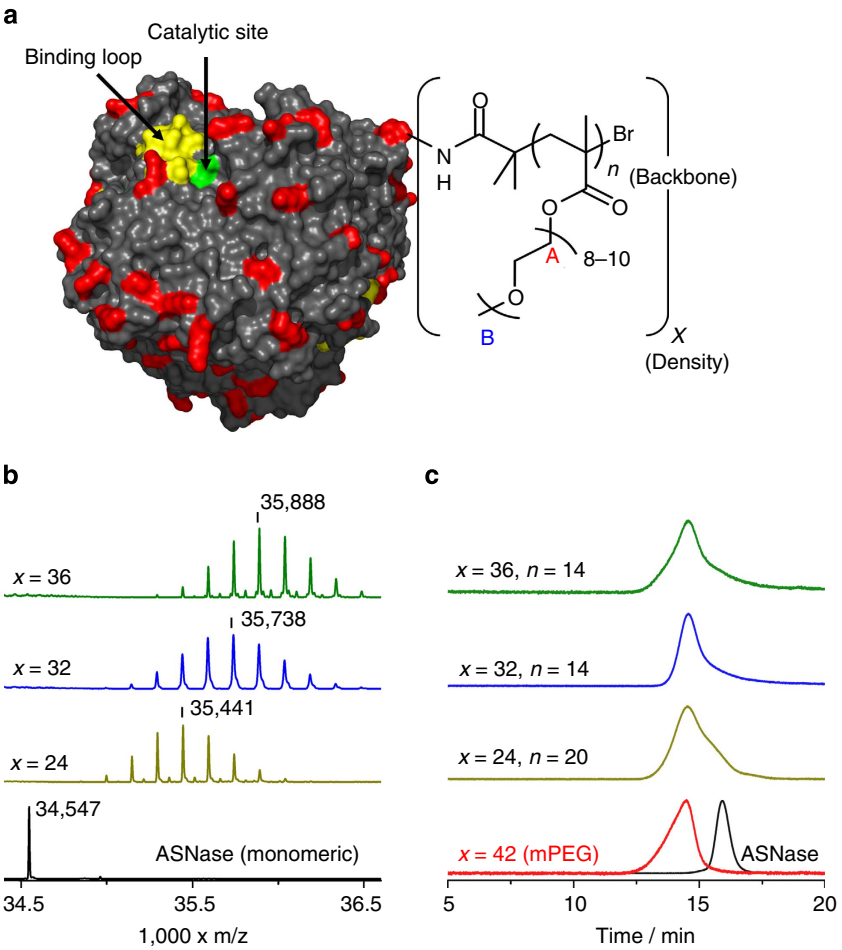

Figure 1 | Preparation of well-defined pOEGMA–ASNase conjugates. (**a**) Tetrameric ASNase possesses 92 amino groups (lysine residues and N-termini in red) that are evenly distributed on the solvent-exposed surface of the protein. Nineteen unique pOEGMA–ASNase conjugates were prepared by activation of a certain number (x) of these amino groups with 2-bromoisobutyryl bromide, followed *in situ* growth of different length (n) pOEGMA chains by atom transfer radical polymerization. (**b**) Analysis of the molecular weight of ASNase macro-initiators by matrix-assisted laser desorption/ionization-time of flight mass spectrometry to determine the average number of initiating groups per protein. (**c**) Representative size-exclusion chromatograms of pOEGMA–ASNase conjugates, mPEG–ASNase and native ASNase. All conjugates tested displayed monomodal molecular-weight distributions.

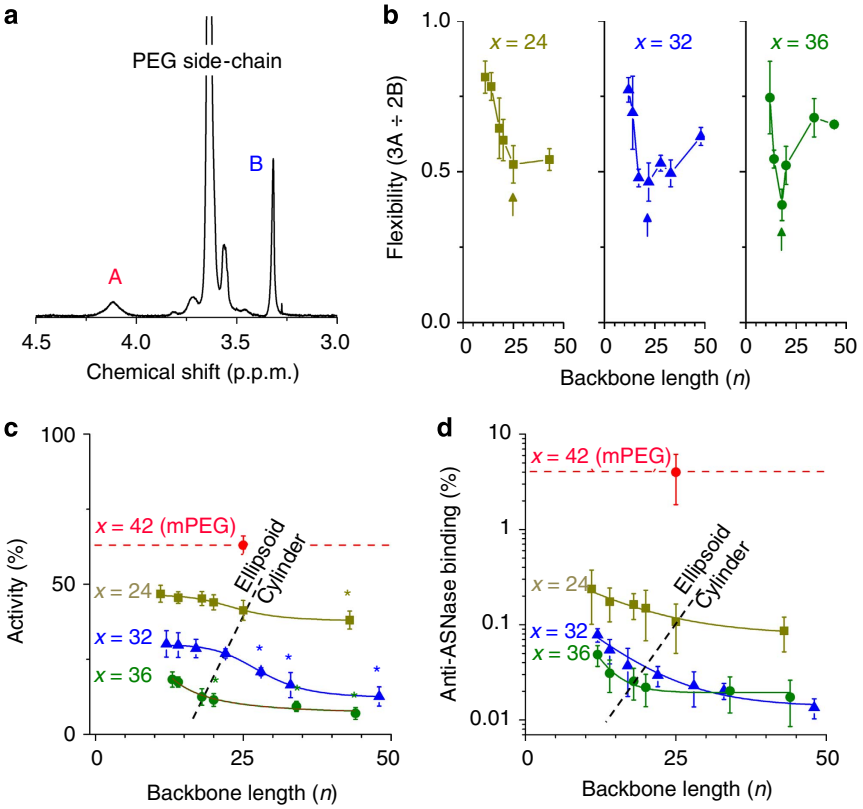

Figure 2 | Molecular sieving characteristics of pOEGMA–ASNase conjugates. (**a**) Representative ^{1}H NMR spectrum of a pOEGMA–ASNase conjugate with peaks corresponding to 'A' and 'B' from Fig. 1a identified. (**b**) Analysis of the flexibility *F* of the pOEGMA backbone permits the identification of the transition between ellipsoidal to cylindrical at the local minimum of the curve (arrow). (**c**,**d**) Enzymatic activity and anti-ASNase-binding affinity of ASNase–polymer conjugates, both relative to native ASNase, plotted as a function of polymer backbone length *n*. In **c**, star symbols indicate that the measured activity is statistically different from the value at lowest *n* (ANOVA, Tukey $P = 0.05$; Supplementary Table 2). The sigmoidal curve fit (**c**) and single exponential decay (**d**) used to fit the data are to guide the eye. mPEG–ASNase is shown as a line and a symbol in the centre of the graph for ease of comparison. Mean ± s.d. ($n = 3$).

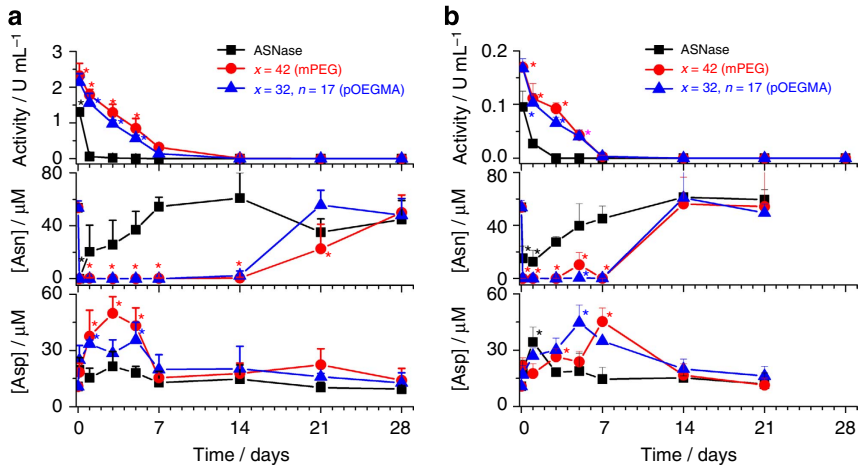

Figure 3 | Pharmacokinetics of ASNase and ASNase bio-conjugates. (**a**) 800 IU kg^{-1} or (**b**) 80 IU kg^{-1} of ASNase, mPEG–ASNase or pOEGMA–ASNase were administered and the catalytic activity, L-asparagine (Asn) concentration and L-aspartic acid (Asp) concentration monitored in blood samples taken at different intervals. The ASNase bio-conjugates showed similar profiles demonstrating that pOEGMA can convey long circulation to proteins, despite being in a compact conformation. Mean + s.d., $n = 3$. Stars denote statistically significant differences with respect to the natural ASNase activity of blood or to the initial concentration of Asn or Asp (Tukey, $P < 0.05$). When data points are superimposed, only a single star is shown for clarity.

at regular intervals from the tail vein for analysis of residual ASNase catalytic activity and for analysis of the concentration of Asn and Asp. Native ASNase was rapidly cleared from the body, as evidenced by the complete loss of activity within 1–2 days (Fig. 3a). Both mPEG–ASNase and pOEGMA–ASNase displayed sustained activity and depletion of blood Asn below the limit of detection (250 nM) for ca 14 days. At day 21, mPEG–ASNase was the only sample not to have reached its initial Asn concentration. The longer circulation time of mPEG–ASNase is consistent with its slightly larger hydrodynamic diameter (30 ± 5 and 25 ± 5 nm

for mPEG–ASNase and pOEGMA–ASNase, respectively) measured by dynamic light scattering. Thus, despite the expected compact conformation of the pOEGMA backbone in its ellipsoidal state, the hydrodynamic volume of the conjugate is sufficient for extended circulation. A transient increase of blood Asp was observed, consistent with the observations of others[28], indicating that depletion of Asn is occurring according to the expected catalytic mechanism. The observed difference between blood activity and Asn concentration could reflect distribution of the conjugate outside the blood compartment. A lower dose group, receiving 80 IU kg^{-1}, was also investigated and yielded comparable conclusions (Fig. 3b).

Epitope shielding *in vivo*. To assess the efficiency with which the polymers shielded epitopes on ASNase, BALB/c mice were immunized with either ASNase or ASNase bio-conjugates using aluminum hydroxide as adjuvant. Groups of five mice received 20 μg (protein content) of native ASNase, mPEG–ASNase or pOEGMA–ASNase (same conjugates as above) by subcutaneous injections. Analytes were administered on an equal weight (protein) basis to more easily compare their relative ability to generate immune responses. Different results might be expected if the analytes were administered on an equal activity basis, as a lower amount of more active analytes would be administered. For instance, as mPEG–ASNase is twice as active as the selected pOEGMA–ASNase, half as much of it would have been administered. It should also be noted that sensitization was promoted by an adjuvant to test immunogenicity in an accelerated way and that a much lower immune response is to be expected in its absence. Four injections were done with 2-week intervals. Blood was withdrawn on days 28, 42 and 71, and IgG titres towards either ASNase or the bio-conjugate itself were measured. In comparison to the native protein, immunization with mPEG–ASNase and pOEGMA–ASNase conjugates stimulated significantly lower anti-ASNase IgG (Fig. 4a,b; orange bars). The results also revealed that immunization with pOEGMA stimulated ~20-fold lower anti-ASNase IgG titres than immunization with mPEG–ASNase, and ~1,000-fold lower than with the native protein. To compare the relative levels of antibodies raised against the conjugates themselves, ELISA plates were coated with mPEG–ASNase or pOEGMA–ASNase (Fig. 4a,b; blue bars). The amounts of absorbed native ASNase and ASNase conjugates were verified in order to guarantee that the same amount of protein content was coated into each well, which permits comparisons to be made. On day 28, that is, 2 weeks after the second immunization, low titres of anti-mPEG–ASNase-specific IgG were determined, whereas no pOEGMA–ASNase-specific IgG was detected (Fig. 4a). On day 71, 1 month after four immunizations, low conjugate-specific IgG titres were detected for both formulations, but the titre was approximately 20 times lower in serum from mice immunized with pOEGMA–ASNase. Similar results were observed in serum taken on day 42 (Supplementary Fig. 5). These results demonstrate the effectiveness of the comb-shaped polymer in shielding epitopes of ASNase in the adaptive environment of the body. This result is also interesting in light of reports that antibodies can be raised against the polymer component (for example, mPEG) of bio-conjugates and mPEG–ASNase itself[29,30]. For robustness, the sensitization experiment was repeated by administrating a higher dose of analyte (200 μg protein per injection) into ASNase-naïve mice according to the same schedule as above. The tenfold increase in ASNase dose resulted in a general three- fourfold increase of IgG titres in all samples analysed, but again with pOEGMA–ASNase producing much lower titres than mPEG–ASNase and native ASNase (Supplementary Fig. 6).

Bioactivity of ASNase in ASNase-sensitized mice. Long-term treatment with ASNase can produce unwanted antibody responses against the enzyme. This may compromise the biological activity of the therapeutic enzyme. To assess the biological activity of ASNase in such a sensitization model, mice having received the multiple doses of ASNase, mPEG–ASNase or pOEGMA–ASNase according to the schedule above, then received an intra-peritoneal injection of 800 IU kg^{-1} of the corresponding ASNase formulation 4 weeks after the last of four immunizations. Before injection, Asn concentrations in blood were normal and the sensitizing ASNase preparations had no residual enzymatic activity. As seen in Fig. 4c, neither native ASNase nor mPEG–ASNase were able to maintain full depletion of blood Asn beyond the first 3 h after injection, whereas full depletion was still observed for pOEGMA–ASNase at day 3. Normal Asn levels were observed by day 7 for both native ASNase and mPEG–ASNase and by day 14 for pOEGMA–ASNase. Although the half-lives of both polymer–ASNase conjugates were significantly shorter than those observed in the non-sensitized animals, the longer circulation time of pOEGMA–ASNase vs mPEG–ASNase appears to reflect the lower immune response raised for this conjugate during sensitization and suggests that pOEGMA conveys better stealth-like characteristics to ASNase than does mPEG, even after repeated dosing.

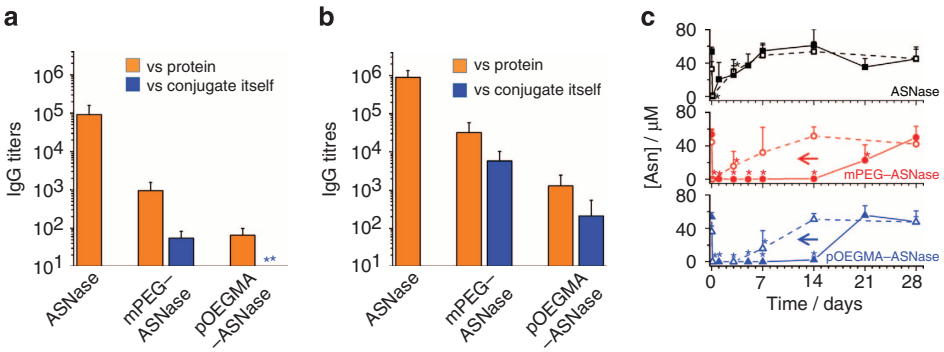

Figure 4 | Development of new antibodies *in vivo*. BALB/c mice were sensitized with either native ASNase, mPEG–ASNase ($x = 42$) or pOEGMA–ASNase ($x = 32$, $n = 17$). (**a**,**b**) IgG titres at days 28 and 71. Double stars indicates that signal in undiluted serum was undetectable. (**c**) Comparison of pharmacokinetic profiles of unsensitized (filled symbols, from Fig. 3a) and sensitized mice administered ASNase and ASNase bio-conjugates on day 72. Mean + s.d. ($n = 5$). Single star denotes statistically significant differences with respect to the natural concentration of Asn (ANOVA, Tukey, $P < 0.05$). When data points are superimposed, only a single star is shown for clarity. Horizontal arrow indicates shift of the curve because of sensitization.

Discussion

The desire to effectively shield enzymes with polymers, without compromising activity, has driven multiple systematic studies in which the influence of grafting density, polymer molecular weight, polymer type (that is, synthetic, natural), coupling chemistry and so on, have been examined[31,32]. However, studies that directly compare linear polymers to (related) branched ones are rare. In two important studies, Veronese and co-workers compared the activity, pH and temperature stability, and proteolytic digestion of ASNase (from *Erwinia Carotivora*) and three other enzymes modified with either linear mPEG or double-branched mPEG ($mPEG_2$)[33,34]. Although, for the most part, catalytic activity was similar for the mPEG and $mPEG_2$ bio-conjugates, all of the enzymes modified with $mPEG_2$ were more resistant to proteolysis. This is consistent with the more facile diffusion of small vs large molecules through the polymer coating, as observed herein. Furthermore, the antigenicity of the $mPEG_2$–ASNase conjugate was lower than for the mPEG analogue, although the difference was smaller than that observed herein. The present study expands upon these observations and emphasizes how controlling the molecular dimensions of the architecturally complex polymer pOEGMA beneficially reduces the immunogenicity of a subclass of biomolecules with diffusible small molecules as their substrates.

Dense pOEGMA coatings are well-known to efficiently repel the adsorption of proteins to solid surfaces, such as gold[35,36]. However, the application of this strategy to protect proteins themselves has met little attention. The dissuading dogma is the expected strong negative effect multiple polymer conjugation will have on the protein's bioactivity because of obstructed interaction with its binding partners, substrates and so on[31]. To our knowledge, Magnusson *et al.*[37] have presented the only *in vivo* study of the shielding efficacy of multiple pOEGMA chains on a protein, recombinant human growth hormone. The beneficial properties observed, however, were attributed to enhanced stability and prolonged pharmacokinetic profile, which counter-balanced the expected loss of activity, rather than to an intrinsic characteristic of nonlinear polymers or pOEGMA itself. Of course, the mechanism of action of recombinant human growth hormone involves receptor binding rather than enzymatic activity, which is probably why the relevance of the architecture of pOEGMA was not discussed. Other *in vivo* studies have focused on extending the circulation half-life of proteins with single pOEGMA chains[38–40]. Thus, the most significant contribution herein is the demonstration of the particularity of pOEGMA, which can be conveniently and rationally manipulated to address the dogma of loss of activity, even in the complex environment *in vivo*. This is an important finding because many non-human-derived proteins, including ASNase, possess numerous epitopes or enzyme-sensitive segments that can be responsible for treatment failure if they are not adequately shielded[41,42]. In fact, as ASNase is a homo-tetrameric protein, all epitopes are present in four identical copies. Thus, this type of protein absolutely requires multiple polymer conjugation because of the inability of a single (or a few) polymer chains to adequately shield these problematic parts of the protein[43,44]. Finally, it is worth considering that pOEGMA is attached to the protein via an amide bond and is unlikely to be released from the conjugates within the timeframe of the experiments performed. Ultimately, however, one would expect degradation of ASNase, which would release single pOEGMA chains connected to short peptide segments. Considering the molecular weight of the pOEGMA used (that is, $n=17$ is $\sim$8 kDa), it should ultimately be eliminated by, for example, renal filtration.

In summary, this study is the first *in vivo* demonstration of how polymer architecture, via the comb-shaped nature of pOEGMA, provides a unique design parameter for optimizing therapeutic proteins. The combined properties of effective epitope shielding with proportionately low loss of activity are inaccessible by conventional 'PEGylation' using linear polymers. Using ASNase as a model therapeutic protein, the designed pOEGMA bio-conjugate outperformed the mPEG–ASNase control (of similar catalytic activity) by being less immunogenic and providing a more sustained activity in sensitized animals. This shows promise for long-term therapies involving pOEGMA-modified proteins. Importantly, observations were consistent with predictions made from the phase diagram of protein-bound pOEGMA[12]. This guided the design of optimal semi-permeable coatings alongside convenient spectroscopic analysis of polymer conformation. This implies that one can easily design optimal pOEGMA coatings for proteins with little trial-and-error. One caveat is the limitation to therapeutic proteins that target soluble substrates small enough to penetrate through the pOEGMA coating. This makes the findings above most applicable to enzymes such as asparaginase, methioninase, arginine deiminase, arginase, uricase and so on[32]. Nevertheless, the presented strategy could also be used to protect and alter the circulation lifetime of emerging classes of therapeutics, such as small-molecule-binding proteins that could be used as drug scavengers[45], and create non-fouling coatings for biosensors that are specific towards small analytes.

Methods

ASNase pOEGMA–ASNase and mPEG–ASNase. *E. coli* ASNase was purchased from Afine Chemicals Ltd and de-salted before use. The synthesis, purification and characterization of ASNase bio-conjugates follow a robust procedure adapted from the original work of Lele *et al.*[22] and is described in detail in the Supplementary Methods.

***In vitro* catalytic activity.** ASNase and ASNase bio-conjugate catalytic activities were assayed by the formation of aspartate hydroxamate from Asn and hydroxylamine (aspartyl transferase activity). 20 µl of a 50 µg ml^{-1} (protein) aqueous enzyme solution were added to 1 ml Tris-HCl buffer (100 mM, pH 7.4) containing 20 µM Asn and 400 µM hydroxylamine. The mixture was incubated at 37 °C for 30 min, after which 700 µl of ferric chloride agent (5% ferric chloride, 1 M HCl, 4% trichloroacetic acid) were added. Aspartate hydroxamate forms a coloured complex with ferric chloride that can be quantified at 500 nm (ref. 46).

***In vitro* recognition by anti-ASNase antibodies.** Streptavidin-coated 96-well microplates (Pierce) were rinsed with 3 × 200 µl wash buffer (25 mM Tris, 150 mM NaCl, 0.25% bovine serum albumin, 0.05% Tween-20, pH 7.2) after which 100 µl of biotinylated anti-asparaginase antibody (10 µg ml^{-1}) wash buffer was added and incubated for 2 h room temperature. The wells were rinsed with 3 × 200 µl wash buffer after which 100 µl of serial dilutions of native ASNase (1 µg ml^{-1} to 1 pg ml^{-1}) were incubated for 30 min at room temperature to obtain a response curve. Thereafter, 100 µl of either mPEG–ASNase or pOEGMA–ASNase (1 µg ml^{-1}) were analysed in the same manner and the value compared with this response curve. The wells were rinsed with 3 × 200 µl wash buffer, and 100 µl horseradish peroxidase-labelled anti-asparaginase antibody (4 µg ml^{-1} in wash buffer) was added and incubated for 30 min. After a final rinse with 6 × 200 µl wash buffer, 100 µl 1-Step Slow TMB-ELISA Substrate Solution was added. After exactly 10 min, 50 µl 2 N HCl was added and absorbance of each well was measured at 450 nm.

Pharmacokinetics in naïve mice. All animal protocols were approved and conducted according to the guidelines of the Cantonal Veterinary Office Zurich. Groups of three female BALB/c mice (25 g) were administered either 80 or 800 IU kg^{-1} of ASNase, pOEGMA–ASNase ($x=32$, $n=17$) or mPEG–ASNase ($x=42$) in 100 µl sterile saline by intra-peritoneal injection. One international unit (IU) of activity is defined herein as the amount of enzyme that catalyses the formation of 1.0 mmol of Asp per min at 25 °C. Approximately 50 µl blood was sampled from the tail vein repeatedly over 28 days, and was immediately centrifuged for collection of serum that was stored frozen (− 80 °C) until analysed.

Sensitization and enzymatic activity in sensitized mice. Groups of five female BALB/c mice were immunized on days 0, 15, 29 and 43 by subcutaneous injections of 100 µl of a sterile saline solution containing either 20 or 200 µg protein content in ASNase, pOEGMA–ASNase ($x=32$, $n=17$) or mPEG–ASNase ($x=42$). All

vaccine preparations also contained 0.6 wt% Alhydrogel (Brenntag Biosector). Blood was collected on days 28, 42 and 71 as described above. On day 72, all mice from the low-dose groups were administered 800 IU kg^{-1} of the corresponding ASNase or ASNase bio-conjugate in 100 µl sterile saline by intra-peritoneal injection, and blood was sampled for measurement of Asn metabolism as described above.

Blood analysis. Bioactivity of native ASNase and polymer-modified ASNase was measured with an Asparaginase Activity Assay Kit (MAK007, Sigma-Aldrich) according to the manufacturer's recommended protocol. The concentrations of Asn and Asp in mice serum were analysed using pre-column derivatization high-performance liquid chromatography (Supplementary Figs 7 and 8) according to a method modified from Bidlingmeyer and described in the Supplementary Methods[47]. Blood antibody titres were measured by sandwich ELISA as described in the Supplementary Methods.

Statistics. Means from activity tests were compared by one-way ANOVA followed by a Tukey *post-hoc* test. Means from pharmacokinetics data were compared by one-way repeated-measures ANOVA followed by a Tukey *post-hoc* test. Differences were considered significant at $P<0.05$.

References

1. Harris, J. M. & Chess, R. B. Effect of pegylation on pharmaceuticals. *Nat. Rev. Drug Discov.* **2,** 214–221 (2003).
2. Pasut, G. & Veronese, F. M. State of the art in PEGylation: The great versatility achieved after forty years of research. *J. Control. Release* **161,** 461–472 (2012).
3. Alconcel, S. N. S., Baas, A. S. & Maynard, H. D. FDA-approved poly(ethylene glycol)-protein conjugate drugs. *Polym. Chem.* **2,** 1442–1448 (2011).
4. Duncan, R. The dawning era of polymer therapeutics. *Nat. Rev. Drug Discov.* **2,** 347–360 (2003).
5. Matyjaszewski, K. & Tsarevsky, N. V. Nanostructured functional materials prepared by atom transfer radical polymerization. *Nat. Chem.* **1,** 276–288 (2009).
6. Schmidt BVKJ, Fechler N, Falkenhagen, J. & Lutz, J.-F. Controlled folding of synthetic polymer chains through the formation of positionable covalent bridges. *Nat. Chem.* **3,** 234–238 (2011).
7. Kissel, P. *et al.* A two-dimensional polymer prepared by organic synthesis. *Nat. Chem.* **4,** 287–291 (2012).
8. Nguyen, T. H. *et al.* A heparin-mimicking polymer conjugate stabilizes basic fibroblast growth factor. *Nat. Chem.* **5,** 221–227 (2013).
9. Keefe, A. J. & Jiang, S. Poly(zwitterionic)protein conjugates offer increased stability without sacrificing binding affinity or bioactivity. *Nat. Chem.* **4,** 59–63 (2012).
10. Fuhrmann, G. *et al.* Sustained gastrointestinal activity of dendronized polymer–enzyme conjugates. *Nat. Chem.* **5,** 582–589 (2013).
11. Fuhrmann, G. & Leroux, J.-C. *In vivo* fluorescence imaging of exogenous enzyme activity in the gastrointestinal tract. *Proc. Natl Acad. Sci. USA* **108,** 9032–9037 (2011).
12. Liu, M. *et al.* Molecular Sieving on the Surface of a Protein Provides Protection Without Loss of Activity. *Adv. Funct. Mater.* **23,** 2007–2015 (2013).
13. Fu, C. H. & Sakamoto, K. M. PEG-asparaginase. *Expert Opin. Pharmacother.* **8,** 1977–1984 (2007).
14. Müller, H.-J. *et al.* Pharmacokinetics of native *Escherichia coli* asparaginase (Asparaginase medac) and hypersensitivity reactions in ALL-BFM 95 reinduction treatment. *Br. J. Haematol.* **114,** 794–799 (2001).
15. Hak, L. J. *et al.* Asparaginase pharmacodynamics differ by formulation among children with newly diagnosed acute lymphoblastic leukemia. *Leukemia* **18,** 1072–1077 (2004).
16. Avramis, V. I. *et al.* A randomized comparison of native *Escherichia coli* asparaginase and polyethylene glycol conjugated asparaginase for treatment of children with newly diagnosed standard-risk acute lymphoblastic leukemia: a Children's Cancer Group study. *Blood* **99,** 1986–1994 (2002).
17. Asselin, B. L. *et al.* Comparative pharmacokinetic studies of three asparaginase preparations. *J. Clin. Oncol.* **11,** 1780–1786 (1993).
18. Salzer, W. L. *et al.* Intensified PEG-L-asparaginase and antimetabolite-based therapy for treatment of higher risk precursor-B acute lymphoblastic leukemia: a Report From the Children's Oncology Group. *J. Pediatr. Hematol. Oncol.* **29,** 369–375 (2007).
19. Schrey, D. *et al.* Therapeutic drug monitoring of asparaginase in the ALL-BFM 2000 protocol between 2000 and 2007. *Pediatr. Blood Cancer* **54,** 952–958 (2010).
20. Murthy, N. S. & Knox, J. R. Small-angle X-ray scattering studies of *Escherichia coli* l-asparaginase. *J. Mol. Biol.* **105,** 567–575 (1976).
21. Lucon, J. *et al.* Use of the interior cavity of the P22 capsid for site-specific initiation of atom-transfer radical polymerization with high-density cargo loading. *Nat. Chem.* **4,** 781–788 (2012).
22. Lele, B. S., Murata, H., Matyjaszewski, K. & Russell, A. J. Synthesis of Uniform Protein – Polymer Conjugates. *Biomacromolecules* **6,** 3380–3387 (2005).
23. Cummings, C., Murata, H., Koepsel, R. & Russell, A. J. Tailoring enzyme activity and stability using polymer-based protein engineering. *Biomaterials* **34,** 7437–7443 (2013).
24. Murata, H., Cummings, C. S., Koepsel, R. R. & Russell, A. J. Polymer-Based Protein Engineering Can Rationally Tune Enzyme Activity, pH-Dependence, and Stability. *Biomacromolecules* **14,** 1919–1926 (2013).
25. Cummings, C., Murata, H., Koepsel, R. & Russell, A. J. Dramatically increased pH and temperature stability of chymotrypsin using dual block polymer-based protein engineering. *Biomacromolecules* **15,** 763–771 (2014).
26. Cheng, G. *et al.* Small angle neutron scattering study of conformation of oligo(ethylene glycol)-grafted polystyrene in dilute solutions: effect of the backbone length. *Macromolecules* **41,** 9831–9836 (2008).
27. Roth, P. J., Davis, T. P. & Lowe, A. B. Comparison between the LCST and UCST transitions of double thermoresponsive diblock copolymers: insights into the behavior of POEGMA in alcohols. *Macromolecules* **45,** 3221–3230 (2012).
28. Ho, D. H. *et al.* Polyethylene glycol-L-asparaginase and L-asparaginase studies in rabbits. *Drug Metab. Dispos.* **16,** 27–29 (1988).
29. Garay, R. P., El-Gewely, R., Armstrong, J. K., Garratty, G. & Richette, P. Antibodies against polyethylene glycol in healthy subjects and in patients treated with PEG-conjugated agents. *Expert Opin. Drug Deliv.* **9,** 1319–1323 (2012).
30. Armstrong, J. K. *et al.* Antibody against poly(ethylene glycol) adversely affects PEG-asparaginase therapy in acute lymphoblastic leukemia patients. *Cancer* **110,** 103–111 (2007).
31. Gauthier, M. A. & Klok, H.-A. Polymer-protein conjugates: an enzymatic activity perspective. *Polym. Chem.* **1,** 1352–1373 (2010).
32. Pasut, G., Sergi, M. & Veronese, F. M. Anti-cancer PEG-enzymes: 30 years old, but still a current approach. *Adv. Drug Deliv. Rev.* **60,** 69–78 (2008).
33. Veronese, F. M. *et al.* Improvement of pharmacokinetic, immunological and stability properties of asparaginase by conjugation to linear and branched monomethoxy poly(ethylene glycol). *J. Control. Release* **40,** 199–209 (1996).
34. Monfardini, C. *et al.* A branched monomethoxypoly(ethylene glycol) for protein modification. *Bioconjug. Chem.* **6,** 62–69 (1995).
35. Ma, H., Wells, M., Beebe, T. P. & Chilkoti, A. Surface-initiated atom transfer radical polymerization of oligo(ethylene glycol) methyl methacrylate from a mixed self-assembled monolayer on gold. *Adv. Funct. Mater.* **16,** 640–648 (2006).
36. Ma, H., Hyun, J., Stiller, P. & Chilkoti, A. 'Non-fouling' oligo(ethylene glycol)-functionalized polymer brushes synthesized by surface-initiated atom transfer radical polymerization. *Adv. Mater.* **16,** 338–341 (2004).
37. Magnusson, J. P., Bersani, S., Salmaso, S., Alexander, C. & Caliceti, P. *In situ* growth of side-chain peg polymers from functionalized human growth hormone—a new technique for preparation of enhanced protein – polymer conjugates. *Bioconjug. Chem.* **21,** 671–678 (2010).
38. Gao, W. P., Liu, W. G., Christensen, T., Zalutsky, M. R. & Chilkoti, A. *In situ* growth of a PEG-like polymer from the C terminus of an intein fusion protein improves pharmacokinetics and tumor accumulation. *Proc. Natl Acad. Sci. USA* **107,** 16432–16437 (2010).
39. Gao, W. P. *et al. In situ* growth of a stoichiometric PEG-like conjugate at a protein's N-terminus with significantly improved pharmacokinetics. *Proc. Natl Acad. Sci. USA* **106,** 15231–15236 (2009).
40. Ryan, S. M. *et al.* Conjugation of salmon calcitonin to a combed-shaped end functionalized poly(poly(ethylene glycol) methyl ether methacrylate) yields a bioactive stable conjugate. *J. Control. Release* **135,** 51–59 (2009).
41. Werner, A., Röhm, K.-H. & Müller, H.-J. Mapping of B-cell epitopes in *E. coli* asparaginase II, an enzyme used in leukemia treatment. In: *Biol. Chem.* **386,** 535–540 (2005).
42. Patel, N. *et al.* A dyad of lymphoblastic lysosomal cysteine proteases degrades the antileukemic drug l-asparaginase. *J. Clin. Invest.* **119,** 1964–1973 (2009).
43. Shaunak, S. *et al.* Site-specific PEGylation of native disulfide bonds in therapeutic proteins. *Nat. Chem. Biol.* **2,** 312–313 (2006).
44. Balan, S. *et al.* Site-specific PEGylation of protein disulfide bonds using a three-carbon bridge. *Bioconjug. Chem.* **18,** 61–76 (2006).
45. Tinberg, C. E. *et al.* Computational design of ligand-binding proteins with high affinity and selectivity. *Nature* **501,** 212–216 (2013).
46. Jayaram, H. N., Cooney, D. A., Jayaram, S. & Rosenblu, L. Simple and rapid method for estimation of L-asparaginase in chromatographic and electrophoretic effluents - comparison with other methods. *Anal. Biochem.* **59,** 327–346 (1974).
47. Bidlingmeyer, B. A., Cohen, S. A. & Tarvin, T. L. Rapid analysis of amino-acids using pre-column derivatization. *J. Chromatogr.* **336,** 93–104 (1984).

Acknowledgements

M.L. recognizes a doctoral scholarship from the Chinese Scholarship Council (CSC). Funding from the Sassella foundation (11/06) is gratefully acknowledged.

Author contributions

M.L., P.J., J.-C.L. and M.A.G. designed and conceived the study; M.L. synthesized and analysed all compounds. M.L. conducted all *in vivo* experiments with the help of F.Z. and P.J.; M.L., P.J., J.-C.L. and M.A.G. co-wrote the paper. All authors discussed the results and their implications, and commented on the manuscript at all stages.

Additional information

Supplementary Information accompanies this paper at http://www.nature.com/naturecommunications

Competing financial interests: The authors declare no competing financial interests.

Reprints and permission information is available online at http://npg.nature.com/reprintsandpermissions/

How to cite this article: Liu, M. *et al.* Semi-permeable coatings fabricated from comb-polymers efficiently protect proteins *in vivo*. *Nat. Commun.* 5:5526 doi: 10.1038/ncomms6526 (2014).

Molecular Sieving on the Surface of a Protein Provides Protection Without Loss of Activity

*Mi Liu, Pasquale Tirino, Milos Radivojevic, Daniel J. Phillips, Matthew I. Gibson, Jean-Christophe Leroux, and Marc A. Gauthier**

Tethering polymers to surfaces represents the cornerstone of a wide range of applications, including the stabilization of colloids/biomolecules and the preparation of functional coatings. Unfortunately, despite the prevalence of protein-tethered polymers in the pharmaceutical sector, the analysis of such polymer monolayers on a molecular level is difficult. In this work, simple ^{1}H NMR spectroscopy and the catalytic properties of α-chymotrypsin are used to analyze the conformational/permeability properties of protein-bound monolayers of poly(oligoethyleneglycol monomethylether methacrylate) (pOEGMA), a biocompatible comb-polymer of interest in the biomedical field. By analyzing >100 distinct conjugates of α-chymotrypsin and pOEGMA, a detailed picture of the behavior of pOEGMA on the surface of a protein was obtained. Remarkably, control of polymer conformation and inter-penetration produced a thus far overlooked molecular sieving effect. The application of this effect for the "smart" PEGylation of proteins is portrayed, from which insight is provided for the design of other therapeutic bioconjugates and functional coatings with selective permeability properties.

1. Introduction

Tethering polymers to surfaces represents the cornerstone of a wide range of applications, including the stabilization of colloids/biomolecules and the preparation of functional coatings.[1] For instance, the modification of therapeutic proteins with monolayers of linear poly(ethylene glycol) (PEG), a process referred to as PEGylation, is the current benchmark for increasing protein stability and for prolonging their circulation lifetime.[2] In many cases, the relative permeability of molecules through the polymer monolayer towards the surface is a crucial design parameter influencing efficacy. For example, PEG monolayers grafted to L-asparaginase, an enzyme used for the treatment of acute lymphoblastic leukemia,[3] should reject proteins from the immune system while simultaneously permitting the facile transit of the small substrate L-asparagine to the enzyme's active site.[2,4] Unfortunately, despite the prevalence of protein-tethered polymers in the pharmaceutical and biomedical sector, a detailed analysis of the permeability properties of such monolayers is difficult.[5]

In this work, simple ^{1}H NMR spectroscopy and the catalytic properties of α-chymotrypsin (αCT) were used to analyze the conformational/permeability properties protein-bound monolayers of poly(oligoethyleneglycol monomethylether methacrylate) (pOEGMA), a biocompatible polymer of current interest.[6] pOEGMA is an emerging comb-shaped derivative of PEG that possesses unique conformational properties which have lead to its use in peptide/protein PEGylation[7] and for the development of effective nonfouling coatings.[1g,1h] For instance, while PEG adopts a random coil conformation in solution, comb-polymers can behave either as compact ellipsoids or as (semi) rigid cylinders as a function of backbone and side-chain lengths.[8] Based on its solution behavior, it is hypothesized herein that the aspect ratio of pOEGMA can be accurately tuned on the surface of a protein to generate well-defined monolayers with potentially distinct permeability characteristics.

The conformation and packing of protein-bound pOEGMA monolayers was conveniently analyzed through >100 unique conjugates of pOEGMA and αCT by ^{1}H NMR spectroscopy and was correlated to the permeability characteristics of the polymer monolayer, established using the particular bioanalytical characteristics of αCT. More specifically, this protein displays catalytic activity towards substrates of differing size, which can be used to probe the influence of size on ease of access to the enzyme's catalytic site. Through the detailed molecular picture of the behavior of pOEGMA on the surface of a protein, new insight into the design of other therapeutic bioconjugates and non-fouling coatings with selective permeability properties is provided, which are of use in broad fields of application.

M. Liu, P. Tirino, M. Radivojevic,
Prof. J.-C. Leroux, Dr. M. A. Gauthier
Swiss Federal Institute of Technology Zürich (ETH Zürich)
Department of Chemistry and Applied Biosciences
Institute of Pharmaceutical Sciences
Wolfgang-Pauli Str. 10, 8093 Zürich, Switzerland
E-mail: M.A.G.marc.gauthier@pharma.ethz.ch
P. Tirino
Department of Chemistry "Paolo Corradini"
University Federico II
Via Cinthia, I-80126 Naples, Italy
D. J. Phillips, Prof. M. I. Gibson
Department of Chemistry
University of Warwick
Gibbet Hill Road, Coventry, UK

DOI: 10.1002/adfm.201202227

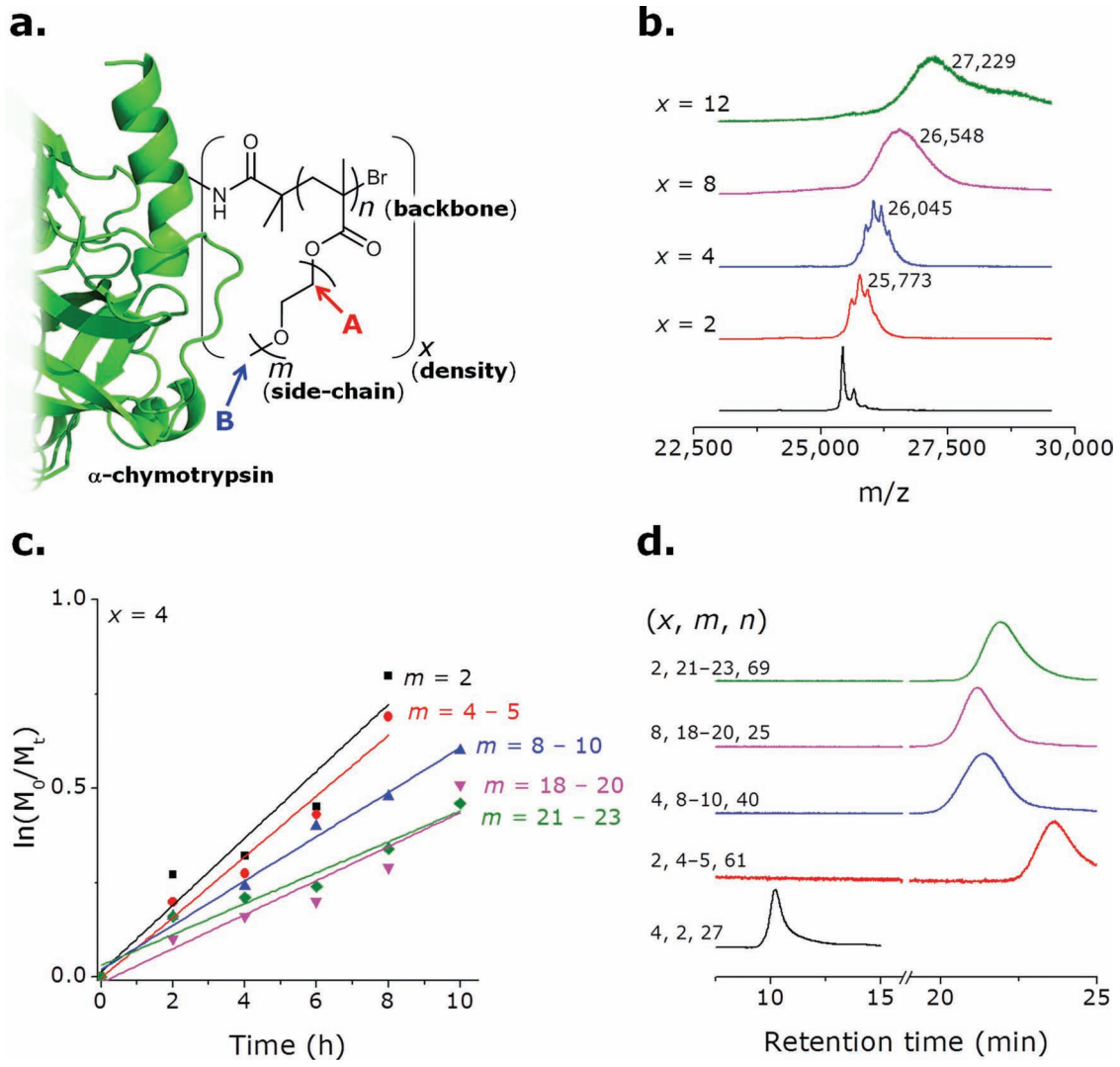

Figure 1. a) 3D parameter space (*x*, *n*, *m*) of αCT–pOEGMA conjugates. >100 unique αCT–pOEGMA conjugates were prepared by activation of αCT with 2-bromoisoburyryl bromide and in situ growth of pOEGMA chains by atom transfer radical polymerization. Analysis of prepared b) αCT macro-initiators and c,d) αCT–pOEGMA conjugates. b) Analysis of the molecular weight of αCT macro-initiators by MALDI-TOF MS to determine the average number of initiating groups covalently attached to the protein; c) Kinetics of the ATRP process. The polymerization reaction showed the characteristics of a living polymerization reaction with pseudo-first-order kinetics. In the figure, typical results obtained for $x = 4$ and the entire series of OEGMA monomers examined are presented. d) Typical SEC chromatograms of αCT–pOEGMA conjugates. All conjugates tested displayed monomodal molecular-weight distributions. Note that in this figure, all chromatograms were recorded in aqueous media, with the exception of the conjugate with $m = 2$, which was measured in DMF.

2. Packing and Conformation of pOEGMA within Protein-Bound Monolayers

As first reported by Matyjaszewski and co-workers,[9] a series of pOEGMA–protein conjugates were prepared by in situ growth of polymer chains directly from the surface of αCT (**Figure 1**a) by atom transfer radical polymerization, a powerful tool for the preparation of well-defined polymers and nanostructures.[10] This process yielded >100 well-defined conjugates with unique combinations of grafting density (*x*; number of polymer chains per protein), backbone length (*n*), and side-chain length (*m*) (Table S1–S8 in the Supporting Information). The grafting density was precisely varied ($x = 2$, 4, 8, and 12; Supporting Information Figure S1, Figure 1b) by controlling the number of initiating groups on the surface-exposed lysine residues of the protein. Digestion of the protein macro-initiators with trypsin followed by mass spectrometry failed to identify specific peptides preferentially modified with initiating groups (data not shown), suggesting random modification of the surface of αCT. The length of the oligoethylene glycol side-chain ($m = 2$, 4–5, 8–10, 18–20, and 21–23 oxyethylene units) was varied by selecting the appropriate OEGMA monomer, and the backbone length was varied between $n \approx 10$–100 monomeric units by sampling the living polymerization reaction at different times (Figure 1c, d). The conjugates were digested with pepsin, which is a more aggressive protease than trypsin and has the feature

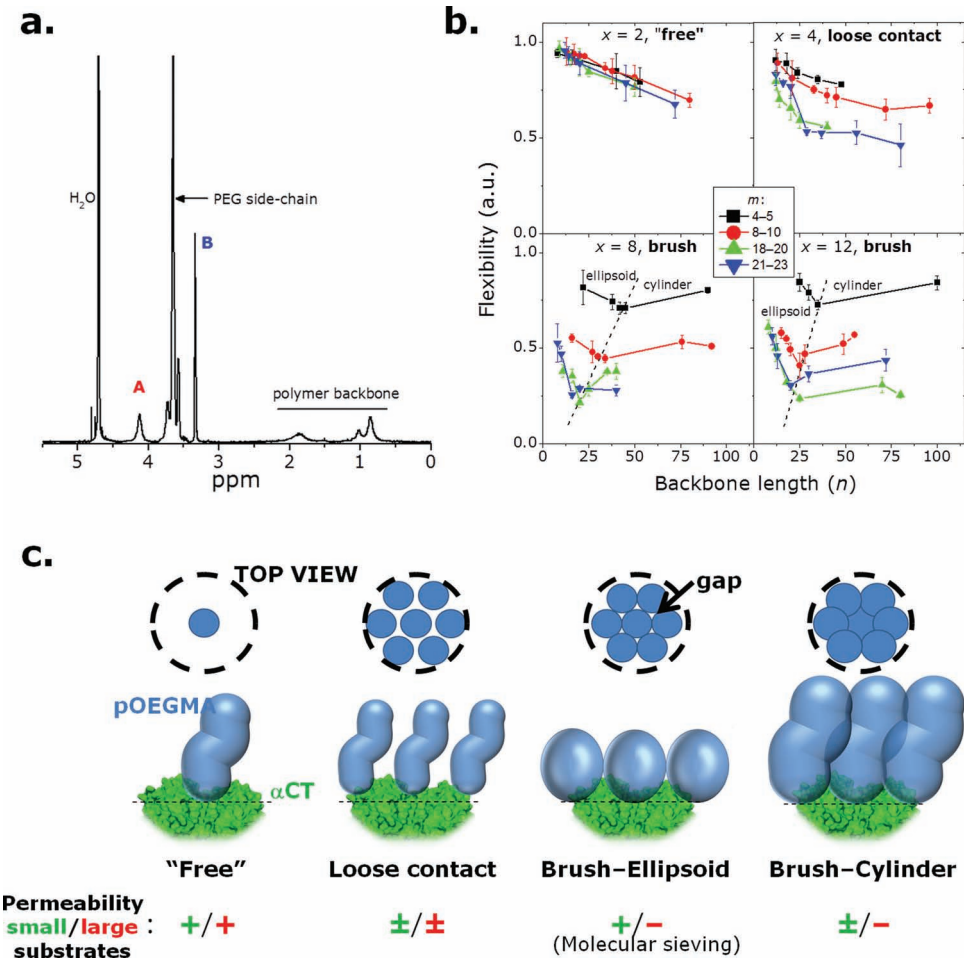

Figure 2. a) Analysis of backbone flexibility. Representative ^{1}H NMR spectrum of an αCT–pOEGMA conjugate for which polymer backbone flexibility was probed through the integral of peak A (proton at A in Figure 1a), normalized to the integral of peak B (proton at B in Figure 1a), which corresponds the most solvated and mobile group on pOEGMA. b) Conformation of protein-bound pOEGMA monolayers. Polymer backbone flexibility estimated by ^{1}H NMR spectroscopy provides insight into the conformation and organization of pOEGMA within protein-bound monolayers. Increasing grafting density led to a pronounced loss of flexibility signaling a transition from highly mobile pOEGMA chains ($x = 2$) to a dense brush-like pOEGMA monolayer ($x \geq 8$). In the brush regime, it is hypothesized that transitions of the pOEGMA chains from ellipsoidal to cylindrical take place to minimize inter-chains interactions within the monolayer. Mean ± SD (n = 3). c) Cartoon illustrating the idealized organization and selective permeability characteristics of the four different regimes observed within the 3D parameter space of protein-bound pOEGMA examined.

of being able to hydrolyze amide bonds within proteins but not ester bonds.[11] This digestion produced pOEGMA–peptide fragments (Supporting Information Figure S2) with an average molecular weight consistent with the molecular weight of the parent αCT–pOEGMA conjugate divided by the number of initiator groups. This suggests that initiation of polymerization occurred at all expected sites on the protein, and the all polymer chains have comparable lengths (monomodal distribution).

To analyze the conformation and packing of pOEGMA on the surface of the protein, the flexibility of the polymer backbone was probed by ^{1}H NMR spectroscopy. It is commonly observed that a decrease of molecular mobility leads to a loss of signal due to changes of the characteristic relaxation times of protons within the polymer.[12] Thus, a simple ^{1}H NMR spectrum recorded under typical conditions used for small molecules contains semi-quantitative information on the average (relative) flexibility at different locations on the polymer without the hassle of a more laborious analysis of the actual relaxation times and their distribution within a given polymer. This feature was exploited herein to compare the relative flexibility of the first side-chain methylene group adjacent the polymer backbone (Peak A, in **Figure 2**a) versus the terminal methyl group on the side-chains (Peak B, in Figure 2a), which is expected to be the most solvated and free group on pOEGMA. A dimensionless flexibility factor F, defined as $F = A \div 2/3B$, was calculated for each conjugate. F can vary from a value of 1 for a fully flexible and solvated polymer backbone and tend towards 0 when it is rigid, extended, and/or collapsed.

At low grafting density ($x = 2$) flexibility was initially high ($F \approx 1$) and decreased linearly with n, independently of side-chain length (Figure 2b). This suggests that the protein-tethered polymer chains are essentially "free" and behave independently of one another on the surface of the protein (Figure 2c). At this grafting density, conformational changes from ellipsoid to cylinder, while expected based on the behavior of related polymers,[8] did not lead to a discernible feature in the graph of F versus n.

At intermediate grafting density ($x = 4$) F was again initially high (≈1) at low n, indicating that the chains remain loosely spread on the surface of the protein. As n increased, a more pronounced decrease of F compared to that observed for $x = 2$ was observed due to partial contact between the polymer chains. The decrease of flexibility was more pronounced for polymers with longer side-chain lengths m, as expected from the larger "footprint" of these polymers. Globally, the polymer chains are in a "loose contact" regime (Figure 2c) whereby interactions between protein-bound pOEGMA chains partially restrict their freedom.

At high grafting density ($x = 8$, 12), the initial flexibility of the backbone (at low n) was $0.5 < F < 0.8$, signaling strong contact between the pOEGMA chains. Such interactions should force the longest dimension of the polymer along an axis perpendicular to the surface, i.e., the so-called brush regime for surface-tethered polymer monolayers.[13] F strongly decreased linearly versus n to a minimal value at n = 20–40, then increased linearly at a more moderate slope with respect to n (Figure 2b). This plot provided an indication that at this minimal value, pOEGMA changes conformation to minimize inter-polymer contacts. Indeed, conformational differences as a function of n have been observed for other comb-polymers such as poly(styrene)-*g*-oligo(ethylene glycol), which undergo ellipsoid to cylinder transitions with increasing n.[8] The putative interpretation put forth herein is that the pOEGMA chains, which initially behave as compact and non-interpenetrated ellipsoids at low n, change conformation to cylinders beyond n = 20–40. This slightly decreases the footprint of the polymer on the surface of the protein, but promotes side-chain interpenetration between neighboring chains. For dilute solutions of poly(styrene)-*g*-oligo(ethylene glycol), such a transition has been shown to occur between n = 8–40,[8] a value which is compatible with the interpretation put forth above. The n at which the transition from ellipsoid to cylinder was observed herein decreased with increasing m as well as increasing x (dashed lines in Figure 2b), which corroborates the interpretation that confinement of the pOEGMA chains within the dense monolayer is driving the change of backbone conformation.

3. Selective Permeability of Protein-Bound pOEGMA Monolayers

αCT displays catalytic activity towards substrates of differing size. Consequently, analysis of the activity of αCT–polymer conjugates towards substrates including a single amino acid derivative (benzoyl-L-tyrosine *p*-nitroanilide (BT*p*NA), 405 Da), to a peptide (*N*-Succinyl-Ala-Ala-Pro-Phe *p*-nitroanilide, 625 Da), to a protein (casein, 19–25 kDa) provides information on the relative ease of diffusion of the substrates towards the active site of αCT within the conjugate. Note that the catalytic site on αCT is the same for all three substrates. Hydrolysis of all three substrates involves cleavage of an amide bond, and the substrates differ significantly in molecular weight. To identify regions of preferential activity towards smaller substrates, an "activity ratio" was calculated by dividing the activity of the conjugates towards either BT*p*NA (**Figure 3**a) or the peptide substrate (Figure 3b) by the activity towards casein, all measured using established protocols based on the kinetics of substrate hydrolysis. An alternative presentation of data can be found in Supporting Information Figure S3. The raw activity values for all conjugates towards all substrates can be found in Supporting Information Table S1–S8 and are plotted as a map in Figure S4.

At low grafting density ($x < 8$; i.e., in the "free" and loose contact regimes), none of the conjugates displayed any particular preference for small or large substrates, as indicated

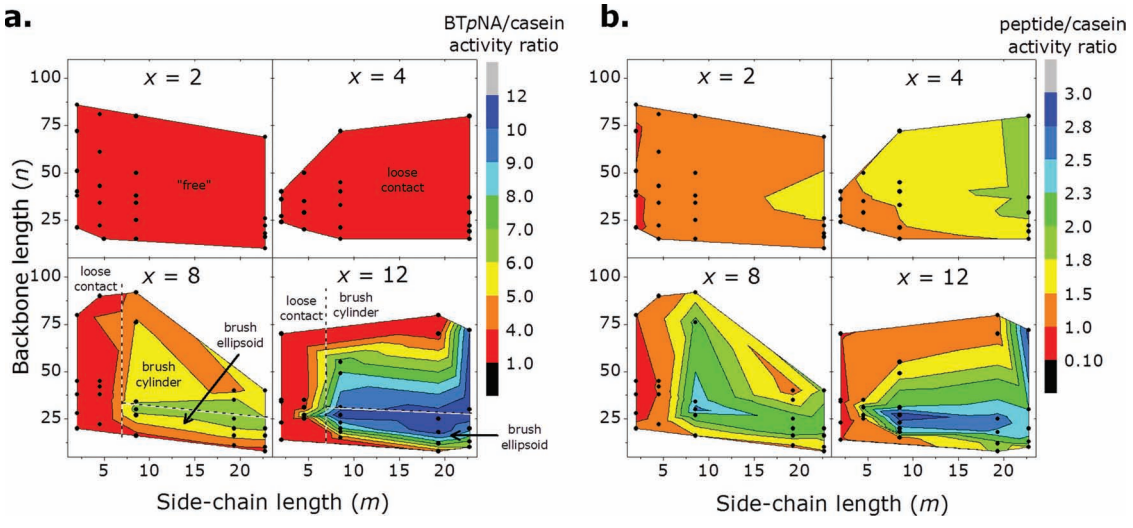

Figure 3. Molecular sieving of protein-bound pOEGMA monolayers. Regions of preferential activity towards small substrates such as a) BT*p*NA or b) peptide compared to large substrates (casein), were observed at room temperature by comparing the relative activities of each individual conjugate towards the three substrates. For $x \geq 8$, the brush–ellipsoid regime determined by NMR spectroscopy coincides with regions showing strong preferential activity towards small substrates (in blue). Color maps established as linear projections between data-points (black dots are the mean of n = 3). Absolute activity values are found in Supporting Information Table S1–S8 and Figure S5 as Mean ± SD (n = 3).

by activity ratios close to 1 (Figure 3a,b top). However, at high grafting density (x = 8, 12; i.e., in the brush regime) a zone of preferential activity towards small substrates was observed for n < ≈35–40 (Figure 3a,b bottom). In this region, the preferential activity ratio reached a maximum of ≈10 for BT*p*NA ÷ casein and ≈3 for peptide ÷ casein. Interestingly, this zone (defined by x, n, and m) coincided with the pOEGMA monolayer being in a brush–ellipsoid conformation (Figure 2b) and was observed for both BT*p*NA and the peptide substrate, indicating that this phenomenon does not result from specific substrate–conjugate interactions. The lower preferential activity ratio observed for the peptide substrate (versus BT*p*NA) further points to a size-dependence of the phenomenon. From these experiments, it appears that protein-bound pOEGMA monolayers in brush–ellipsoid conformation possess pronounced selective permeability, or "molecular sieving" properties. Similar results were obtained at 37 °C (Supporting Information Figure S5).

4. Phenomenological Interpretation

The "molecular sieving" properties observed in the brush–ellipsoid regime result from the formation of a densely packed monolayer of compact ellipsoids on the surface of αCT. In contrast to monolayers with lesser inter-pOEGMA interactions (i.e., in the "free" and loose contact regimes, Figure 2c), the dense brush–ellipsoid monolayers effectively block the passage of biomacromolecules (Supporting Information Figure S4), despite the fact that the length of the backbone is quite low (n < 20–40). The ellipsoidal shape of the pOEGMA chains, as illustrated conceptually in Figure 2c as hexagonally packed hard circles, yield a comparatively small barrier to permeation by small molecules, likely due to the presence of finite gaps within monolayer between polymer chains. Such gaps are observed in the 2D hexagonal packing of non-interpenetrated circles and can account for down to ≈9% of the surface area.[14] The gaps should be smallest just prior to the transition of the pOEGMA chains from ellipsoids to cylinders (i.e., strongest inter-polymer interactions), and is consistent with the maximum preferential activity towards small substrates observed in this region. By changing conformation from ellipsoidal to cylindrical, the inter-penetration of polymer side-chains closes these gaps, thus yielding an effective diffusion barrier to small and large molecules alike, as a function of their hydrodynamic radius.

The pOEGMA monolayers in the "free" and loose contact regime were obtained at low grafting densities and mainly when the side-chains were short (m ≤ 4–5). For these more disordered monolayers, trends comparable to those observed for linear polymers were observed. That is, permeability towards small and large molecules alike was restricted with increasing grafting density and pOEGMA backbone length.[15] The lack of significant preferential activity towards small molecule substrates is consistent with the observations made with a conjugate of αCT bearing 9–10 chains of linear 5 kDa PEG chains (≈1.8 for BT*p*NA ÷ casein and ≈1.2 for peptide ÷ casein; Supporting Information Table S9). It should be noted that higher degrees of modification with linear PEG were not possible. Protein-bound linear PEG is expected to adopt a random-coil or a mushroom conformation depending on grafting density.[16] Assuming αCT to be a sphere with a 2-nm radius,[17] the brush–ellipsoid regime was observed at grafting densities of one pOEGMA chain per 4.2–6.3 nm^2 (x = 12 and 8, respectively) in combination with m ≥ 8–10 and n ≤ ≈35–40. These guidelines, in combination with analysis by ^{1}H NMR spectroscopy (when possible for soluble conjugates), should be used to prepare molecular sieving coatings for other applications.

5. Molecular Sieving for "smart" PEGylation

In addition to the comb polymers discussed above, other architecturally complex polymers such as double-branched PEG, polysaccharides, and hyperbranched polymers have shown beneficial properties for the modification of proteins.[15,18] Unfortunately, little systematic modulation of the structure of these polymers has been examined. In a recent study, Wurm et al.[18] have observed only a small effect of polymer architecture on bioactivity within a library of hyperbranched poly(glycerol)–protein conjugates. In their study however, grafting density is quite low and their findings corroborate those herein at low grafting densities. It therefore appears evident that manifestations of polymer architecture on protein bioactivity only become pronounced at very high grafting densities, where inter-polymer interactions direct organization of the polymer within the monolayer.

To assess the usefulness of specific zones within the conformation diagram of protein-bound pOEGMA monolayers for the PEGylation of proteins, the catalytic activity of selected conjugates towards BT*p*NA was measured in the presence of α_1-antichymotrypsin (α_1-antiCT), a competitor for the active catalytic site on the protein.[19] This glycoprotein is known to bind αCT in a strong 1:1 complex devoid of catalytic activity and was used herein to simulate recognition by biomacromolecules, such as immune system components or proteases. As seen in **Figure 4**, one equivalent of α_1-antiCT completely inhibited the

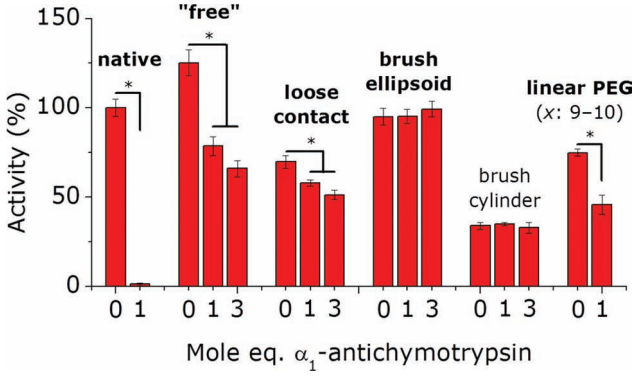

Figure 4. "Molecular sieving" for "smart" PEGylation of proteins. The competition of α_1-antiCT for the active site of αCT was examined as model for recognition by biomolecules such as immune system components. The inhibitory effect of α_1-antiCT was observed for all αCT–polymer conjugates, except for those within the brush regime. The conjugate in the brush–ellipsoid regime possessed the full catalytic activity of the native enzyme, despite being modified with 12 polymer chains. Mean ± SD (n = 3). Samples analyzed: "free" (x = 4, n = 25, m = 8–10); loose contact (x = 12, n = 35, m = 4–5); brush–ellipsoid (x = 12, n = 25, m = 8–10); brush–cylinder (x = 12, n = 55, m = 8–10). (Star denotes statistically significant difference at p = 0.05). x is the grafting density of the polymer on the surface of the protein.

activity of the native enzyme. As α_1-antiCT is a large molecule (≈68 kDa), it was rationalized that the polymer monolayers could, in certain conformations, selectively block this protein, while nevertheless admitting a small molecule substrate to the active site of αCT. Four αCT–pOEGMA conjugates were selected from within different parts of the conformational diagrams above as representative of "free", loose contact, brush–ellipsoid, and brush–cylinder regimes (see figure caption for specific *x*, *n*, *m* of the conjugates). Based on the results from the previous sections, the first two conjugates were expected to be sensitive to α_1-antiCT while the latter two not. The results presented in Figure 4 confirm this expectation. Remarkably, due to the "molecular sieving" effect discussed above, the conjugate in the brush–ellipsoid regime displayed ≈100% of the catalytic activity of the native enzyme, despite the fact that it bore 12 polymer chains, and was completely insensitive to α_1-antiCT. The conjugate in the brush–cylinder regime displayed similar properties, but had lower activity due to closure of the gaps between the POEGMA chains. These results corroborate similar findings from above (Figure 3).

As a control, a conjugate of αCT bearing 8–9 linear chains of PEG also showed a marked decrease of activity upon addition of as little as 1 eq. of α_1-antiCT (Figure 4). Comparable results were observed for the other two substrates (Supporting Information Figure S6). It should be noted that the activity of certain conjugates towards BT*p*NA was higher than 100%. This phenomenon has been previously reported for trypsin as resulting from a micro-environmental effect.[20] These combined results indicate protein-bound pOEGMA monolayers within the brush–ellipsoid conformation are of significant interest for the PEGylation of proteins whose activity involves small molecules, which includes the ever expanding list of anticancer enzymes.[2a] It should be noted that some of the enzymatic activity tests were performed in the presence of small amounts of organic solvent (DMF, DMSO; for substrate solubility), which may potentially influence polymer conformation. Nevertheless, the correspondence between transitions observed in the activity maps (Figure 3) and polymer conformation (in pure aqueous media, Figure 2b), in addition to the corroborating evidence for molecular sieving from Figure 4, appears to rule out a strong influence of these amounts of organic solvent on the results presented.

6. Temperature-Induced Conformational Changes to Protein-Bound pOEGMA

pOEGMA is a thermo-sensitive polymer[6b] that undergoes a coil to globule transition at a temperature known as the cloud-point, which is influenced by the length of the side-chain *m*, though not that of the backbone,[6b,21] and concentration.[21] To rule out the influence of thermo-sensitivity on the transitions observed above, the cloud-points of all conjugates were measured. This was deemed particularly necessary considering that the high grafting density of pOEGMA on the protein creates an artificially high local concentration of polymer, which should depress the cloud-point of these polymers significantly, as observed on particle surfaces elsewhere.[22] Stimuli-sensitive protein–polymer conjugates are notably receiving increasing interest in a variety of fields.[23] The cloud-points measured for the conjugates were consistent with those previously reported for pOEGMA in solution[6b,21] (Supporting Information Table S10 and **Figure 5**a) and were all well above 37 °C, with the exception of αCT–pOEGMA conjugates with *m* = 2, which had cloud points ≈20–30 °C. These low values prompted their exclusion from the flexibility analysis shown in Figure 2b owing to possible misinterpretation. Increasing the grafting density of αCT–pOEGMA conjugates (*m* = 8–10) from *x* = 2 to 12 lead to an impressive depression of the cloud-point by ≈20 °C (Figure 5b), confirming the high local concentration of pOEGMA on the surface of αCT.[21] Overall, the thermo-sensitivity of pOEGMA can be ruled out as cause for the transitions observed in Figure 2b.

7. Conclusions

This work constitutes the first elucidation of the conformation/permeability diagram of protein-bound pOEGMA monolayers

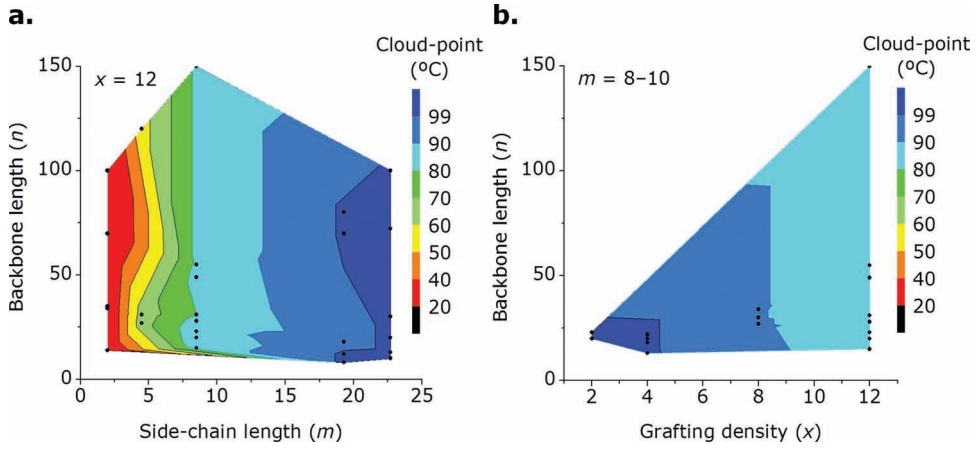

Figure 5. Thermo-sensitivity of αCT–pOEGMA conjugates. a) The cloud-point of αCT–pOEGMA conjugates decreased with increasing *m*, though was largely independent of *n*. b) The cloud-point of αCT–pOEGMA conjugates decreased with grafting density *x*. Color maps established as linear projections between data-points (black dots are the mean of n = 3).

and provides a detailed and systematic investigation of how the aspect ratio of protein-tethered polymers can be modulated to predictably tune protein bioactivity. ^{1}H NMR spectroscopy was a simple, rapid, and accessible tool for screening the conformational state of protein-bound pOEGMA. As the permeability of most pOEGMA monolayers cannot be analyzed in the same fashion as for αCT herein (i.e., due to a lack of substrates of differing size), NMR spectroscopy should serve as a tool of importance for directing monolayer design towards the brush–ellipsoid regime through the flexibility factor *F*. This regime showed a not previously described molecular sieving effect which is inaccessible using other modern PEGylation strategies or using conventional linear polymers.[15,24] This study points notably to the importance of grafting density and opens the door for more systematic evaluations of surface-bound polymer monolayers with complex architectures. The guidelines established herein may be applicable to other proteins for the development of new optimized therapeutic agents and stress the yet largely untapped parameter of polymer architecture in bioconjugate design. In addition, the same guidelines provide insight into the design of other functional coatings with selective permeability to small molecules for wide-ranging applications in the biomedical field.

8. Experimental Section

Materials: 2-Amino-2-hydroxymethyl-propane-1,3-diol (Tris), calcium chloride, α-chymotrypsin (αCT) from bovine pancreas, α_1-antichymotrypsin (human), sodium phosphate dibasic anhydrous and di-sodium hydrogen phosphate were purchased from AppliChem (Axon Lab AG) and used as received. 2,2′-bipyridine, 2-bromoisobutyryl bromide, copper(I) bromide, copper(II) bromide, α-cyano-4-hydroxycinnamic acid, dithiothreitol (DTT), guanidinium HCl, iodoacetamide, milk casein (sodium salt), *N*-benzoyl-L-tyrosine *p*-nitroanilide (BT*p*NA), *N*-succinyl-Ala-Ala-Pro-Phe *p*-nitroanilide, oligoethylene glycol monomethyl ether methacrylate (OEGMA; average M_n: 188, 300, 475, 950, 1100 Da), pepsin (2188 U mg^{-1} protein), sinapinic acid, trichloroacetic acid, trifluoroacetic acid (TFA), and trypsin were purchased from Sigma-Aldrich (Buchs, Switzerland) and used as received. Deuterium Oxide was purchased from Cambridge Isotope Laboratories and used as received. All solvents were of the purest grade available.

Equipment: Organic analytical size-exclusion chromatography (SEC) measurements were performed in DMF containing 0.01 M LiBr using a Viscotek TDAmax system (Viscotek, Houston, TX) equipped with a differential refractive index detector, a low-angle light-scattering detector, and a right-angle light-scattering detector. Absolute molecular weights were reported. Separation was achieved using two Viscotek columns (CLM 3047) in series at a flow rate of 1 mL min^{-1} at 45 °C. Aqueous SEC measurements were performed in 100 mM phosphate buffer (pH = 6.8) using a Viscotek TDAmax system (Viscotek, Houston, TX) equipped with differential refractive index detector, a low-angle light-scattering detector, and a right-angle light-scattering detector. Absolute molecular weights were reported. Separation was achieved using three Viscotek columns (CLM 3016) in series at a flow rate of 0.7 mL min^{-1} at 35 °C. Activity tests were conducted using an Infinite M200 microplate reader (Tecan Ltd.). An Ultrafextreme instrument (Bruker) was used in linear mode for MALDI-TOF MS analysis.

Preparation of αCT Macro-Initiators: αCT macro-initiators were prepared following a modified procedure from Lele et al.[9a] αCT (500 mg, 0.02 mmol of protein; 0.28 mmol of ε-NH_2 groups in lysine residues) was dissolved in 100 mM phosphate buffer (50 mL, pH 8). An appropriate amount of 2-bromoisobutyryl bromide (10–250 eq. relative to protein) dissolved in chloroform was added drop-wise to the vigorously stirred enzyme solution. The mixture was allowed to react at 4 °C for 30–150 min and the pH of the reaction mixture was maintained at 7.5–8 by addition of 100 mM NaOH. The degree of modification was altered by changing the concentration of 2-bromoisobutyryl bromide. After reaction, the solution was centrifuged to remove any precipitate and then the activated proteins were purified by preparative SEC (Sephadex G-25) followed by centrifugal dialysis against water for (MWCO 10 kDa). Purified αCT macro-initiators were isolated by freeze-drying and stored at –20 °C until used. To determine the number of initiators covalently connected to αCT, the purified macro-initiators were dissolved in 50 μL water containing 0.1% TFA. 1 μL of this solution was mixed with 1 μL of matrix (saturated sinapinic acid in 50% acetonitrile containing 0.1% TFA), the mixture spotted on the target, and then analyzed by MALDI TOF MS using α-cyano-4-hydroxycinnamic acid as matrix (≈5 mg mL^{-1} in 50% acetonitrile containing 0.1% TFA); Figure 1b. The average number of initiators present was determined by dividing the increase of molecular weight relative to the native protein by 150 Da, the molecular weight of the initiating group. Selected samples were also dissolved in acetonitrile:water 1:1 (v/v) and analyzed by nano-electrospray mass spectrometry, which yielded comparable results to those obtained by MALDI TOF MS. Good control over the grafting density was achieved by controlling the amount of acylating agent added (Supporting Information Figure S1).

Analysis of Location of Initiator Groups by Tryptic Digestion/Mass Spectrometry: Tryptic digestion LC-MS was performed under contract by the *Protein Analysis Group* at the *Functional Genomics Center Zurich*. Native αCT and αCT macro-initiators (≈0.1 mg) were dissolved in 20 μL 6 M guanidinium HCl (pH 8) and then 2 μL 500 mM DTT was added. The mixture was incubated at 37 °C for 1 h. To the reduced samples, 1.5 μL iodoacetamide was added and the mixture left in the dark for 30 min at 37 °C. 10 μL of the solution of alkylated protein was then added to 450 μL buffer (10 mM Tris, 2 mM $CaCl_2$, pH 8.2), 100 μL trypsin (0.01 μg μL^{-1} in 10 mM Tris, 2 mM $CaCl_2$, pH 8.2), and 60 μL acetonitrile. The digestion was allowed to proceed for 2 h at 50 °C. The digested samples were analyzed by MALDI TOF MS using α-cyano-4-hydroxycinnamic acid as matrix (5 mg mL^{-1} in 50% acetonitrile containing 0.1% TFA). Despite careful comparative analysis of sequence coverage between the native and a sparingly modified αCT derivative (x = 2), dominant fragments unambiguously modified with 2-bromoisobutyryl bromide were not found. This result points to a random distribution of initiator groups on αCT rather than the preferential modification of specific locations on the protein.

In Situ Growth of Polymer Chains from αCT Macro-Initiators: Atom transfer radical polymerization (ATRP) was used to grow pOEGMA chains from the αCT macro-initiators in a modified procedure from Lele et al.[9a] In a typical reaction, 50 mg of αCT macro-initiator (0.002 mmol protein; 0.004 mmol initiators, 1 eq.) and OEGMA (0.4 mmol, 100 eq.) were placed in a sealed round-bottom flask containing 15 mL 100 mM phosphate buffer (pH 6) and the solution de-oxygenated under a flow of argon. This solution was transferred to a second sealed flask containing CuBr (2.9 mg, 0.02 mmol, 5 eq.), $CuBr_2$ (4.4 mg, 0.02 mmol, 5 eq.), and 2,2′-bipyridine (9.4 mg, 0.06 mmol, 15 eq.) to initiate the polymerization reaction. The polymerization was allowed to proceed at 4 °C, and at given time points aliquots were extracted using degassed syringes. The aliquots were exposed to air to quench the polymerization reaction and diluted in D_2O to measure monomer conversion by ^{1}H NMR spectroscopy (Figure 1c). After analysis by ^{1}H NMR spectroscopy, the αCT–pOEGMA conjugates were purified by centrifugal dialysis (MWCO 30 kDa). When the expected molecular weight of the conjugate was below 30 kDa, purification was achieved by silica gel chromatography. The complete numerical characteristics of all αCT–pOEGMA conjugates (x, m, n) are listed in Supporting Information Table S1–S8.

Analysis of Molecular Weight of αCT–pOEGMA Conjugates: Owing to the difficulty in analyzing the molecular weight of protein–polymer conjugates, this parameter was determined by three complementary techniques: ^{1}H NMR spectroscopy, SEC, and by UV-vis spectrometry. The molecular weights determined by these methods are listed in Supporting Information Table S1–S9 at the end of this document. ^{1}H

NMR spectroscopy: Because characteristic peaks of αCT could not be observed in the ^{1}H NMR spectra of purified αCT–pOEGMA conjugates, the molecular weight of the latter was determined based on monomer conversion and the known initial ratio of αCT to OEGMA; SEC: The molecular weight and molecular weight distribution of αCT–pOEGMA was analyzed by aqueous SEC for conjugates with $m \geq 4$–5, whereas conjugates with shorter m were analyzed by SEC in DMF. Typical chromatograms are shown in Figure 1d. UV-vis spectroscopy: The molecular weight of αCT–pOEGMA was determined by dissolving known amounts of purified conjugates in distilled water, and then determining the concentration of αCT in this solution by measuring the absorbance at 280 nm. pOEGMA does not absorb significantly at this wavelength and thus does not interfere with quantification of molecular weight in this manner. All three analytical techniques yielded comparable values of molecular weight.

Analysis of Initiation Efficiency of αCT Macro-Initiators: To analyze the efficiency of the initiation process, the molecular weight of the individual pOEGMA chains were analyzed after digestion of a conjugate by pepsin. This enzyme is known to hydrolyze amide bonds, but not affect ester bonds. Indeed, incubation of 10 mg of free pOEGMA (i.e., not attached to a peptide or protein) in 3 mL 100 mM citric acid buffer (pH 3) with 2 mL of pepsin (5 mg mL^{-1} in 100 mM citric acid buffer, pH 3) at 37 °C over a 24 h period did not alter the SEC chromatogram of this polymer (Supporting Information Figure S2a). In contrast, over a 70 h period, the peak in the SEC chromatogram of a selected αCT–pOEGMA (*x*, *m*, *n*: 4, 8–10, 80), which was pre-denatured at 95 °C for 10 min, shifted to lower molecular weight and remained monomodal (Supporting Information Figure S2b). The molecular weight of the digested peak corresponded to the value expected for initiation at all possible groups on the protein. These results point to quasi-unitary efficiency of initiation. The polymer chains should all have comparable lengths (*n*) within a given conjugate.

Preparation of αCT–(linear PEG) Conjugates: Conjugates of αCT with linear PEG were prepared by reaction of αCT with monomethoxy polyethylene glycol (5 kDa; $mPEG_{5kDa}$) bearing an aldehyde (CHO) functional group. For reductive alkylation, αCT (2 mg, 0.08 μmol, 1 eq.) and $mPEG_{5kDa}$-CHO (50 mg, 0.01 mmol, 125 eq.) were dissolved in 1 mL 100 mM phosphate buffer (pH 6) containing 20 mM $NaCNBH_4$. The reaction was allowed to proceed for 16 h at 4 °C. After the conjugation reaction, the conjugate was purified by centrifugal dialysis (MWCO 30 kDa) and the number of conjugated polymer chains determined as for the αCT–pOEGMA conjugates.

^{1}H NMR Spectroscopy: ^{1}H NMR spectra were recorded in D_2O on a Bruker Av400 spectrometer (Bruker BioSpin, Fällanden, Switzerland) operating at 400 MHz for protons. Each spectrum consisted of 512 scans, with an acquisition time of 4 s per scan (conventional parameters for small-molecules).

Thermo-Sensitivity of αCT–pOEGMA Conjugates: Solutions of conjugates (5 mg mL^{-1} total) in phosphate buffered saline (pH 7.4) were prepared and the cloud-point measured using an Optimelt MPA100 system (Stanford Research Systems). The recorded turbidity curve was normalized between 0 and 1 and the transition temperature defined as that corresponding to a normalized absorbance of 0.5 (Supporting Information Table S10). A constant heating rate of 1 °C min^{-1} was used in all experiments. Equipment used was supported by Advantage West Midlands and part funded by the European Regional Development Fund.

Enzymatic Activity of αCT–Polymer Conjugates: The enzymatic activity of the conjugates was measured towards three substrates (Supporting Information Table S1–S9 and Figure S4). Benzoyl-L-tyrosine *p*-nitroanilide (BT*p*NA): to solutions of αCT or αCT–polymer conjugates (0.1 mg mL^{-1} protein) in 200 μL 100 mM Tris buffer (pH 8) in a 96-well plate was added 50 μL of a solution of BT*p*NA (1 mg mL^{-1}) in DMF at room temperature or 37 °C. The evolution of absorbance at 412 nm was recorded over 3 min and the activity calculated from the initial slope. *N*-succinyl-L-Ala-L-Ala-L-Pro-L-Phe-*p*-nitroanilide: to solutions of αCT or αCT–polymer conjugates (0.01 mg mL^{-1} protein) in 100 μL 100 mM Tris buffer (pH 8) in a 96-well plate was added 25 μL of a solution of substrate (1 mg mL^{-1}) in DMSO at room temperature or 37 °C. The evolution of absorbance at 412 nm was recorded over 1 min and the activity calculated from the initial slope. Milk casein: to solutions of αCT or αCT–polymer conjugates (0.1 mg mL^{-1} protein) in 100 μL 100 mM Tris buffer (pH 8) in Eppendorf vials was added 1 mL of a casein suspension (10 mg mL^{-1}) and the mixture incubated at room temperature or 37 °C. After 20 min, the reaction was stopped with 200 μL of 50% trichloroacetic acid in water. The precipitate was removed by centrifugation at 4 °C and the absorbance of 200 μL of supernatant at 280 nm measured.

Inhibition Assay with α_1-antiCT: To assess the sensitivity of αCT and αCT–polymer conjugates towards inhibition by α_1-antiCT, the enzymatic activity of αCT and αCT–polymer conjugates was measure as above, in the presence of 1–3 molar eq. α_1-antiCT (added sample solution prior to substrate). Results for peptide and casein substrate are found in Supporting Information Figure S6.

Statistics: The activity of αCT–polymer conjugates were compared by one-way ANOVA followed by a Tukey post-hoc test. Differences were considered significant at $p < 0.05$.

Acknowledgements

M.L. recognizes a doctoral scholarship from the Chinese Scholarship Council (CSC). M.I.G. recognizes funding from HEFCE. D.J.P. recognizes a scholarship from the University of Warwick. Expert technical assistance from the Functional Genomics Center Zurich and funding from the Sassella foundation are gratefully acknowledged.

Received: August 7, 2012
Revised: October 17, 2012
Published online: November 15, 2012

[1] a) T. M. Allen, P. R. Cullis, *Science* **2004**, *303*, 1818; b) S. Shaunak, A. Godwin, J. W. Choi, S. Balan, E. Pedone, D. Vijayarangam, S. Heidelberger, I. Teo, M. Zloh, S. Brocchini, *Nat. Chem. Biol.* **2006**, *2*, 312; c) Y. Yamamoto, Y. Tsutsumi, Y. Yoshioka, T. Nishibata, K. Kobayashi, T. Okamoto, Y. Mukai, T. Shimizu, S. Nakagawa, S. Nagata, T. Mayumi, *Nat. Biotechnol.* **2003**, *21*, 546; d) K. Fuhrmann, J. D. Schulz, M. A. Gauthier, J.-C. Leroux, *ACS Nano* **2012**, *6*, 1667; e) J. J. Moon, H. Suh, A. Bershteyn, M. T. Stephan, H. Liu, B. Huang, M. Sohail, S. Luo, S. Ho Um, H. Khant, J. T. Goodwin, J. Ramos, W. Chiu, D. J. Irvine, *Nat. Mater.* **2011**, *10*, 243; f) A. Hucknall, D. H. Kim, S. Rangarajan, R. T. Hill, W. M. Reichert, A. Chilkoti, *Adv. Mater.* **2009**, *21*, 1968; g) A. Hucknall, S. Rangarajan, A. Chilkoti, *Adv. Mater.* **2009**, *21*, 2441; h) H. Ma, J. Hyun, P. Stiller, A. Chilkoti, *Adv. Mater.* **2004**, *16*, 338; i) P. Akcora, H. Liu, S. K. Kumar, J. Moll, Y. Li, B. C. Benicewicz, L. S. Schadler, D. Acehan, A. Z. Panagiotopoulos, V. Pryamitsyn, V. Ganesan, J. Ilavsky, P. Thiyagarajan, R. H. Colby, J. F. Douglas, *Nat. Mater.* **2009**, *8*, 354; j) M. A. C. Stuart, W. T. S. Huck, J. Genzer, M. Muller, C. Ober, M. Stamm, G. B. Sukhorukov, I. Szleifer, V. V. Tsukruk, M. Urban, F. Winnik, S. Zauscher, I. Luzinov, S. Minko, *Nat. Mater.* **2010**, *9*, 101.

[2] a) G. Pasut, M. Sergi, F. M. Veronese, *Adv. Drug Delivery Rev.* **2008**, *60*, 69; b) G. Pasut, F. M. Veronese, *Adv. Drug Delivery Rev.* **2009**, *61*, 1177.

[3] C.-H. Pui, W. E. Evans, *N. Engl. J. Med.* **2006**, *354*, 166.

[4] J. D. Broome, *Nature* **1961**, *191*, 1114.

[5] L. Feuz, P. Strunz, T. Geue, M. Textor, O. Borisov, *Eur. Phys. J. E: Soft Matter Biol. Phys.* **2007**, *23*, 237.

[6] a) J.-F. Lutz, J. Andrieu, S. Üzgün, C. Rudolph, S. Agarwal, *Macromolecules* **2007**, *40*, 8540; b) J. F. Lutz, O. Akdemir, A. Hoth, *J. Am. Chem. Soc.* **2006**, *128*, 13046.

[7] a) W. Gao, W. Liu, J. A. Mackay, M. R. Zalutsky, E. J. Toone, A. Chilkoti, *Proc. Natl. Acad. Sci. USA* **2009**, *106*, 15231;

b) S. M. Ryan, X. Wang, G. Mantovani, C. T. Sayers, D. M. Haddleton, D. J. Brayden, *J. Controlled Release* **2009**, *135*, 51; c) J. P. Magnusson, S. Bersani, S. Salmaso, C. Alexander, P. Caliceti, *Bioconjugate Chem.* **2010**, *21*, 671; d) W. Gao, W. Liu, T. Christensen, M. R. Zalutsky, A. Chilkoti, *Proc. Natl. Acad. Sci. USA* **2010**, *107*, 16432; e) L. Tao, G. Mantovani, F. Lecolley, D. M. Haddleton, *J. Am. Chem. Soc.* **2004**, *126*, 13220; f) G. Mantovani, F. Lecolley, L. Tao, D. M. Haddleton, J. Clerx, J. J. L. M. Cornelissen, K. Velonia, *J. Am. Chem. Soc.* **2005**, *127*, 2966; g) M. A. Gauthier, M. Ayer, J. Kowal, F. R. Wurm, H.-A. Klok, *Polym. Chem.* **2011**, *2*, 1490.

[8] G. Cheng, Y. B. Melnichenko, G. D. Wignall, F. J. Hua, K. Hong, J. W. Mays, *Macromolecules* **2008**, *41*, 9831.

[9] a) B. S. Lele, H. Murata, K. Matyjaszewski, A. J. Russell, *Biomacromolecules* **2005**, *6*, 3380; b) S. Averick, A. Simakova, S. Park, D. Konkolewicz, A. J. D. Magenau, R. A. Mehl, K. Matyjaszewski, *ACS Macro Lett.* **2011**, *1*, 6.

[10] K. Matyjaszewski, N. V. Tsarevsky, *Nat. Chem.* **2009**, *1*, 276.

[11] L. A. Lokshina, V. N. Orekhovich, V. A. Sklyankina, *Nature* **1964**, *204*, 580.

[12] J. Spěváček, *Curr. Opin. Colloid Interface Sci.* **2009**, *14*, 184.

[13] D. Dukes, Y. Li, S. Lewis, B. Benicewicz, L. Schadler, S. K. Kumar, *Macromolecules* **2010**, *43*, 1564.

[14] A. Donev, F. H. Stillinger, P. M. Chaikin, S. Torquato, *Phys. Rev. Lett.* **2004**, *92*, 255506.

[15] M. A. Gauthier, H.-A. Klok, *Polym. Chem.* **2010**, *1*, 1352.

[16] S. S. Pai, B. Hammouda, K. Hong, D. C. Pozzo, T. M. Przybycien, R. D. Tilton, *Bioconjugate Chem.* **2011**, *22*, 2317.

[17] P. V. Kostetsky, *Biochemistry* **2007**, *72*, 392.

[18] F. Wurm, C. Dingels, H. Frey, H.-A. Klok, *Biomacromolecules* **2012**, *13*, 1161.

[19] B. S. Cooperman, E. Stavridi, E. Nickbarg, E. Rescorla, N. M. Schechter, H. Rubin, *J. Biol. Chem.* **1993**, *268*, 23616.

[20] Z. Ding, G. Chen, A. S. Hoffman, *J. Biomed. Mater. Res.* **1998**, *39*, 498.

[21] K. Bebis, M. W. Jones, D. M. Haddleton, M. I. Gibson, *Polym. Chem.* **2011**, *2*, 975.

[22] M. I. Gibson, D. Paripovic, H.-A. Klok, *Adv. Mater.* **2010**, *22*, 4721.

[23] A. Nelson, *Nat. Mater.* **2008**, *7*, 523.

[24] a) S. Brocchini, A. Godwin, S. Balan, J.-W. Choi, M. Zloh, S. Shaunak, *Adv. Drug Delivery Rev* **2008**, *60*, 3; b) M. W. Popp, S. K. Dougan, T. Y. Chuang, E. Spooner, H. L. Ploegh, *Proc. Natl. Acad. Sci. USA* **2011**, *108*, 3169.

International Journal of Pharmaceutics 391 (2010) 292–304

Contents lists available at ScienceDirect

International Journal of Pharmaceutics

journal homepage: www.elsevier.com/locate/ijpharm

Pharmaceutical Nanotechnology

Preparation of tri-block copolymer micelles loading novel organoselenium anticancer drug BBSKE and study of tissue distribution of copolymer micelles by imaging in vivo method

Mi Liu[a,b], Jianing Fu[a,b], Jing Li[a,b], Lihui Wang[a,b], Qiang Tan[a,b], Xiaoyuan Ren[a,b], Zuofu Peng[c], Huihui Zeng[a,b,*]

[a] State Key Laboratory of Natural and Biomimetic Drugs, Beijing 100191, China
[b] School of Pharmaceutical Science, Peking University, Beijing 100191, China
[c] Chilong Health Care International Limited Corporation, China

ARTICLE INFO

Article history:
Received 5 November 2009
Received in revised form 26 February 2010
Accepted 1 March 2010
Available online 6 March 2010

Keywords:
Polymeric micelles
Imaging in vivo
Anticancer
MCF-7
BBSKE

ABSTRACT

BBSKE (1,2-[bis(1,2-benzisoselenazolone-3(2H)-ketone)] ethane, PCT: CN02/00412) is a novel organoselenium anticancer drug that plays a role in anticancer through inhibiting TrxR (thioredoxin reductase). In this study, we prepared a tri-block copolymer micelles loading BBSKE utilizing the amphiphilic tri-block copolymers (PEG6000-PLA6000) which we synthesized. And then the characters of the copolymer micelles were investigated. When packaged in polymeric micelles, the water solubility of BBSKE was improved to 0.21 mg/ml. The IC_{50} were 7.14 μM, 5.05 μM and 4.23 μM when MCF-7 breast cancer cells were treated with BBSKE after 24 h, 48 h and 72 h. The inhibition effect of polymeric micelles to MCF-7 tumor cells was bettered when folate, whose receptor was highly expressed in various tumors, was coated on the surface of these nanoparticles. Finally, by adopting a new way of imaging in vivo, we studied the distribution of micelles in nude mice with and without MCF-7 tumor. The results demonstrated that this copolymer micelles loading BBSKE can accumulate into tumor efficiently.

1. Introduction

Thioredoxin reductase (TrxR) is a NADPH-dependent selenocysteine-containing flavoenzyme, it can catalyze the reduction of oxidized Trx (Holmgren, 1985). TrxR offers a target for the development of drugs to treat and prevent cancer (Gasdaska et al., 1995) due to its capability of stimulating cancer cell growth and inhibiting apoptosis. Recently, several clinical anti-tumor compounds have been reported to have anti-tumor activities through inactivating TrxR (Xiong et al., 1993; Harper et al., 1993; Deiry et al., 1993; Sabine and Katja, 2006).

Our lab has successfully synthesized a novel organoselenium compound 1,2-[bis(1,2-benzisoselenazolone-3(2H)-ketone)] ethane (BBSKE, Supplemental Fig. 1) targeting thioredoxin reductase, which has been shown to inhibit thioredoxin reductase activity in vitro (Shi et al., 2003; Zhao et al., 2006), and to repress the growth of a variety of human cancer cells from various organs, including lung, stomach, liver, cervix, prostate, blood, etc. (Deng et al., 2003; Shi et al., 2003; Yan et al., 2004; Zhao et al., 2006). As a new type of anticancer medicine, BBSKE is now in Phase I of the clinical trial. As far as we know, most of the anticancer drugs could not dissolve in water. BBSKE also has the characteristics of the anticancer drugs. In common solvents such as water, ethanol, chloroform, ethyl ether, ethyl acetate, etc., BBSKE is not easily dissolved, and only in dimethyl sulfoxide (DMSO) and N,N-dimethylformamide (DMF), it is dissolved easily. So we applied polymeric micelles to improve solubility of BBSKE. Li et al. have prepared polymeric micelles loading BBSKE with some bi-block copolymers such as MPEG5000-PLA2500, MPEG5000-PLA5000, MPEG5000-PLA10000, and investigated some characters of these polymeric micelles (Xinru et al., 2009). However, in our study, we prepared tri-block polymeric micelles loading BBSKE with another material PLA3000-PEG6000-PLA3000 that we synthesized. Besides, a targeting motif folate has been designed to coat the surface of the polymeric micelle by covalent connection, providing the nanoparticles with active targeting ability. Furthermore, we applied a novel method imaging in vivo to study the tissue distribution character of BBSKE polymeric micelles.

Current anticancer drug therapy results in systemic side effects due to non-specific uptake by normal healthy noncancerous tissues. Many anticancer drugs have marginal selectivity for malignant cells because they target the replicative apparatus in cells with high proliferation rates. Therefore, anticancer drugs having this mechanism

* Corresponding author at: State Key Laboratory of Natural and Biomimetic Drugs, Beijing 100191, China. Tel.: +86 010 82802878; fax: +86 010 82802878.
E-mail address: Zenghh@bjmu.edu.cn (H. Zeng).

0378-5173/$ – see front matter © 2010 Elsevier B.V. All rights reserved.
doi:10.1016/j.ijpharm.2010.03.001

of action also have high toxicity against rapidly dividing normal cells. The side effects associated with chemotherapy limit the dose or cumulative doses that can be administered to patients, which can lead to relapse of the tumor and which often leads to the development of drug resistance. To resolve the problem of difficult to dissolve, many attempts have been devoted to the development of new delivery systems such as emulsions, liposomes, copolymer micelles. Among these delivery systems, polymeric micelles formed by self-assembling of amphiphilic block copolymers seem to be a promising selective delivery system for many hydrophobic drugs. Recently, because of a number of advantages, polymer micelles have attracted increasing attention from both the scientific community and industry due to their promising applications in high-quality drug-delivery vehicles to treat cancers. Polymeric micelles have a core–shell structure with the drug in the core, thus the drug is effectively protected. It has a low level of toxicity in the human body, and a prolonged circulation time in the blood owing to its high water solubility (avoiding phagocytic and renal clearance). In addition, the passive accumulation of the micelles in a solid tumor is achieved by the enhanced permeability and retention (EPR) effect of the vascular endothelia at the tumor. It is also worth mentioning that a micelle as an invasive body is generally taken up by the cell through endocytosis, translated into endosomes, and then fused with lysosomes in which the proton concentration is 100 times higher (pH 4.0–5.0) than the physiological condition (pH7.4) (Kwon et al., 1994). Polymeric micelles have been applied in delivering many anticancer drugs such as cisplatin (Valery et al., 1999; Uchino et al., 2005), paclitaxel (Sung et al., 2001; Hamaguchi et al., 2007), doxorubicin, etc. (Hyuk and Tae, 2004).

In order to further improve the therapeutic indices of copolymer micelles loading anticancer drugs, the strategy of ligand-mediated has been applied. In this strategy, some ligands, whose receptors expressed selectively or overexpressed on tumor cells, are connected to the surface of the copolymer micelles. Folic acid (folate) is an attractive candidate molecule for targeting cancer cells because it is an essential vitamin for the biosynthesis of nucleotide bases and is consumed in elevated quantities by proliferating cells. The receptor for folic acid is overexpressed in many human cancers, including malignancies of the ovary, brain, kidney, breast, myeloid cells, and lung (Cummings and McArdle, 1986; Weitman et al., 1992; Goren et al., 2000). Folate has been popularly employed as a targeting moiety of various anticancer agents to avoid their non-specific attacks on normal tissues as well as to increase their cellular uptake within target cells (Wang et al., 1995; Lu et al., 1999; Reddy and Low, 2000; Lu and Low, 2002; Hyuk and Tae, 2004; Guangya et al., 2008).

In this study, a kind of tri-block copolymer of polyethylene glycol-polylactic acid (PEG-PLA) was synthesized for the purpose of improving the targeting and increasing the water solubility. With the tri-block copolymers as the carrier materials, we prepared a tri-block copolymer micelle packaged BBSKE in the core. In order to further enhance the targeting of polymer micelles, folic acid was connected to the hydrophilic side of the copolymer. Thus, we obtained a targeting function nanoparticle, which enhanced the targeting of drugs and reduced the toxicity of drugs. The polymeric micelles loading anticancer drug were investigated from different aspects, such as particle size, shape, and the inhibition of tumor cell growth, etc. And then, we focused on the study of distribution of the polymeric micelles in the tissues after they were injected into the nude mice. In the study of the tissue distribution of the copolymer micelles in nude mice, we applied a new technology — imaging in vivo. There are many media in which in vivo imaging could be used, such as fluorescence, NMR, infrared, etc. (Frank et al., 2002). In our experiment, we applied the Maestro in vivo imaging device (The company's Cambridge Research Instruments) to detect fluorescence signals (Maha et al., 2008; Erina et al., 2009; Muraru et al., 2009; Tomoyuki et al., 2009).

2. Material and methods

2.1. Materials

BBSKE (purity > 98.5%) was synthesized by us (School of Pharmaceutical Science, Peking University, Beijing, China). Polyethylene glycol 6000 (PEG6000) and Polyethylene glycol 4000 (PEG4000) were purchased from Merck. D,L-Lactide (CAS. R.NO: 95-96-5), and p-nitrophenylchloroformate (PNP) were all obtained from SIGMA. Adriamycin (doxorubicin, DOX) was purchased from Beijing Hua Feng Technology Co., Ltd. The model of scanning electron microscope was HITACHI, S-4800.

Female nude mice were obtained from Experimental Animal Center of Peking University acclimatized for several days after arrival. All animals were provided with standard food, water and were exposed to alternating 12 h periods of light and darkness. Temperature and relative humidity were maintained at 25 °C and 50%, respectively. All care and handling of animals were performed with the approval of Institutional Authority for Laboratory Animal Care of Peking University.

2.2. Synthesis of tri-block copolymer PEG6000-PLA6000

The lactide was first recrystallized with ethyl acetate three times. It was then dried in vacuum at room temperature to the melting point 127 °C. Then PEG6000 (2 g) and toluene (100 ml) was added into the flask. Water separation device is used next to remove the water in toluene. The lactide (2 g) and stannous octoate (0.5% quality of lactide), which were used as a catalyst, were added to the flask. Thereafter, the polymerization reaction then undergoes for 24 h under the conditions of oil bath at 120 °C and nitrogen protection. The crude product, after the toluene was evaporated, was dissolved with chloroform. The chloroform solution was dropped into the ether at 0 °C. Then we obtained a kind of solid powder by filtering the ether solution. The powder was dried under vacuum at room temperature, and then it was placed in −20 °C refrigerator for storage (Scheme 1).

2.3. Synthesis of folic acid-polyethylene glycol-polylactic acid

2.3.1. Synthesis of single-amino-polyethylene glycol

First, PEG4000 (2 g, 0.5 mmol), methyl benzenesulfonyl chloride (0.09525 g, 5 mmol) and pyridine (5 ml) solution were dissolved in CH_2Cl_2 (10 ml). After a 24 h reaction was conducted at room temperature, 3 mol/L HCl (47 ml) was added into the solution. Then $NaHCO_3$ (0.5 g) was added into the organic layer following violent agitation. Crude PEG-p-toluene sulfonic acid ester was obtained after the filtrate was Rotary evaporated. The precipitate was obtained by dropping the tetrahydrofuran (0.87 ml) dissolved crude products to ether (43.5 ml). Subsequently through filtering and vacuum drying, the pure product was acquired. Then the pure product (1.61 g) was reacted with of 25% ammonia (16 ml) for 6 h at 140 °C in high-pressure reactor and 1 mol/L NaOH (14 ml) is added to the organic layer (approximately 14 ml, containing PEG-p-toluene sulfonic acid ammonium salt) attained by dichloromethane (16 ml) extraction, then the solution is stirred for 2 h. The product amino-polyethylene glycol separation was obtained, after some operations of separating organic layer, washing to neutral and drying. The Ninhydrin test was used to verify whether the amino-polyethylene glycol was obtained.

2.3.2. Synthesis of tertiary-butyloxycarbonyl amino-polyethylene glycol

Single-amino-polyethylene glycol (6 g, 0.01 mol) and $(Boc)_2O$ (0.22 g, 0.001 mol) were reacted in methanol at 50 °C for 10 h. Thereafter, the product of rotation evaporation was dissolved in

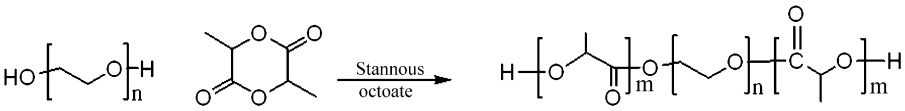

Scheme 1. Synthesis of PEG6000-PLA6000 (PEG: polyethylene glycol; PLA: polylactic acid).

CH_3Cl completely. A white powder could be obtained by adding the dissolution into cold ether. Finally, the solid precipitate was vacuum dried for 12 h.

2.3.3. Synthesis of Boc-PEG4000-PLA4000

Before the experiment lactide was recrystallized with ethyl acetate three times, and then it was vacuum dried for 24 h. Initially, Boc-PEG4000 (2 g) was placed in the flask, and then toluene (100 ml) was added. Water separation device was used next to remove the water in toluene. As described before, the lactide (2 g) and stannous octoate (0.5% quality of lactide) which were used as a catalyst were added to the flask. After that, the polymerization reaction was conducted for 24 h under the conditions of oil bath at 120 °C and nitrogen protection. The crude product, after the toluene was evaporated, was dissolved with chloroform. The chloroform solution was dropped into the ether at 0 °C. Then after the ether solution was filtered and the Boc-PEG4000-PLA4000 was obtained.

2.3.4. Synthesis of NH_2-PEG-PLA

Boc-PEG4000-PLA4000 and trifluoroacetic acid reacted for 3 h under the conditions of nitrogen protection. As mentioned earlier, the product of rotation evaporation was dissolved in CH_3Cl completely. We can get a white powder by adding the dissolution into cold ether. Thereafter, Ninhydrin reaction was used to test for the presence of the amino group. The results where the product becomes purple indicate the existence of free primary amino groups.

2.3.5. Synthesis of folate-NH-PEG-PLA

First, folic acid, N-hydroxy succinimide (NHS), and N,N-dicyclohexyl carbodiimide (DCC) (by the molar ratio of 1:1.5:1.5) reacted 6 h in DMSO, at room temperature. Then DCU was removed by filtering. And then The NH_2-PEG-PLA and 1.2 equivalent of DCC were added to the system, thereafter the system underwent the nitrogen protection for 12 h. When the reaction was completed, the solution was put for dialysis for 24 in the dialysis bag (3500). The dialysis solution was dried on the freeze-drying machine. When the dialysis was completed, a certain amount of folic acid-NH-PEG-PLA and pure folic acid were dissolved in DMSO, following UV scanning. The scanning results showed that the UV maps were exactly the same and thus confirmed that the folic acid was connected to the NH_2-PEG-PLA by chemical bond (Lee and Low, 1995; Guo et al., 2000; Hyuk and Tae, 2004; Guangya et al., 2008) (Scheme 2).

2.4. Synthesis of PEG-PLA-DOX

The reagent PNP, PLA-PEG-PLA and pyridine (PLA-PEG-PLA/PNP/pyridines molar ratio = 1/5/10) were reacted in anhydrous dichloromethane at 0 °C for 30 min under the conditions of nitrogen. The reaction was conducted for 4 h at room temperature under the conditions of nitrogen. After the reaction was completed, as depicted before, the product of rotation evaporation was dissolved in CH_3Cl completely. We can get a white powder by adding the dissolution into cold ether. The product of PNP-PLA-PEG-PLA-PNP was acquired. In our study, we adopted the method performed by Galdwell to test for the degree of substitution of the PNP. Next, the previous product PNP-PLA-PEG-PLA-PNP, DOX-HCL and Triethylamine (TEA) (PNP-PLA-PEG-PLA-PNP/DOX-HCL/TEA molar ratio = 1:2:8) dissolved in DMF and took a reaction for 24 h under the protection of nitrogen. After the reaction was accomplished, the solution was diluted five times with distilled water dialysis for 24 h in the dialysis bag (3500). Dialysis solution was dried on the freeze dryer. Then the freeze-dried powder was placed in a −20 °C refrigerator for storage (Kataoka et al., 2000; Yoo and Park, 2001; Hyuk and Tae, 2004) (Scheme 3).

2.5. Preparation of nano-micelle

We adopt the way of dialysis to the prepare the polymer micelles containing the drug.

2.5.1. Preparation of drug-loaded polymer micelles

PEG6000-PLA 6000 (100 mg), folate-NH-PEG-PLA (12 mg) and BBSKE (10 mg) were dissolved in 50 ml DMSO and was put into dialysis bag (3500) for dialysis for 24 h in 3 L of distilled water. Upon completion of dialysis, the dialysis solution then underwent centrifuge at 3000 rpm for 30 min, and then it was filtered using 0.45 μm microporous membrane. The filtrate with PEG4000 as a protective agent was freeze-dried in the freeze-drying freeze dryer.

2.5.2. Preparation of polymeric micelles with fluorescent reagents

PEG6000-PLA6000-DOX (100 mg), folic acid-NH-PEG-PLA (12 mg) and BBSKE (10 mg) was dissolved in 50 ml DMSO and was put into a dialysis bag (3500) for dialysis for 24 h in 3 L of distilled water. Upon completion of dialysis, dialysis solution then underwent centrifuge at 3000 rpm for 30 min, and was filtered using 0.45 μm microporous membrane. The filtrate with PEG4000 as a protective agent was freeze-dried in the freeze-drying freeze dryer.

2.6. Analysis of critical micelle concentration (CMC)

In order to determine the critical micelle concentration of tri-block copolymers in distilled water, fluorescence measurements were carried out using pyrene (Sigma–Aldrich, Inc.) as probe (Kwon et al., 1993; Hagan et al., 1996; Yoo and Park, 2001; Jaeyoung et al., 2004; Xinru et al., 2009). Pyrene predissolved in acetone was added to the test tube, and the solvent was evaporated. Different amounts of nanoparticles solution and distilled water were added to this tube and different concentrations of tri-block copolymers ranging from 10^{-7} mg/ml to 10^{-1} mg/ml were made. The concentration of pyrene used was 6.0×10^{-7} mol/L. The solution was incubated at 37 ± 0.5 °C with mild stirring to ensure that the pyrene equilibrated between the nanoparticles and the aqueous phase completely. Fluorescence spectra of pyrene were recorded with a PC fluorescence spectrometer (Shimadzu RF-5301). The excitation wavelength used was 333 nm and 335 nm, and the emission spectra were recorded at 390 nm. The peak height intensity ratio (I_{335}/I_{333}) of the peak of 335 nm to the peak of 333 nm was plotted against the logarithm of polymer concentration. Two tangents were then drawn, one to the curve at high concentrations and another through the points at low concentrations. The CMC value was taken from the intersection between the two tangents.

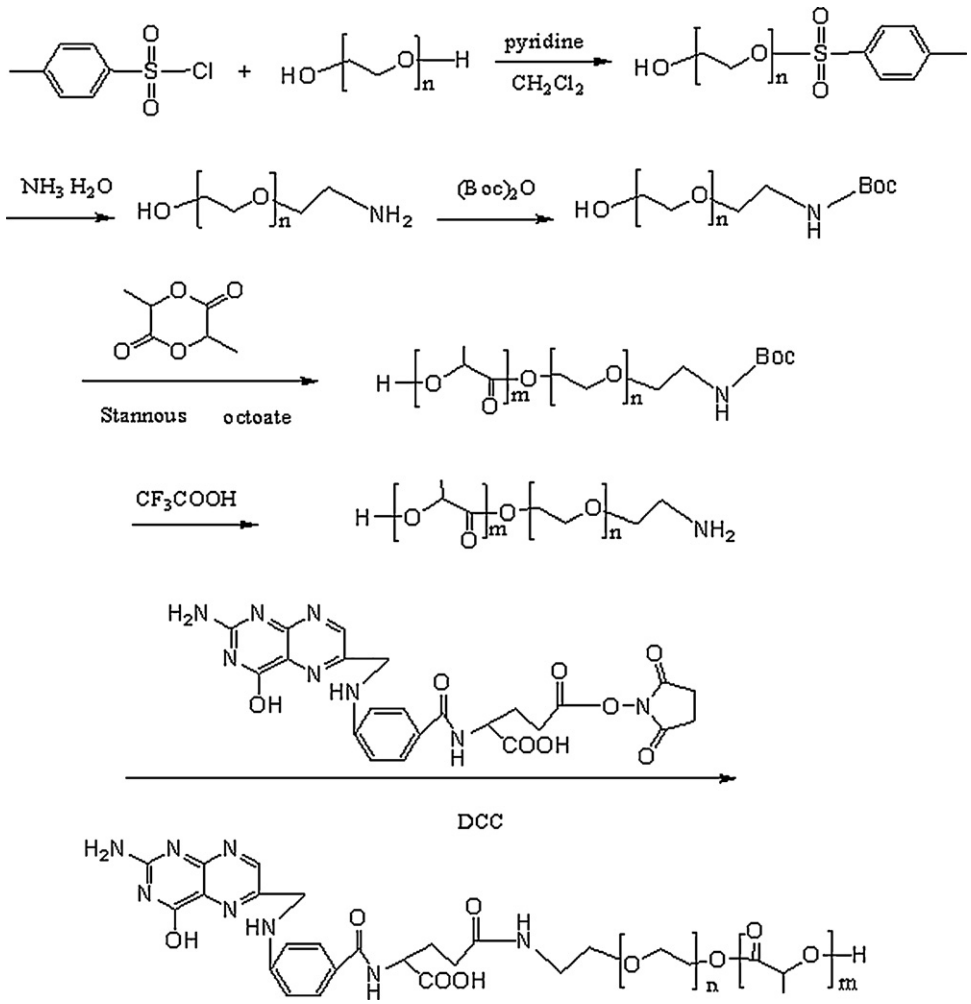

Scheme 2. Synthesis of folate-PEG4000-PLA4000.

2.7. Drug content and solubility analysis

The method of liquid chromatography was applied to detect the content of the drug BBSKE loaded in polymeric micelles. First, we obtained the standard curve of BBSKE by HPLC. In drug content investigation, 2 mg lyophilized polymeric micelles loaded BBSKE were dissolved in 1 ml DMSO, then the solution was filtered by 0.45 μm pore-sized filtration membrane and the concentration of BBSKE in the solution was measured by HPLC (Agilent 1100, Agilent Technologies, Inc., USA). For solubility analysis, we put excessive BBSKE polymeric micelles lyophilized powder into 2 ml distilled water. Over a period of time, the solution was filtered through a 0.45 μm filter to remove aggregates. After that 2 ml DMSO was added to the solution and the content of BBSKE in the solution was detected by HPLC (Agilent 1100, Agilent Technologies, Inc., USA). The tri-block copolymer PEG6000-PLA6000 under the wavelength of 320 nm showed no UV absorption. The HPLC column was produced by Agilent Technologies, Inc., USA. The HPLC conditions are as follows: mobile phase – methanol:water (0.01%Phosphate) = 40:60; detection wavelength: 320 nm; temperature: 25 °C.

2.8. Particle size and morphology analysis

The size of the polymer micelles was determined using dynamic light scattering analysis. The machine utilized is Malvern Zetasizer Nano ZS particle size determination instrument. Wavelength of the laser beam equipment was set to 633 nm, the angle between the incident and scattered light was 90°. Before the examination, each sample was filtered by the utilization of the 0.45 μm membrane filter. Each sample was tested three times, we adopt the average of three times as the size of the sample.

First of all, drug-loaded micelles were plated, and then, we observed the micelles in the scanning electron microscopy. The model of scanning electron microscope is HITACHI, S-4800.

Precision micro-pipette was applied to check the volume of 2 ml of distilled water, the water was then added to the excessive drug polymer micelles. The solution underwent Ultrasonic for 5 min in order to make polymeric micelles dissolved fully in the water. 8 ml DMSO then was added to the system, following ultrasonic mixing. We measured the content of the drug through the liquid chromatography method.

2.9. In vitro test of BBSKE release from polymeric micelles

The BBSKE release from polymeric micelles in vitro was measured by a dialysis method. The dialysis was conducted in PBS media (pH 7.4) containing 50% fetal bovine serum (FBS) (Ishida et al., 2001; Jaeyoung et al., 2004; Xiong et al., 2005; Michael et al., 2006; Chen et al., 2009; Xue et al., 2010). The lyophilized polymeric micelles loaded BBSKE was dissolved in 10 ml release media, and then the media were placed into a dialysis bag (MW cutoff 3500) sealed at both ends with clips. The concentration of BBSKE was 150 μg/ml. The dialysis bag was then placed into a beaker containing 190 ml

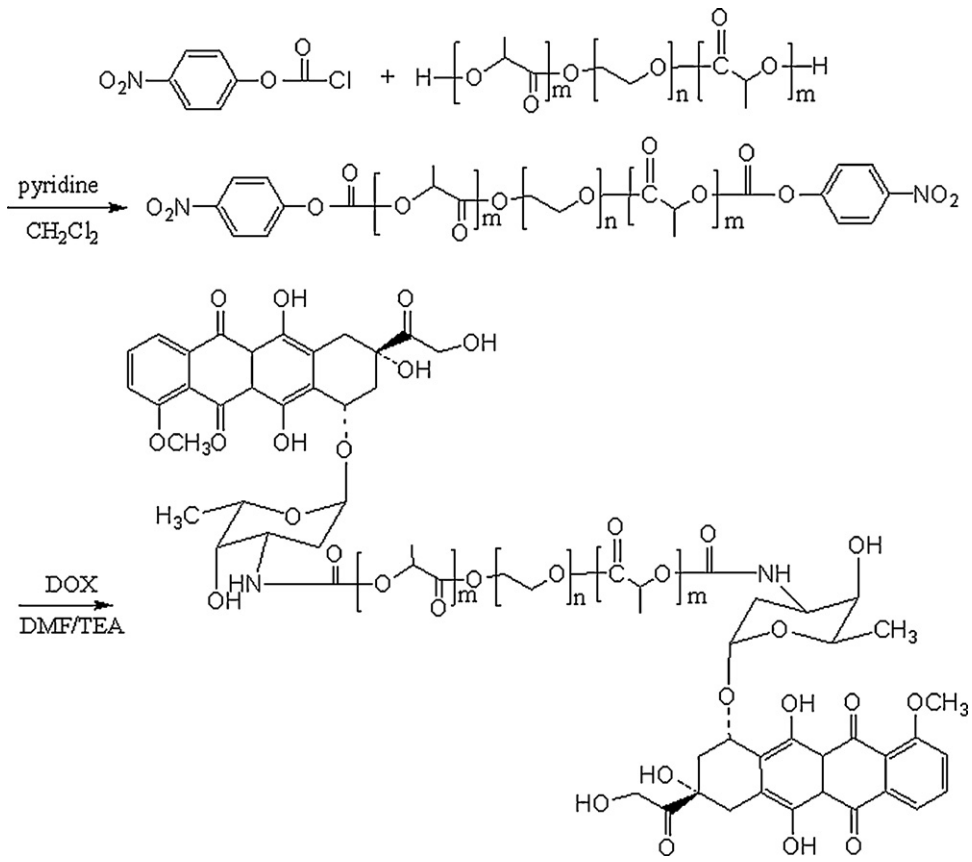

Scheme 3. Synthesis of DOX-PLA3000-PEG6000-PLA3000-DOX.

of the media, and incubated with stirring for 24 h at 37 ± 0.5 °C. At various time points, 3 ml samples were withdrawn from the beaker and replaced with equal volume of the media. The concentrations of BBSKE in various samples were measured by HPLC (Agilent 1100, Agilent Technologies, Inc., USA). Liquid conditions are as follows: mobile phase – methanol:water (0.01%Phosphate) = 40:60; detection wavelength: 320 nm; temperature: 25 °C.

2.10. Cell growth inhibition assay

Stock solutions of BBSKE were made at 20 μM concentration in DMSO and freshly diluted in culture medium for all cell experiments. Stock solutions of drug-loaded polymer micelles without folic acid, drug-loaded polymer micelles with folic acid were dissolved in DMEM directly at concentration of 1 mM. and freshly diluted in culture medium for all cell experiments.

The effect of BBSKE and drug-loaded polymer micelles on growth of MCF-7 were determined using the procedure of MTT cell proliferation assay which was the first time for this novel drug to be used to inhibit these breast cancer cells. Cells were maintained as mono-layer cultures in DMEM with 10% FBS and antibiotics (100 U of penicillin/ml and 100 mg streptomycin/ml). The cells were inoculated in 5% CO_2 atmosphere. Exponentially growing cells were detached from the cell culture and a single cell suspension was produced. Then the cells were plated into 96-well plates with 5000 cells a well, treated with naked BBSKE, drug-loaded polymer micelles without folic acid, drug-loaded polymer micelles with folic acid, drug-loaded polymer micelles with folic acid containing free folic acid as a antagonist of desired concentration when cells began to grow exponentially. Free folic acid in drug-loaded polymer micelles with folic acid containing free folic acid was added before the polymer micelles were added. After incubation for 24 h, 48 h, or 72 h, 20 μl of 3-(4,5-diethyl-2-thiazolyl)-2,5-diphenyl tetrazolium bromide (MTT 5 mg/ml) was added to each well, and the cells were further incubated at 37 °C for 4 h. The medium was then removed and 200 μl of HCl 0.04 M in isopropanol was added to dissolve the reduced formazan product. The plate was then read on a microplate reader (Bio-RAD, model 550) at 590 nm.

2.11. Confocal assay

BBSKE can reach a certain fluorescence signal, but the signal was not strong enough. As a result in Confocal trials, we connected doxorubicin to the polymer material of PEG6000-PLA6000 with covalent bond, which helped us to achieve DOX-PLA-PEG-PLA-DOX. And then, we utilized DOX-PLA-PEG-PLA-DOX as the polymer material to prepare polymer micelles, the doxorubicin (excitation wavelength 480 nm, detection wavelength 560 nm) was exploited as a fluorescent probe for detection. MCF-7 cells were inoculated into the Petri dish, and the percentage of cell aggregation was at least 50% before drug treatment. Subsequently, folic acid (100 μM of 100 μl) was added into the group of drug-loaded polymer micelles with folic acid containing free folic acid as a antagonist (free folic acid and folic acid of the micelle surface has molar ratio of 100:1). Each group was placed in the 37 °C incubator for 30 min, the groups were then placed in the 37 °C incubator for 3 h after drug-loaded polymer micelles was administrated. After these operations were performed, each group with polymer micelle added was rinsed with cold PBS three times and fixed 10 min with 4% paraformaldehyde. Next, we used hoechst33342 (excitation wavelength 350–363 nm, detection wavelength 450 nm) staining the nucleus for 5 min. Consequently, image analysis was conducted by Confocal laser

scanning microscope (LETCA TCS SP2) with 480 nm as excitation wavelength.

2.12. Flow cytometry assay

Adherent MCF-7 cells were digested with 0.25% trypsin, and then were harvested and resuspended into the single-cell suspension with fresh DMEM culture medium (without serum). In the group of polymer micelles with folic acid, the cells were pre-incubated for 30 min with free folic acid as an antagonist. Each group was incubated at 37 °C for 30 min. Subsequently, polymer micelles with fluorescence probe were added and incubated further for 3 h in 37 °C water bath. They were then rinsed three times with cold PBS. Finally the cell suspensions were transferred to the flow analysis tube and were detected by flow cytometer. A flow cytometric analysis was then carried out using CS Express V3 software (Beckman Coulter, Inc., Fullerton, CA, USA).

2.13. Study of tissue distribution by imaging in vivo method

As described before, the fluorescence signal of BBSKE was not strong enough, doxorubicin was connected to the tri-block copolymer materials PEG6000-PLA6000 with covalent bond and we obtained DOX-PLA-PEG-PLA-DOX. Then, we utilized DOX-PLA-PEG-PLA-DOX as the polymer material to prepare polymer micelles, thus we can exploit doxorubicin as a fluorescent probe for detection.

The tumor in armpit of nude mice was achieved through the way of embedding tumor blocks. The nude mice were fasted 12 h before the experiment. Before injection, the nano-micelles labeled with fluorescent were dissolved in 0.9% normal saline, and the nude mice were anesthetized by urethane. And then, the same amount of copolymer micelles were injected into the nude mice with tumor and nude mice without tumor through the access of tail vein injection. After 3 h and 24 h, the in vivo imaging device (Maestro, Cambridge Research Instruments) was used to observe the tissue distribution of the polymer micelles in the body. Subsequently, each vital organ was taken out to be detected on the in vivo imaging device for further observation.

The device of in vivo imaging belongs to Maestro (Cambridge Research Instruments). Parameters set are as follows: green light is applied as excitation; detection wavelength range from 550 nm to 700 nm; temperature was room temperature; light is set to 1 and station is set to 1B (Maha et al., 2008; Erina et al., 2009; Tomoyuki et al., 2009).

2.14. Statistical analysis

Results were analyzed using a two-tailed Student's *t*-test to assess statistical significance. Values of $P < 0.05$ were considered statistically significant.

3. Results and discussion

3.1. Synthesis of block copolymer

We synthesized tri-block copolymer PEG6000-PLA6000, bi-block copolymer folate-PEG4000-PLA4000 and tri-block copolymer DOX-PLA3000-PEG6000-PLA3000-DOX. The methods of ^{1}H NMR and UV–vis were carried out to confirm the ratio of hydrophobic and hydrophilic chain in PEG6000-PLA6000 and folate, DOX were connected to NH_2-PEH-PLA.

The ^{1}H nuclear magnetic resonance (^{1}H NMR, $CDCl_3$, trimethylsilyl (TMS)) results of PEG6000-PLA6000 are shown in Fig. 1. From Fig. 1, we can witness the main peaks as follows: δ0.000 (TMS); δ1.554 (–CH_3, PLA); δ3.625 (–CH_2–, PEG); δ5.167 (–CH–, PLA); δ7.260 ($CDCl_3$). The ideal ratio of PEG6000-PLA6000 is 3:8:1 (δ1.567:δ3.617:δ5.167). ^{1}H NMR experiment indicated that the ratio of hydrophobic and hydrophilic chain segments in PEG6000-PLA6000 was 1:1. The analysis of DOX-PLA3000-PEG6000-PLA3000-DOX and folate-PEG4000-PLA4000 through the ^{1}H NMR also shows the same results as PEG6000-PLA6000.

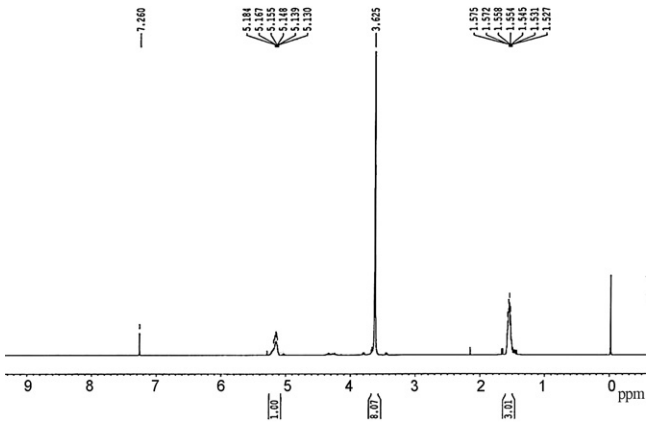

Fig. 1. ^{1}H NMR (H) for PEG-PLA.

Fig. 2B illustrated the UV–vis scanning result of PEG-PLA in the 200–600 nm patterns, which demonstrated that in this range the copolymer PEG-PLA had no UV–vis absorption. Fig. 2C and E shows the UV–vis absorption situation of DOX and folic acid in DMSO in the same pattern as PEG-PLA. The UV–vis scanning result of DOX showed that DOX had two main absorption peaks between 200 nm and 600 nm, one was at about 270 nm, another was at about 480 nm. Fig. 2E showed that folic acid has one main peak at about 290 nm. While, Fig. 2D and picture Fig. 2F, respectively, shows the UV–vis experiment results of DOX and folate in DMSO after they were connected to PEG-PLA. From Fig. 2D and F we could observe almost same results as those from Fig. 2C and E. Considering that PEG-PLA had no absorption in this range and before the measurement samples of PEG-PLA-DOX and folate-PEG-PLA were fully dialysed, to ensure the free DOX and folic acid, whose molecular weight were less than 3500, had been completely removed. According to all the evidence above we could safely draw a conclusion that DOX and folic acid had been connected to the PEG-PLA (Hyuk and Tae, 2004; Jae et al., 2004; Sabine and Katja, 2006; Zhigang et al., 2007).

3.2. Characters of drug-loaded polymeric micelles

Amphipathic tri-block copolymers self-assembled into polymeric micelles in an aqueous solution. The size of polymeric micelles is approximately less than 100 nm, which not only makes them ideal drug-delivery carriers for escaping from renal exclusion and the reticulo-endothelial system, but gives them an enhanced vascular permeability. Copolymeric micelles are composed of a hydrophilic outer shell exposed to the aqueous phase and a hydrophobic inner core encapsulating drug molecules. Fig. 3 depicts the structure of four different tri-block polymeric micelles employed in our study. Fig. 3A shows the structure of tri-block polymeric micelles loading BBSKE. The structure of copolymer micelles loading BBSKE, connected with DOX in the hydrophobic chain is displayed in Fig. 3C. While Fig. 3B and D are, respectively, the polymeric micelles, depicted in Fig. 3A and C, coated with folate. As shown in Fig. 3, the copolymer micelles usually are spherical, which have a hydrophobic core and a hydrophilic shell. BBSKE is packaged into the sphere through the hydrophobic interaction. It can be seen that the folate-PEG4000-PLA4000 is longer than folded PEG6000-PLA6000. This is because folate connected with a larger chain may

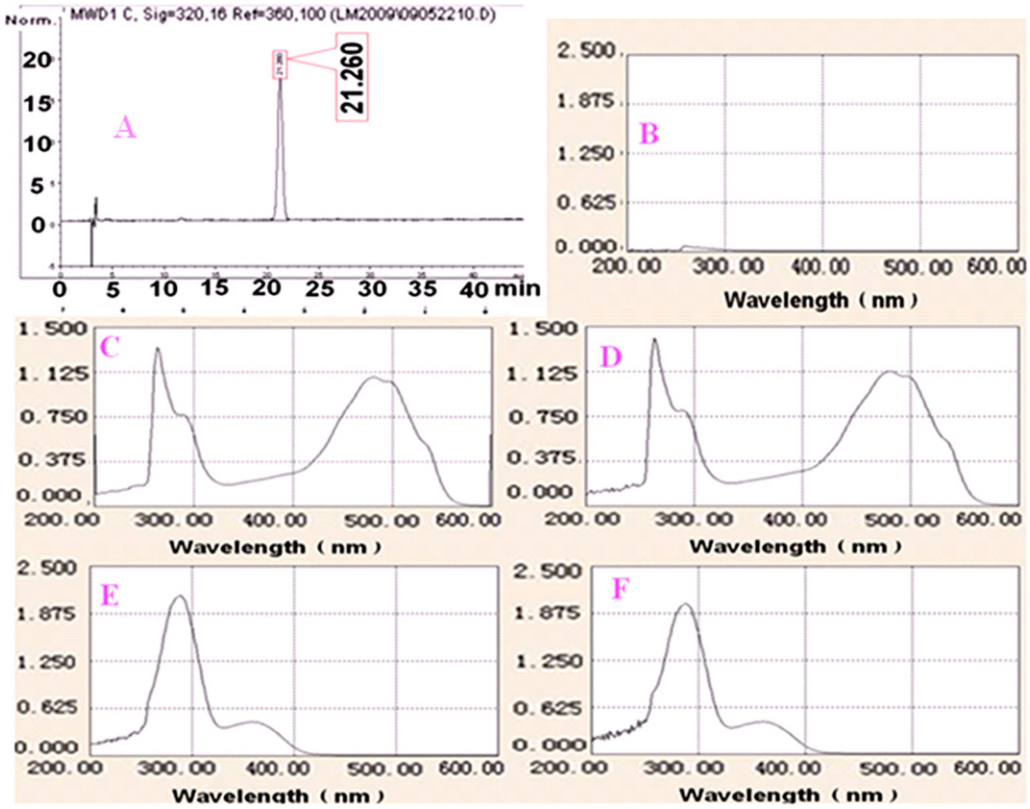

Fig. 2. Retention time of BBSKE in HPLC and UV–vis for folate and DOX.

be easier to expose to the environment and thus they can search the folate receptor and perform a targeting function more effectively.

3.2.1. Analysis of critical micelle concentration

The CMC values of tri-block copolymers were determined by a fluorescence spectroscopy measurement. Pyrene was chosen as a fluorescent probe because its photochemical properties are suitable for an effective probe (Kwon et al., 1993; Hagan et al., 1996; Yoo and Park, 2001; Jaeyoung et al., 2004; Xinru et al., 2009). The CMC values of tri-block copolymers PLA3000-PEG6000-PLA3000 was 1.74×10^{-7} mol/L and the CMC values of DOX-PLA3000-PEG6000-PLA3000-DOX was 3.89×10^{-7} mol/L. The CMC values

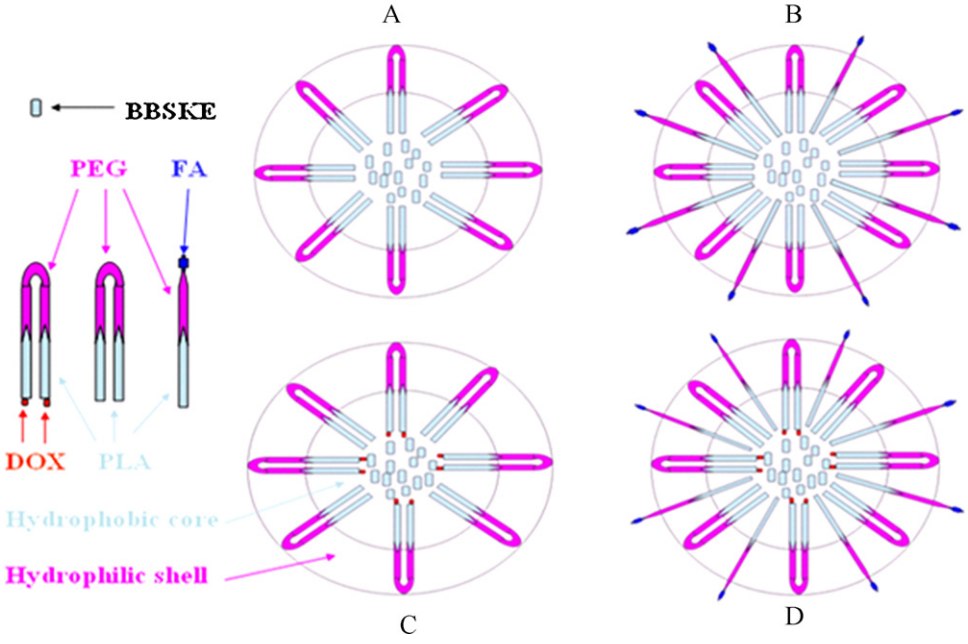

Fig. 3. The structure of copolymer micelles. (A) Structure of PEG-PLA/BBSKE copolymer micelles; (B) structure of folate-PEG-PLA/BBSKE copolymer micelles; (C) structure of PEG-PLA-DOX/BBSKE copolymer micelles; and (D) structure of folate-PEG-PLA-DOX/BBSKE copolymer micelles. PEG: polyethylene glycol; PLA: polylactic acid; DOX: doxorubicin; and BBSKE: ethaselen.

Table 1
Results of particle size determination. The value was mean ± SD ($n \geq 3$).

Particles	Size (nm)
Blank polymer micelle	31.03 ± 1.90
BBSKE polymer micelle	71.25 ± 2.75
FA-BBSKE polymer micelle	75.68 ± 2.34
DOX-BBSKE polymer micelle	83.28 ± 5.44
FA-DOX-BBSKE polymer micelle	85.43 ± 3.86

PEG: polyethylene glycol; PLA: polylactic acid; DOX: doxorubicin; BBSKE: ethaselen; and FA: folate.

of the tri-block copolymers that we synthesized was pretty low, which is an advantage of polymeric micelles as drug carriers. The CMC values of these tri-block copolymers were slightly increased when DOX was connected to the hydrophobic block. This may be attributed to the increase in the hydrophilicity of hydrophobic block with the connection of DOX. Because the absolute value of CMC is very low, however, the stability of nanoparticles was not affected by the connection of DOX.

3.2.2. Drug content and solubility analysis

The data in our experiments suggested that when BBSKE was packaged in the polymer micelle, the water solubility of BBSKE reached to 0.21 mg/ml ($n \geq 3$). Compared with the original situation where BBSKE was insoluble in water (2.57 μg/ml) (Xinru et al., 2009), polymer micelles significantly improved the water solubility of BBSKE, which enabled us to choose the method of injection as the route of administration. This will help BBSKE to perform better in its anti-tumor effect.

We prepared drug-loaded polymer micelle by the dialysis method and determined the drug content with liquid chromatography. In our condition the retention time of BBSKE was 21 min as shown in Fig. 2A. The drug-loaded content of tri-block copolymer micelles in the absence of folic acid was 4.91% ($n \geq 3$) and the drug-loaded content of copolymer micelles coated with folic acid was 4.73% ($n \geq 3$) (Weiyang et al., 2007; Xinru et al., 2009).

3.2.3. Size of nanoparticles and morphology analysis

Dynamic light scattering analysis was applied to measure the size of various polymeric micelles. Table 1 was the result of analysis of particle size for five different nanoparticles. From Table 1 we could observe that size of blank micelles was approximately 30 nm. However the size of particles was increased significantly to approximately 70 nm when it came to the polymeric micelles loading BBSKE. The size of drug-loaded micelles was bigger than that of drug-free micelles, which suggested that BBSKE molecules were trapped in the hydrophobic inner cores and that these entrapped BBSKE molecules increased the average size of BBSKE-loaded tri-block copolymer micelles. Meanwhile, the size of polymer micelles with folic acid as a target was slightly larger than that of non-folate micelles. This maybe due to folate-PEG4000-PLA4000 being longer than folded PEG6000-PLA6000. Another increase in size was observed when DOX was connected to the materials as fluorescence signal for detection.

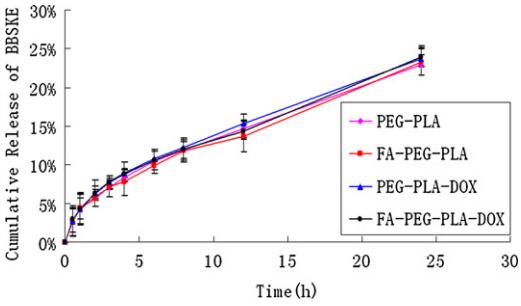

Fig. 5. In vitro release profiles of BBSKE from polymeric micelles (mean ± SD, $n = 3$).

Scanning electron microscope (SEM) was used to study morphology character of polymeric micelles. The SEM experimental results are vividly shown in Fig. 4. Fig. 4I gives the view of blank polymeric micelles investigated through SEM. Fig. 4II shows the shape of polymer micelles loaded BBSKE. Fig. 4III shows the result we obtained by observing polymer micelles loaded BBSKE and coated with folic acid using SEM. From the SEM experimental results, we can readily elicit a conclusion that the blank micelles, micelles loading drugs and micelles loading drugs and coated with folic acid are all spherical in shape and their particle sizes are less than 100 nm. Meanwhile, the results of their particle sizes shown in Fig. 4 are in accord with the data shown in Table 1.

3.2.4. In vitro release profiles of BBSKE from polymeric micelles

The results of in vitro BBSKE release experiments are presented in Fig. 5. During 24 h, the contents that BBSKE released from four kinds of polymeric micelles were all about 23%, in the media PBS (pH 7.4) with 50% fetal bovine serum. As shown in Fig. 5, the modification of targeting molecular folate has no affect on the release activities of BBSKE from polymeric micelles. Besides, the release of BBSKE from polymeric micelles modified with DOX was also very similar to the release of BBSKE from polymeric micelles without the modification, which means release activities of BBSKE from polymeric micelles were not affected by the connection of DOX.

3.3. MCF-7 cell growth inhibition study

In our study, we applied the novel anti-tumor medicine BBSKE and BBSKE packaged in tri-block copolymer micelles to inhibit the growth of MCF-7 breast cancer cells and MTT assay to analyze the treated cancer cells. Why did we choose MCF-7 cells as the candidate for our study? This was because the folate receptor was highly

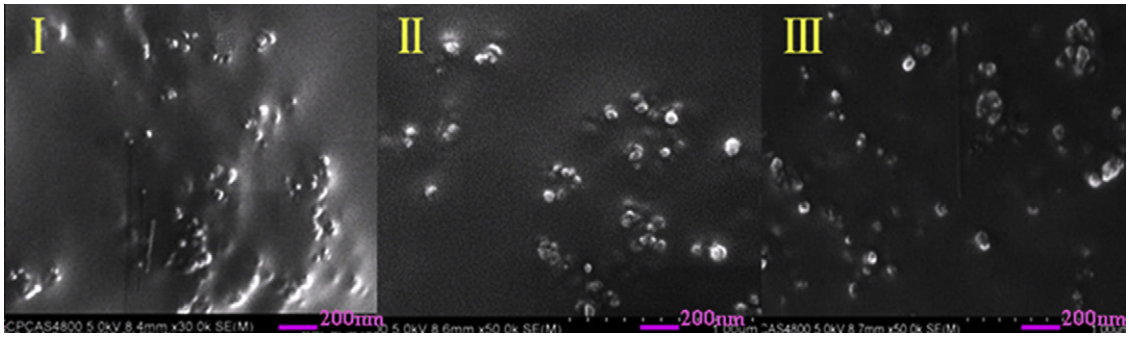

Fig. 4. SEM photography of polymeric micelles. (I) Blank polymeric micelles; (II) polymeric micelles loaded BBSKE; and (III) polymeric micelles loaded BBSKE and coated with folic acid.

Table 2
Investigation of cell growth inhibition for 24 h, 48 h, 72 h, $IC_{50} \pm SD$ (μM).

Group	24 h	48 h	72 h
BBSKE	7.14 ± 1.04	5.05 ± 0.16	4.23 ± 0.40
PM	10.54 ± 1.81	10.13 ± 1.20*	7.29 ± 0.64*
FA + PM	4.14 ± 0.06*,#	3.99 ± 0.10*,#	3.43 ± 0.31#
FA + PM + free FA (1:10)	7.84 ± 0.11†	6.88 ± 0.18*,#,†	6.30 ± 0.73†

Note: FA: folic acid; PM: BBSKE polymer micelles; FA + PM: BBSKE polymer micelles coated with folic acid; FA + PM + FA (1:10): BBSKE polymer micelles coated with folic acid as target and with free folic acid (1:10) as antagonist. Data are presented as means ± SD ($n = 3$).

* $P < 0.05$ (Student's t-test) significantly different from BBSKE group.

\# $P < 0.05$ (Student's t-test) significantly different from PM group.

† $P < 0.05$ (Student's t-test) significantly different from FA-PM group.

expressed on the surface of these breast tumor cells and one group of our polymeric micelles containing anticancer drug was coated with folate. Thus the polymeric micelles coated with folate can be absorbed into the tumor cells through receptor-mediated way, allowing it to function more effectively in killing the tumor cells. Our idea was confirmed by the data we acquired from the MTT experiment.

We have tested the cell growth inhibition of BBSKE for three different time intervals: 24 h, 48 h, and 72 h. From Table 2 it can be viewed that with the extension of time, the inhibition effect of BBSKE to tumor cells by anti-tumor drugs naked or loaded in copolymer micelles were increasingly elevated, which illustrated a certain degree of time-dependent manner. In the four groups, the inhibition effect to tumor cells growth was FA + PM group > BBSKE group > FA + PM + free FA (1:10) group > group of PM. IC_{50} of naked BBSKE was 7.14 μM, 5.05 μM and 4.23 μM when MCF-7 cells were treated with BBSKE for 24 h, 48 h and 72 h, respectively. Compared with naked BBSKE, the IC_{50} value of FA + PM group significantly declined when treatment time was 24 h (4.14 μM) and 48 h (3.99 μM). However, when the time was extended 72 h, a significant difference was not witnessed between naked BBSKE group and FA + PM group, though FA + PM group (3.43 μM) has a slightly lower IC_{50} than naked BBSKE group (4.23 μM). The difference between naked BBSKE group and FA + PM group became smaller as the time was extended from 24 h to 72 h. This result implied that copolymer micelles loading BBSKE and coated with folate can be absorbed into MCF-7 cells faster than naked BBSKE due to the interaction between folate coated on the surface of micelles and folate receptors situated at the surface of MCF-7 cells. It is the interaction between folate and folate receptors that ensured that more drugs were pumped into the tumor cells and showed a better anticancer effect (Hyuk and Tae, 2004).

When the inhibition effect of FA + PM group was compared with that of FA + PM + free FA (1:10) group, we found that when tumor cells were treated with drugs for 24 h, the inhibition effect of FA + PM was 2.55 times larger than that of PM. As time extended to 48 h and 72 h, the inhibition effect of FA + PM was 2.54 times and 2.13 times larger than that of PM, respectively. This means that free folate weakened the inhibitory effect significantly. This result can be attributed to the fact that excessive amount of free folic acid pre-occupied the folate receptors on the cell surface, which led the decreased interaction between folate coated copolymer micelles and folate receptors. Thus the data above offered us an evidence to elicit the conclusion that the folate employed as a targeting moiety significantly improved the inhibition effect of copolymer micelles loading BBSKE through the approach of receptor-mediated endocytosis.

As shown in Table 2 the inhibition effect to MCF-7 cells of group BBSKE polymeric micelles without folate (PM) was not as well as naked BBSKE. When BBSKE polymer micelles enter into cancer cells, they have to release BBKE first and then the drug can perform the function of killing the cancer. However, the naked BBSKE entered into cancer cells can kill them directly. Thus, at the cell level, BBSKE polymer micelles have a weaker suppression of tumor cell growth than naked BBSKE.

3.4. Confocal and flow cytometry study

In the experiment of Confocal and flow cytometry we also selected MCF-7 cells as the candidate cancer cells for our study. As shown in Fig. 6A, hoechst33342 is used to label the nucleus and its

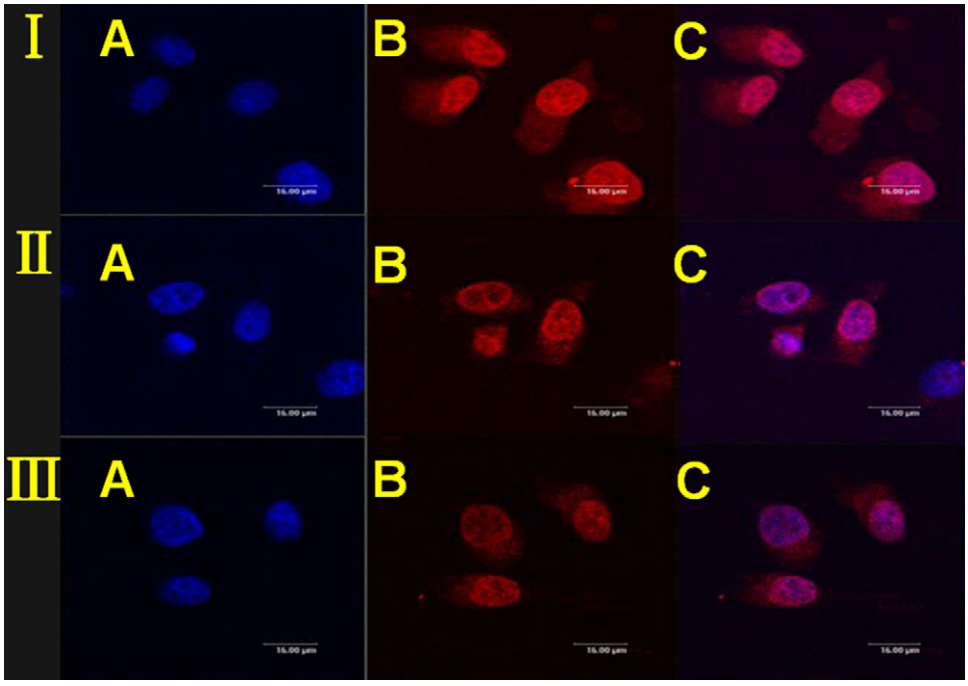

Fig. 6. Confocal microscopic images of MCF-7 cells incubated with polymeric micelles in the medium. (I) Folate-PEG-PLA-DOX/BBSKE; (II) PEG-PLA-DOX/BBSKE; and (III) free folate and folate-PEG-PLA-DOX/BBSKE. (A) Signal of hoechst33342; (B) signal of DOX; and (C) combination signals of hoechst33342 and DOX.

signal is blue, this signal can help us to locate a cell. Fig. 6B depicts the situation of polymer micelles entered into the cells with DOX as fluorescent indicator (red signal). Through the strength of DOX fluorescent signal we can acquire the information about how much copolymer micelles entered into cancer cells. The stronger the signal of DOX is, the more copolymer micelles are absorbed into cancer cells. Meanwhile, we can observe combination signals of hoechst33342 and signal of DOX in Fig. 6C. Group I in Fig. 6 are MCF-7 cells treated with FA-PEG-PLA-DOX/BBSKE. While group II in Fig. 6 and group III in Fig. 6 are MCF-7 cells treated with PEG-PLA-DOX/BBSKE and folate-PEG-PLA-DOX/BBSKE + free folate, respectively. Through the comparison of the three groups, we can clearly see that the cells treated with the polymer micelles coated by folate have stronger fluorescent signal than the cells treated by the polymer micelles without folate. This result indicated that the number of polymer micelles with folate entered into the cells were greater than that of polymer micelles without folate. However, when it comes to the cells treated with drug-loaded polymer micelles coated by folate together with free folate, the signal diminished conspicuously, which indicated the free folate and folate coated on the surface the micelles compete to anchor the folate receptor located at the surface of cancer cells. Thus the conclusion was self-evident, that micelles coated with folate can entered into the cancer cells through the access of receptor-mediated endocytosis. In addition, the results of Confocal are consistent with the results of cancer cell growth inhibition study, and they provide us evidence to explain the improved inhibition effect of BBSKE copolymer micelles with folate to MCF-7 cell growth.

Flow cytometry study was employed to verify the Confocal results. As shown in Fig. 7, Fig. 7I shows MCF-7 cells incubated with FA-PEG-PLA-DOX/BBSKE, Fig. 7II shows MCF-7 cells incubated with PEG-PLA-DOX/BBSKE and Fig. 7III shows MCF-7 cells incubated with free folate and folate-PEG-PLA-DOX/BBSKE. The study of the flow cytometry revealed the same result as to Confocal that is the folate-mediated active targeting of drugs increased the amount of drugs pumped into cancer cells. As a result polymer micelles with folate demonstrated better anti-tumor effect in comparison to naked drugs.

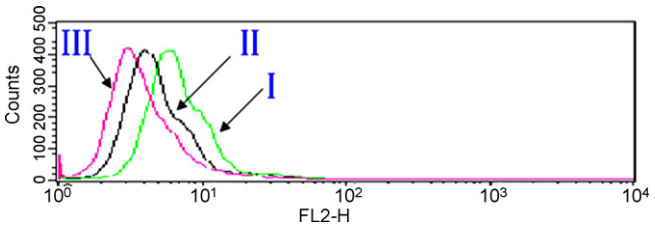

Fig. 7. Flow cytometry results of polymeric micelles. (I) FA-PEG-PLA-DOX/BBSKE; (II) PEG-PLA-DOX/BBSKE; and (III) free folate and folate-PEG-PLA-DOX/BBSKE.

3.5. Study of tissue distribution by imaging in vivo method

Imaging in vivo method was employed to study the tissue distribution of BBSKE polymeric micelles in nude mice with and without tumor. Through the comparison of these two situations, we can obtain a conclusion that polymeric micelles can aggregate in tumor site.

3.5.1. Tissue distribution of BBSKE polymeric micelles in mice without tumor

Fig. 8 depicted the distribution of polymer micelles after the same amount of micelles were injected into nude mice without tumor through the access of intravenous for 2.5 h and 24 h. Fig. 8A and B shows the situation of nude mice when they were viewed

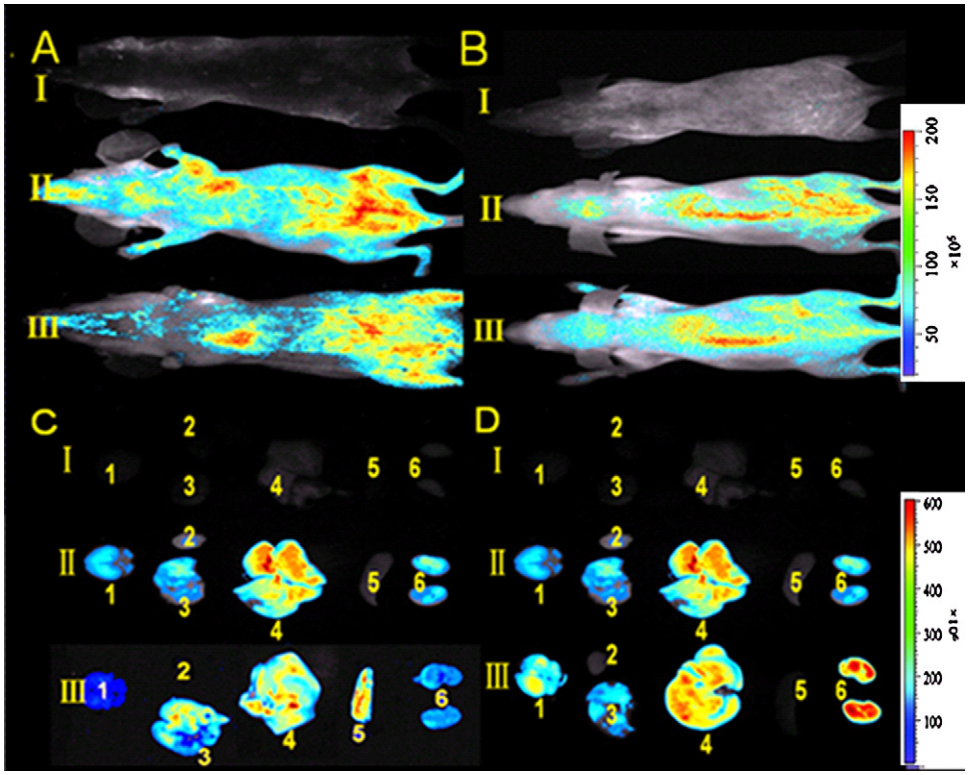

Fig. 8. Tissue distribution of BBSKE polymeric micelles in nude mice without tumor. (A) Viewed from abdomen; (B) viewed from back; (C, D) viewed from organs. (I) Group control; (II) group intravenous injected with PEG-PLA-DOX/BBSKE, 2.5 h; (III) group intravenous injected with PEG-PLA-DOX/BBSKE, 24 h, for A, B and C; (III) group administrated with PEG-PLA-DOX/BBSKE orally, 4 h, for D. 1: Brain; 2: heart; 3: lung; 4: liver; 5: spleen; and 6: kidney.

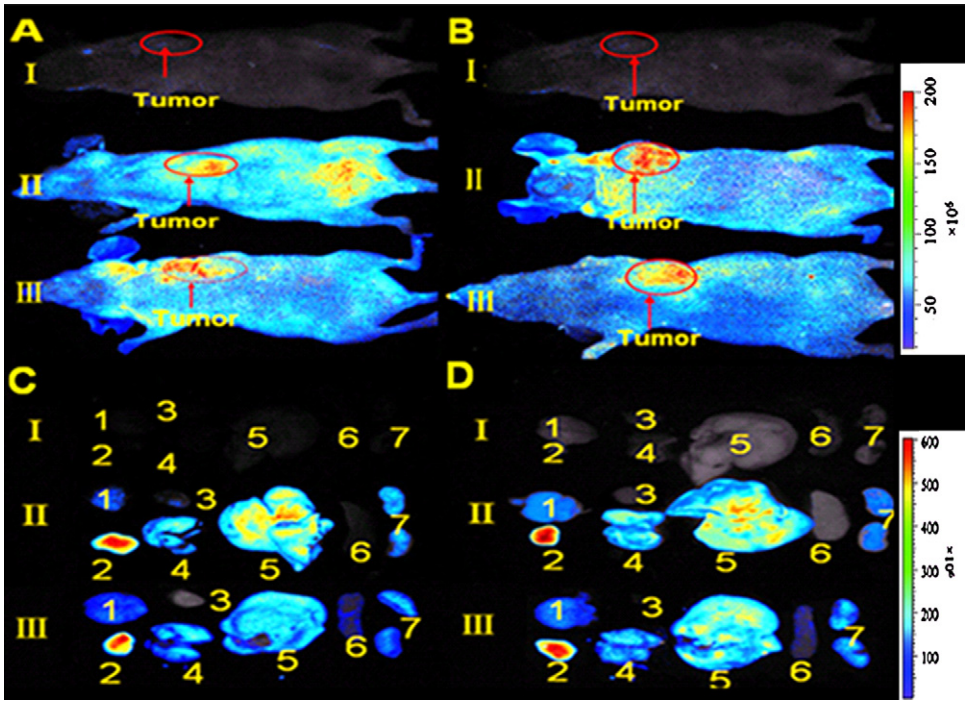

Fig. 9. Tissue distribution of BBSKE polymeric micelles in nude mice with tumor. (A, C) Group intravenous injected with PEG-PLA-DOX/BBSKE; (B, D) group intravenous injected with folate-PEG-PLA-DOX/BBSKE. (I) Group control; (II) group treatment (intravenous injection, 2.5 h); (III) group treatment (intravenous injection, 24 h). 1: Brain; 2: tumor; 3: heart; 4: lung; 5: liver; 6: spleen; and 7: kidney.

from abdomen and back, respectively. While, the tissue distribution of BBSKE polymer micelles in nude mice viewed from organs are shown in Fig. 8C. In Fig. 8A–C, I is group control; II is group intravenous injected with PEG-PLA-DOX/BBSKE and had taken a photograph after 2.5 h; III is group intravenous injected with PEG-PLA-DOX/BBSKE and take a photograph after 24 h. There are no micelles distributed into heart neither for 2.5 h nor for 24 h. However, an obvious difference in distribution of micelles between 2.5 h and 24 h can be observed from Fig. 8. As shown in Fig. 8C.II, there were no polymeric micelles distributed into spleen after polymeric micelles were intravenously injected into nude mice after 2.5 h. However, when time was extended to 24 h, the polymeric micelles distributed in the spleen were significantly increased. Meanwhile, the amount of micelles in the lung administrated after 24 h only enhanced slightly as compared with the situation after treated 2.5 h. However, the distributions of micelles in other organs were weakened to varying degrees. An organ that should draw our especial attention was the brain, whose blood–brain barrier causes the drugs in general to have difficulty entering the brain. But as shown above tri-block copolymer micelles can enter into the brain in a certain degree. This was a matter of great significance, which indicated that copolymer micelles provided an alternative method for future treatment of brain tumors.

Fig. 8D vividly shows us the tissue distribution comparison between two types of administration of polymer micelle – intravenous and oral. I is group control; II is group intravenous injected with PEG-PLA-DOX/BBSKE and a photograph taken after 2.5 h; III is group treated with PEG-PLA-DOX/BBSKE through oral approach and a photograph taken after 4 h. Oral administration had a process of absorption, so we observed the distribution of oral administration after 4 h, and the dose of oral administration was 2.5 times larger than that of the injection. From the results we observed that the differences between oral administration of micelles and intravenous administration of micelles mainly exist in two organs – brain and kidney. As shown in Fig. 8D, when polymeric micelles were administrated orally the quantity of polymeric micelles gathered in kidney increased tremendously, compared with the situation when polymeric micelles were administrated through injection. In addition, the quantity of polymeric micelles gathered in brain was slightly increased than when they were administrated orally. The result that micelles are distributed in the brain prompts us to suppose that micelles are absorbed into the blood circulation as an integrated form. They could not penetrate the BBB and accumulate in brain if they were not absorbed into the blood circulation as a nanoparticle.

3.5.2. Tissue distribution of BBSKE polymeric micelles in mice with tumor

As shown in Fig. 9, tissue distribution study of BBSKE polymer micelles in nude mice with tumor revealed the fact that tri-block copolymer micelles have the trend of aggregating in the tumor site. Fig. 9A and C shows the results when nude mice with tumor were intravenously injected with PEG-PLA-DOX/BBSKE. Fig. 9B and D shows the results when nude mice with tumor were intravenously injected with folate-PEG-PLA-DOX/BBSKE. In Fig. 9, I is group control; II is group that was intravenously injected with polymeric micelles and a photograph taken after 2.5 h; III is group that was intravenously injected with polymeric micelles and a photograph taken after 24 h.

Fluorescence was employed as a detection signal. So the stronger the florescence signal of an organ was, the larger the quantity of polymeric micelles accumulated in the organ was. From Fig. 9 we can find that polymeric micelles have a high concentration in tumor site. For both folate modified polymeric micelles and polymeric micelles without folate, the accumulation amount in the tumor was comparatively higher than in any other organ. At the same time, polymeric micelles scattered into the brain, kidney, liver and spleen were reduced compared with the situation in nude mice without tumor. Among these organs, polymeric micelles distributed in spleen reduced the most significantly. Meanwhile, the quantity of polymeric micelles aggregated in liver also declined conspicuously. When we compared Fig. 9A and C with B and

D, respectively, we found that nude mice injected with folate-PEG-PLA-DOX/BBSKE have stronger fluorescence signal in tumor tissue than nude mice injected with PEG-PLA-DOX/BBSKE, both at 2.5 h and 24 h. This result indicates that folate modified polymeric micelles performed a stronger aggregation behavior in tumor site than polymeric micelles which were not coated with folate, when the same amount of polymeric micelles were injected into nude mice.

The results above offer us evidence to elicit a conclusion that polymeric micelles tend to accumulate at solid tumors. We can attribute enhanced permeation and retention (EPR) effect (Kataoka et al., 1992; Colin et al., 1994; Kwon and Okano, 1996; Minko et al., 1998; Yoo et al., 1999) as a major mechanism for their unique bio-distribution profile in the tumor tissue. Fast growing tumor tissues need a tremendous amount of oxygen and nutrients supplied by blood vessels. They release special growth factors including vascular endothelial cell growth factor (VEGF) to facilitate neo-vascularization. As a result, many new vessels are formed, but their cell junctions are not as tight as those of normal tissues. Thus, polymeric micelles having a size of about 100 nm were likely to freely pass through the endothelial junctions of the capillaries in tumor tissue, but not in normal tissue. In our study, the particle size of polymeric micelles we prepared was less than 100 nm, so they can pass the vascular endothelial in tumor tissue and accumulate in tumor tissues. Moreover, because polymeric micelles were decorated with PEG chains on the surface, their circulation time in the blood stream was greatly prolonged which is also beneficial by accumulating in tumor tissue (Klibanov et al., 1990). In addition, folate modified polymeric micelles that were accumulated in the solid tumor region might be more readily taken up by tumor cells by a receptor-mediated endocytosis process. This indicates that PEG-PLA tri-block polymeric micelles without targeting motif can gather in tumor site through passive targeting-EPR effect and long circulation effect, while a ligand-mediated polymeric nanoparticle system for anticancer drug delivery with both a passive targeting property through a size effect, and an active targeting activity through specific recognition of ligand. The passive targeting allowed folate modified polymeric micelles aggregate in the tumor site, while the active targeting permitted them to be readily taken up by tumor cells at the site. Thus the combined passive and active targeting effects were likely to act synergistically, and they were mainly responsible for accumulation trends to tumor tissue. Therefore, polymeric micelles coated with folate have a slightly stronger accumulation trends than polymeric micelles that were not modified by folate.

4. Conclusion

In our study, we prepared a kind of tri-block copolymer micelles as carriers for novel anticancer drug BBSKE, utilizing the material PEG-PLA that we synthesized. The polymeric micelles improved the water solubility of BBSKE. Therefore, it was made to be a more promising formulation for this new anticancer drug. Folate was coated on the surface of this nanoparticle, which made the inhibition effect of copolymer micelles to MCF-7 tumor cells significantly better. By adopting a new method of imaging in vivo, we studied the distribution of micelles in nude mice with MCF-7 tumor and without MCF-7 tumor, which showed that this polymer micelles loading BBSKE could accumulate into tumor efficiently.

Acknowledgements

The assistance provided by Chilong Health Care International Limited Corporation and their professional technician Zuofu Peng in vivo imaging experiment is gratefully acknowledged.

Appendix A. Supplementary data

Supplementary data associated with this article can be found, in the online version, at doi:10.1016/j.ijpharm.2010.03.001.

References

Chen, X.M., Xun, W., Yue, H., Xuan, Z., Qiang, Z., 2009. A comparison study of the targeting properties of NGR-liposomes and RGD-liposomes towards human umbilical vein endothelial cells. J. Chin. Pharm. Sci. 18, 162–169.
Colin, deV., Dubernet, C., Nemati, F., Poupon, M.F., Puisieux, F., Couvreur, P., 1994. Uptake of doxorubicin from loaded nanoparticles in multidrug resistant leukemic murine cells. Cancer Chemother. Pharmacol. 33, 504–508.
Cummings, J., McArdle, C.S., 1986. Studies on the in vivo disposition of adriamycin in human tumors which exhibit different responses to the drug. Br. J. Cancer 53, 835–838.
Deiry, W.S., Tokino, T., Velculescu, V.E., Levy, D.B., Parsons, R., Trent, J.M., Lin, D., Mercer, W.E., Kinzler, K.W., Vogelstein, B., 1993. WAF-1, a potential mediator of p53 tumour suppression. Cell 75, 817–825.
Deng, S., Kuang, B., Zhou, X., Yan, J., Zhao, F., Jia, X., 2003. BBSKE, 1,2-[bis(1,2-benzisoselenazolone-3(2H)-ketone)]ethane, induced cell death in tumor cells. J. Peking Univ. (Health Sci.) 35, 108–109.
Erina, V., Kwanghee, K., Chann, L., Lorenza, D.D., John, T.M., Mansoureh, E., James, W.S., Encrico, S., William, M., Frank, P., 2009. In vivo imaging, tracking, and targeting of cancer stem cells. J. Natl. Cancer Inst. 101, 350–359.
Frank, F., Dickson, Eva, F.G., Roy, H.P., 2002. In vivo fluorescence imaging using two excitation and/or emission wavelengths for image contrast enhancement. Vib. Spectrosc. 30, 131–137.
Gasdaska, J.R., Berggren, M., Powis, G., 1995. Cell growth stimulation by the redox protein thioredoxin occurs by a novel helper mechanism. Cell Growth Differ. 6, 1642–1650.
Goren, D., Horowitz, A.T., Tzemach, D., Tarshish, M., Zalipsky, S., Gabizon, A., 2000. Nuclear delivery of doxorubicin via folate targeted liposomes with bypass of multidrug-resistance efflux. Clin. Cancer Res. 6, 1949–1957.
Guangya, X., Jun, W., Yanhui, L., Zhilan, L., Robert, J.L., 2008. Synthesis and evaluation of a novel ligand for folate-mediated targeting liposomes. Int. J. Pharm. 356, 29–36.
Guo, W., Lee, T., Sudimack, J.J., Lee, R.J., 2000. Receptor-specific delivery of liposomes via folate-PEG-chol. J. Liposome Res. 10, 179–195.
Hagan, S.A., Coombes, A.G.A., Garnett, M.C., Dunn, S.E., Davies, M.C., Illum, L., Davis, S.S., 1996. Polylactide-poly(ethylene glycol) copolymers as drug delivery systems. 1. Characterization of water dispersible micelle-forming systems. Langmuir 12, 2153–2161.
Hamaguchi, T., Kato, K., Yasui, H., Morizane, C., Ikeda, M., Ueno, H., Muro, K., Yamada, Y., Okusaka, T., Shirao, K., Shimada, Y., Nakahama, H., Matsumura, Y., 2007. A phase I and pharmacokinetic study of NK105, a paclitaxel-incorporating micellar nanoparticle formulation. Br. J. Cancer 97, 170–176.
Harper, J.W., Adami, G.R., Wei, N., Keyomarsi, K., Elledge, S.J., 1993. The p21 Cdk-interacting protein Cip1 is a potent inhibitor of G1 cyclin independent kinases. Cell 75, 805–816.
Holmgren, A., 1985. Thioredoxin. Annu. Rev. Biochem. 54, 237–271.
Hyuk, S.Y., Tae, G.P., 2004. Folate receptor targeted biodegradable polymeric doxorubicin micelles. J. Controlled Release 96, 273–283.
Ishida, T., Kirchmeier, M.J., Moase, E.H., Zalipsky, S., Allen, T.M., 2001. Targeted delivery and triggered release of liposomal doxorubicin enhances cytotoxicity against human B lymphoma cells. Biochim. Biophys. Acta 1515, 144–158.
Jae, H., Seunglee, K., Ju, O.N., Rang, W.P., Hesson, C., Sang, B.S., In, S.K., Ick, C.K., Seo, Y.J., 2004. Self-assembled nanoparticles based on glycol chitosan bearing 5h-cholanic acid for RGD peptide delivery. J. Controlled Release 95, 579–588.
Jaeyoung, L., Eun, C.C., Kilwon, C., 2004. Incorporation and release behavior of hydrophobic drug in functionalized poly(D,L-lactide)-block-poly(ethylene oxide) micelles. J. Controlled Release 94, 323–335.
Kataoka, K., Kwon, G., Yokoyama, M., Okano, T., Sakurai, Y., 1992. Block copolymer micelles as vehicles for drug delivery. J. Controlled Release 24, 119–132.
Kataoka, K., Matsumoto, T., Yokoyama, M., Okano, T., Sakurai, Y., Fukushima, S., Okamoto, K., Kwon, G.S., 2000. Doxorubicin-loaded poly(ethylene glycol)-poly(ß-benzyl-L-aspartate) copolymer micelles: their pharmaceutical characteristics and biological significance. J. Controlled Release 64, 143–153.
Klibanov, A.L., Maruyama, K., Torchilin, V.P., Huang, L., 1990. Amphipathic polyethylene glycols effectively prolong the circulation time of liposomes. FEBS Lett. 268, 235–237.
Kwon, G.S., Okano, T., 1996. Polymeric micelle as new drug carriers. Adv. Drug. Deliv. Rev. 16, 107–116.
Kwon, G., Naito, M., Yokoyama, M., Okano, T., Sakurai, Y., Kataoka, K., 1993. Micelles based on AB block copolymers of poly (ethylene oxide) and poly(h-benzyl-L-aspartate). Langmuir 9, 945–949.
Kwon, G., Suwa, S., Yokoyama, M., Okano, T., Sakurai, Y., Kataoka, K., 1994. J. Controlled Release 29, 17.
Lee, R.J., Low, P.S., 1995. Folate-mediated tumor cell targeting of liposome-entrapped doxorubicin in vitro. Biochim. Biophys. Acta 1233, 134–144.
Lu, Y., Low, P.S., 2002. Folate targeting of haptens to cancer cell surfaces mediates immunotherapy of syngeneic murine tumors. Cancer Immunol. Immunother. 51, 153–162.

Lu, J.Y., Lowe, D.A., Kennedy, M.D., Low, P.S., 1999. Folate-targeted enzyme prodrug cancer therapy utilizing penicillin-V amidase and a doxorubicin prodrug. J. Drug Target. 7, 44–53.

Maha, S., Olga, B.G., Elizabeth, B., Pooja, C., Jayant, J.K., Vitaly, P.P., Tamara, M., 2008. Receptor targeted polymers, dendrimers, liposomes: which nanocarrier is the most efficient for tumor-specific treatment and imaging? J. Controlled Release 130, 107–114.

Michael, J.W.J., Sean, C.S., Sandra, K.K., Katarina, E., Merete, L.E., Esther, C.L., Göran, K., Daniel, Y., Pieter, R.C., 2006. Therapeutically optimized rates of drug release can be achieved by varying the drug-to-lipid ratio in liposomal vincristine formulations. Biochim. Biophys. Acta 1758, 55–64.

Minko, T., Kopeckova, P., Pozharov, V., Kopecek, J., 1998. HPMA copolymer bound adriamycin overcomes MDR1 gene encoded resistance in a human ovarian carcinoma cell line. J. Controlled Release 54, 223–233.

Muraru, L., Lierde, C.V., Naert, I., Sloten, J.V., Jaecques, S.V.N., 2009. Three-dimensional finite element models based on in vivo microfocus computed tomography: elimination of metal artefacts in a small laboratory animal model by registration with artefact-free reference images. Adv. Eng. Software 40, 1207–1210.

Reddy, J.A., Low, P.S., 2000. Enhanced folate receptor mediated gene therapy using a novel pH-sensitive lipid formulation. J. Controlled Release 64, 27–37.

Sabine, U., Katja, B., 2006. On the potential of thioredoxin reductase inhibitors for cancer therapy. Semin. Cancer Biol. 16, 452–465.

Shi, C., Yu, L., Yang, F., Yan, J., Zeng, H., 2003. A novel organoselenium compound induces cell cycle arrest and apoptosis in prostate cancer cell lines. Biochem. Biophys. Res. Commun. 309, 578–583.

Sung, C.K., Dong, W.K., Yong, H.S., Joon, S.B., Hun, S.O., Sung, W.K., Min, H.S., 2001. In vivo evaluation of polymeric micellar paclitaxel formulation: toxicity and efficacy. J. Controlled Release 72, 191–202.

Tomoyuki, M., Kohta, M., Shiho, N., Kazumi, D., Hirokazu, O., 2009. Dual imaging of pulmonary delivery and gene expression of dry powder inhalant by fluorescence and bioluminescence. J. Controlled Release 134, 149–154.

Uchino, H., Matsumura, Y., Negishi, T., Koizumi, F., Hayashi, T., Honda, T., Nishiyama, N., Kataoka, K., Naito, S., Kakizoe, T., 2005. Cisplatin-incorporating polymeric micelles (NC-6004) can reduce nephrotoxicity and neurotoxicity of cisplatin in rats. Br. J. Cancer 93, 678–687.

Valery, A., Evgueni, K., Shengmin, L., Grzegorz, P., Annie, V., Elena, B., Tatiana, B., Alexander, K., 1999. Block copolymer-based formulation of doxorubicin. From cell screen to clinical trials. Colloids Surf., B: Biointerfaces 16, 113–134.

Wang, S., Lee, R.J., Cauchon, G., Gorenstein, D.G., 1995. Delivery of antisense oligodeoxyribonucleotides against the human epidermal growth factor receptor into cultured KB cells with liposomes conjugated to folate via polyethyleneglycol. Proc. Natl. Acad. Sci. U.S.A. 92, 3318–3322.

Weitman, S.D., Weinberg, A.G., Coney, L.R., Zurawski, V.R., Jennings, D.S., Kamen, B.A., 1992. Cellular localization of the folate receptor: potential role in drug toxicity and folate homeostasis. Cancer Res. 52, 6708–6711.

Weiyang, S., Junmin, X., Yiyan, Y., 2007. Targeted and intracellular delivery of paclitaxel using multi-functional polymeric micelles. Biomaterials 28, 1730–1740.

Xinru, L., Zhuoli, Y., Kewei, Y., Yanxia, Z., Xingwei, C., Yanhui, Z., Fei, W., Yan, L., Lijun, R., 2009. Self-assembled polymeric micellar nanoparticles as nanocarriers for poorly soluble anticancer drug Ethaselen. Nanoscale Res. Lett. doi:10.1007/s11671-009-9427-2.

Xiong, Y., Hannon, G.J., Zang, H., Casso, D., Kobayashi, R., Beach, D., 1993. p21 is a universal inhibitor of cyclin kinase. Nature 366, 701–704.

Xiong, X.B., Yue, H., Lu, W.L., Xuan, Z., Hua, Z., Tsuneji, N., Qiang, Z., 2005. Enhanced intracellular delivery and improved antitumor efficacy of doxorubicin by sterically stabilized liposomes modified with a synthetic RGD mimetic. J. Controlled Release 107, 262–275.

Xue, Y., He, W., Wan-Liang, L., Ju, D., Jia, G., Wei, T., Ying, M., Yan, Z., Ruo, J.L., Ting, Y.Y., De, W.S., Jin, N.L., Liang, R.Z., Qiang, Z., 2010. Dual-targeting daunorubicin liposomes improve the therapeutic efficacy of brain glioma in animals. J. Controlled Release 141, 183–192.

Yan, J., Deng, S., Kuang, B., He, F., Liu, T., Zeng, H., 2004. Selenium distribution pattern, antineoplastic and immunostimulatory activities of a novel organoselenium compound Eb. J. Chin. Pharm. Sci. 13, 199–204.

Yoo, H.S., Park, T.G., 2001. Biodegradable polymeric micelles composed of doxorubicin conjugated PLGA–PEG block copolymer. J. Controlled Release 70, 63–70.

Yoo, H.S., Oh, J.E., Lee, K.H., Park, T.G., 1999. Biodegradable nanoparticles containing doxorubicin-PLGA conjugates for sustained release. Pharm. Res. 16, 1114–1118.

Zhao, F., Yan, J., Deng, S.J., Lan,.L.X., He, F., Kuang, B., Zeng, H.H., 2006. A thioredoxin reductase inhibitor induces growth inhibition and apoptosis in five cultured human carcinoma cell lines. Cancer Lett. 236, 46–53.

Zhigang, X., Huili, G., Xuesi, C., Changhai, L., Li, C., Xiuli, H., Quan, S., Xiabin, J., 2007. A novel polymer-paclitaxel conjugate based on amphiphilic triblock copolymer. J. Controlled Release 117, 210–216.

Free Radical Biology & Medicine 52 (2012) 898–908

Contents lists available at SciVerse ScienceDirect

Free Radical Biology & Medicine

journal homepage: www.elsevier.com/locate/freeradbiomed

Original Contribution

Ethaselen: a potent mammalian thioredoxin reductase 1 inhibitor and novel organoselenium anticancer agent

Lihui Wang [a,b,c], Zhiyu Yang [a,b], Jianing Fu [a,b], Hanwei Yin [d], Kun Xiong [d], Qiang Tan [b,e], Hongwei Jin [a], Jing Li [a,b], Tianyu Wang [d], Wanchen Tang [a,b], Jin Yin [a,b], Gaoxiong Cai [a,b], Mi Liu [a,b], Sebastian Kehr [c], Katja Becker [c], Huihui Zeng [a,b,*]

[a] State Key Laboratory of Natural and Biomimetic Drugs, Peking University, Beijing 100191, China
[b] School of Pharmaceutical Sciences, Peking University, Beijing 100191, China
[c] Interdisciplinary Research Center, Justus Liebig University, Giessen D-35392, Germany
[d] College of Life Sciences, Peking University, Beijing 100075, China
[e] Peking University First Hospital, Beijing 100034, China

ARTICLE INFO

Article history:
Received 7 July 2011
Revised 14 November 2011
Accepted 29 November 2011
Available online 21 December 2011

Keywords:
Mammalian thioredoxin reductase 1
Thioredoxin
Ethaselen
Enzyme inhibitor
Selenium compound
Anticancer agent
Free radicals

ABSTRACT

Mammalian thioredoxin reductase 1 (TrxR1) is considered to be an important anticancer drug target and to be involved in both carcinogenesis and cancer progression. Here, we report that ethaselen, a novel organoselenium compound with anticancer activity, specifically binds to the unique selenocysteine–cysteine redox pair in the C-terminal active site of mammalian TrxR1. Ethaselen was found to be a potent inhibitor rather than an efficient substrate of mammalian TrxR1. It effectively inhibits wild-type mammalian TrxR1 at submicromolar concentrations with an initial mixed-type inhibition pattern. By using recombinant human TrxR1 variants and human glutathione reductase, we prove that ethaselen specifically targets the C-terminal but not the N-terminal active site of mammalian TrxR1. In A549 human lung cancer cells, ethaselen significantly suppresses cell viability in parallel with direct inhibition of TrxR1 activity. It does not, however, alter either the disulfide-reduction capability of thioredoxin or the activity of glutathione reductase. As a downstream effect of TrxR1 inactivation, ethaselen causes a dose-dependent thioredoxin oxidation and enhances the levels of cellular reactive oxygen species in A549 cells. Thus, we propose ethaselen as the first selenium-containing inhibitor of mammalian TrxR1 and provide evidence that selenium compounds can act as anticancer agents based on mammalian TrxR1 inhibition.

The thioredoxin system, composed of thioredoxin reductase (TrxR), thioredoxin (Trx), and NADPH, regulates various cellular processes, including antioxidant defense, redox homeostasis, cell proliferation, and apoptosis [1,2]. Thioredoxin reductase belongs to the family of pyridine nucleotide disulfide oxidoreductases, together with enzymes such as lipoamide dehydrogenase and glutathione reductase [3]. In mammals three TrxRs have been identified: (i) cytosolic TrxR1, (ii) mitochondrial TrxR2, and (iii) testis-specific TrxR3, which contains an additional N-terminal glutaredoxin domain [4]. All three mammalian TrxRs are selenocysteine-containing enzymes that catalyze the selenium-dependent reduction of the oxidized active-site disulfide (Cys32/Cys35) in thioredoxin [4]. Interestingly, increasing evidence indicates that TrxR1 plays important roles in the development and progression of cancer [1,5]. Many malignant cells overexpress TrxR1 and show markedly enhanced TrxR1 activity, possibly correlating with tumor aggressiveness, apoptosis inhibition, and increased resistance to chemotherapeutic treatment [1,4,6]. It was reported that reduction of TrxR1 levels in cancer cells reverses many characteristics of malignancy and inhibits cancer cell growth and DNA replication [7,8]. Further studies substantiate the notion that mammalian TrxR1 is a promising drug target for cancer therapy [9–11].

Mammalian TrxRs possess an N-terminal dithiol/disulfide redox motif with striking homology to human glutathione reductase (GR) [12]. However, mammalian TrxRs additionally possess a unique and conserved cysteine–selenocysteine (Cys–Sec) redox pair at the C-terminal active site [13,14]. It is believed that mammalian TrxR1 is able to reduce a variety of diverse substrates because of the inherent high reactivity and redox properties of the selenocysteine residue [13,14]. During catalysis electrons are transferred from NADPH via enzyme-bound FAD to the N-terminal active site, from where they are delivered to the oxidized C-terminal arm, reducing the

Abbreviations: ethaselen, 1,2-[bis(1,2-benzisoselenazolone 3(2*H*)-ketone)] ethane; GR, glutathione reductase; GSH, glutathione; GSH-Px, glutathione peroxidase; GSSG, glutathione disulfide; ROS, reactive oxygen species; Sec, selenocysteine; Trx, thioredoxin; TrxR, thioredoxin reductase.

* Corresponding author at: School of Pharmaceutical Sciences, Peking University, Beijing 100191, China. Fax: +86 10 62015584.
E-mail address: zenghh@bjmu.edu.cn (H. Zeng).

0891-5849/$ – see front matter © 2011 Elsevier Inc. All rights reserved.
doi:10.1016/j.freeradbiomed.2011.11.034

selenylsulfide (S–Se, formed by Cys497/Sec498) to a selenolthiol (–SH/–SeH). The current idea is that the reduced Sec498 residue attacks the active-site disulfide of Trx to form an intermolecular selenenylsulfide bond (Se–S, formed by TrxR Sec498 and Trx Cys32). Then the intermolecular selenylsulfide bond is reduced by Cys497 of TrxR via a thiol/selenenylsulfide exchange. As a result, reduced Trx is released and the oxidized C-terminal selenenylsulfide of TrxR is regenerated for the next cycle of catalysis [4,15]. As mentioned above, the C-terminal Sec is highly reactive and solvent exposed, which is thought to be the reason for the broad substrate specificity of mammalian TrxRs, at least in vitro [4,16]. Moreover, the inhibitory effects of many active compounds and drugs targeting mammalian TrxR1 are mainly based on their interactions with the Sec residue; prominent examples include gold- and platinum-based compounds, arsenic trioxide, motexafin gadolinium, antitumor quinols, curcumin, and natural flavonoids. In fact, inactivation of TrxR1 is considered to be involved in the described anticancer effects of these compounds [17–22].

Selenium compounds that are effective as anticancer agents are increasingly gaining interest for the development of new powerful cancer treatment strategies [23]. Ethaselen (1,2-[bis(1,2-benzisoselenazolone 3(2*H*)-ketone)] ethane, BBSKE), a promising organoselenium anticancer agent with low toxicity in animal models, has been developed by our group and is currently undergoing phase I clinical trials [24–29]. Its anticancer effectiveness has been proven in various human cancer cell lines and tumor-bearing mouse models [24–27,29,30]. Interestingly, the inhibition of cancer cell growth by ethaselen is correlated with TrxR1 inactivation in various investigated cell lines, including HeLa (human cervical cancer), BGC823 (human stomach adenocarcinoma), HL60 and K562 (human leukemia), A549 (human lung cancer), LoVo (human colon cancer), Bel-7402 (human epithelial hepatoma), Tca8113 (human tongue cancer), and KB (human nasopharyngeal epidermal carcinoma) cells [24–27]. In addition, ethaselen markedly suppresses tumor growth in human A549-grafted nude mice along with TrxR1 inactivation in tumor tissue [30]. However, the mechanism of action and the inhibitory properties of ethaselen on mammalian TrxR1 and its impact on the intracellular TrxR/Trx redox system remain to be elucidated in detail.

In this work, we provide evidence that ethaselen targets mammalian TrxR1 at the C-terminal active site acting as a potent inhibitor and a rather weak substrate of the enzyme. Disruption of the TrxR-dependent reduction of oxidized Trx by ethaselen leads to the accumulation of oxidized Trx and reactive oxygen species in A549 cells. Thus ethaselen, as a selenium-containing anticancer agent, can be added to the diversity of known mammalian TrxR inhibitors.

Materials and methods

Enzymes and reagents

Rat liver TrxR1, *Escherichia coli* TrxR and Trx, bovine insulin, reduced and oxidized glutathione, NADPH, 5,5′-dithiobis-2-nitrobenzoic acid (DTNB), iodoacetic acid, and 2′,7′-dichlorfluorescein diacetate (DCFH-DA) were obtained from Sigma–Aldrich (St. Louis, MO, USA). Human placental TrxR1, the recombinant Sec498Cys TrxR1 mutant (Sec → Cys), and the truncated TrxR1 missing the last two amino acids (Sec–Gly), as well as human GR and the human Trx mutant Cys73 → Ser (which does not form dimers and is stable in enzymatic assays), were produced as described before [31–34]. Ethaselen was synthesized in our group and dissolved in a stock solution of dimethyl sulfoxide (DMSO) as described [24]. All other reagents were of analytical grade.

Molecular docking and dynamics

The mammalian TrxR1 structure was obtained from the Protein Data Bank (PDB ID: 1H6V) [35]. A 1000-ps molecular dynamics (MD) simulation of the complex was done with an Amber 8 molecular simulation package [36]. The initial conformation was taken from the lowest binding energy docking conformation. It was then solvated in TIP3P water using an octahedral box, which was extended 8 Å away from any solute atom. The solvated system was neutralized by adding a sodium ion into the simulation. Molecular dynamics simulation was carried out using the SANDER (simulated annealing with NMR-derived energy restraints) module of Amber 8. The solvent (water molecules) was optimized with 250 steps of steepest descent followed by 750 steps of conjugate gradient, with a large constraint of 500 kcal mol^{-1} $Å^{-2}$ on solute (protein, counter ion, ligand) atoms. The full system was minimized using the steepest decent and conjugated gradient methods consecutively without a force constraint. After minimization, 100 ps of MD were done for the complex, during which the temperature was slowly increased from 0 to 300K. The production simulation of 1000 ps was followed at constant pressure (1 atm) and temperature (300K). SHAKE was applied to all hydrogen atoms in the entire simulation. A cutoff of 12 Å was used for Lennard–Jones interactions. The final structure of the complex of TrxR1 and ethaselen for future analysis was produced from the 1000 steps of the minimized and averaged structure of the last 500 ps of MD.

Enzyme assays

All enzyme activity assays and kinetic studies were carried out in at least three independent experiments at room temperature using a Hitachi U-2001 spectrophotometer.

Both DTNB and Trx reduction assays were used to measure TrxR activity [37,38]. Mammalian TrxRs were prereduced by incubation with NADPH for 5 min. Then reduced human placental TrxR1 (4 nM) and rat TrxR (0.15 μM) were incubated with different concentrations of ethaselen in 490 μl of 0.1 M phosphate buffer (200 μM NADPH, 1 mM EDTA, pH 7.5) and for different incubation times at room temperature in the dark. For the DTNB reduction assay, 10 μl of 0.1 M phosphate buffer containing DTNB (final concentration: 2 mM) was added. The increase in absorbance at 412 nm was recorded in the initial 3 min. Likewise the activities of the recombinant human TrxR1 variants (Sec498 → Cys TrxR1 mutant and Sec–Gly truncated TrxR1 mutant) in the presence of ethaselen were determined (concentrations of ethaselen up to 120 μM). For the Trx reduction assay, 10 μM human recombinant Trx was added, followed by monitoring the initial decrease in absorbance at 340 nm.

To investigate the inhibition kinetics of ethaselen on mammalian TrxR1, various concentrations of the disulfide substrate DTNB (31.25–2000 μM) and ethaselen (0–46.28 nM) were used [39]. After the simultaneous addition of DTNB and ethaselen into the reaction buffer containing 4 nM human TrxR1 and 200 μM NADPH, the increase in absorbance at 412 nm was recorded in the initial 60 s (the enzymatic reaction is linear during this period). The inhibition of human TrxR1 by ethaselen was analyzed using Lineweaver–Burk plots [39]. The inhibition constants K_i and K_{is} (equilibrium constants for the inhibitor binding to free enzyme and to the enzyme–substrate complex) were obtained by creating secondary plots of either the slope or the intercept of the primary plot against the concentration of ethaselen [40].

To study if ethaselen can be reduced by TrxR1, we adapted a DTNB-coupled assay to spectrophotometrically detect one of the two possible reduced forms (Scheme 1). DTNB is a sensitive and rapid thiol/selenothiol-detecting reagent. For the experimental design, low and high concentrations of ethaselen (8, 64, 100 μM) and human TrxR1 (4, 20, 40 nM), covering the same concentrations used in the experiments for Fig. 3, were employed. Ethaselen and human TrxR1 were incubated in 0.1 M phosphate buffer (1 mM EDTA, 200 μM NADPH, pH 7.4) at room temperature for various times (15, 30, and 60 min) in the dark. After the removal of human TrxR1 via a molecular weight cut-off 3000 filter (Vivaspin), DTNB

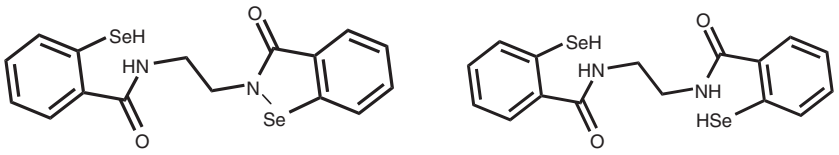

Scheme 1. Two possible reduced forms of ethaselen.

(final concentration: 1 mM) was immediately added into the flowthrough and reacted in the dark for 2 min. Then the absorbance at 412 nm was recorded by a Hitachi U-2001 spectrophotometer. Controls were done following the same procedure but either without human TrxR1 or without ethaselen in the incubation mixture.

GR activity was evaluated as described before [41]. Prereduced human GR (4 nM) was incubated with various concentrations of ethaselen (4–120 μM) in 485 μl reaction buffer (50 mM potassium phosphate, 1 mM EDTA, 200 mM KCl, and 100 mM NADPH, pH 6.9) for 10 min at 25 °C in the dark. When 15 μl of buffer containing glutathione disulfide (GSSG; final concentration: 1 mM) was added, GR activity was determined by measuring the consumption of NADPH, which was monitored as the decrease in absorbance at 340 nm for 3 min.

All enzyme activities are presented as percentages with the activity of control samples set to 100%. Control experiments were conducted analogously except for using DMSO alone without ethaselen.

NADPH oxidation assay

Various concentrations of ethaselen were added to 0.1 M phosphate buffer containing NADPH (100 μM), human TrxR1 (4, 20, and 40 nM), and EDTA (1 mM), pH 7.5, immediately followed by measuring the absorbance decrease at 340 nm for 3 min. The oxidation of NADPH without ethaselen was subtracted from this value. For the steady-state enzyme kinetic analysis, the NADPH oxidation rate was calculated from the initial 60 s (the enzymatic reaction is linear during this period) [42]. The kinetic parameters were calculated by nonlinear regression using the program SigmaPlot (version 11.0).

Determination of TrxR1 activity and the disulfide reduction capability of Trx in cell extracts

Enzyme activities in cell extracts were measured in 96-well plates using a Thermo Scientific Multiskan MK3 microplate reader. The end-point Trx-dependent insulin reduction assay was used to determine TrxR1 activity in cell extracts [38]. Cell extracts (30 μl) containing 40 μg total protein were incubated with 100 μl reaction buffer (0.2 M Hepes, 5 mM EDTA, 1 mM NADPH, 5 μM *E. coli* Trx, and 2.5 mg/ml bovine insulin, pH 7.6) for 30 min at 37 °C. After the addition of 120 μl stop solution (6 M guanidine–HCl, 50 mM Tris, and 1.5 mM DTNB, pH 8.0), the amount of free thiols generated from reduced insulin was determined with DTNB monitoring the change in absorbance at 412 nm (the extinction coefficient for the released 2-nitro-5-thiobenzoic acid is 13,600 M^{-1} cm^{-1}). For each sample, the corresponding background reaction was measured in the same assay by omitting *E. coli* Trx from the reaction buffer (control experiment). The TrxR1 activity in cell extracts was calculated by subtracting the background reaction from the total reaction.

For the measurement of the disulfide reduction capability of Trx in cell extracts, the end-point insulin reduction assay was used as described above, but with one modification: 0.2 μM rat TrxR was used in the reaction buffer instead of *E. coli* Trx [43]. Likewise rat TrxR was omitted to detect the background reaction of each sample. The disulfide reduction capability of Trx in cell extracts was then determined by subtracting the background reaction from the total reaction.

Determination of glutathione reductase activity in cell extracts

The glutathione reductase activity in cell extracts was measured by the GSSG reduction assay [41]. Cell extracts (30 μl) containing 40 μg total protein were incubated with 60 μl of buffer (50 mM potassium phosphate, 1 mM EDTA, 200 mM KCl, and 100 mM NADPH, pH 6.9) in the cuvette for 2 min at room temperature. After the addition of 10 μl glutathione disulfide (final concentration: 1 mM) and rapid mixing, the decrease in the absorbance at 340 nm was recorded for the initial 3 min by using an Agilent UV-8453 spectrophotometer.

Cell culture and cell viability assays

A549 and H1666 human lung cancer cells were commercially obtained from the Cell Resource Center, Peking Union Medical College (morphology check by microscope). Cells were cultured in Dulbecco's modified Eagle's medium with 10% fetal bovine serum and maintained in an atmosphere of 5% CO_2 at 37 °C. After exposure to various concentrations of ethaselen for 12 and 24 h, the cell viability was measured using the 3-(4,5-dimethylthiazol-2-yl)-2,5-diphenyltetrazolium bromide (MTT) assay as described [25].

Western blot analysis

Western blot analysis was carried out as previously described [44]. Briefly, 40 μg of total protein extracted from A549 cells was separated by SDS–PAGE and transferred onto polyvinylidene difluoride (PVDF) membranes. Membranes were blocked with 5% milk in TBST and incubated with anti-human TrxR1 and anti-human Trx antibodies (Santa Cruz Biotechnology, Santa Cruz, CA, USA). The blots were developed using enhanced chemiluminescence detection reagents (Amersham Biosciences, Amersham, UK) with peroxidase-conjugated secondary antibodies.

Reverse transcriptase-polymerase chain reaction (RT-PCR)

The mRNA level of human TrxR1 was measured by RT-PCR as described [44]. For human TrxR1 (185 bp) the primers were forward, 5′-CTAAAAATGAACGGCCCTGA-3′, and reverse, 5′-ACACATGTTCCTCC-GAGACC-3′. For GAPDH (202 bp) the primers were forward, 5′-TGTTGCCATCAATGACCCCTT-3′, and reverse, 5′-CTCCACGACGTACT-CAGCG-3′.

Detection of the redox status of thioredoxin (redox Western blot)

Ethaselen-treated and untreated A549 cells (2×10^5) were washed once with ice-cold phosphate-buffered saline (PBS; pH 7.2) to exclude contamination with secreted oxidized Trx. Cells were then lysed in 6 M guanidine–HCl lysis buffer (50 mM Tris, 3 mM EDTA, 0.5% Triton X-100, and 50 mM iodoacetic acid, pH 8.3) and incubated for 30 min at 37 °C in the dark. After excess iodoacetic acid was removed by MicroSpin G-25 columns (GE Healthcare, Piscataway, NJ, USA), samples (40 μg protein) were subjected to native PAGE

(15%). The reduced, partially oxidized (oxidation at Cys32/Cys35), and fully oxidized (oxidation at Cys32/Cys35 and Cys62/Cys69) Trxs were separated by electrophoretic analysis owing to the impaired mobility of iodoacetic acid–carboxymethylated cysteines of Trx's [45]. Then the proteins were electroblotted on a PVDF membrane and probed with specific primary and secondary antibodies. Bands were visualized by ECL detection reagents.

Measurement of intracellular levels of reactive oxygen species (ROS)

The production of reactive oxygen species was measured by a fluorescence method in ethaselen-treated A549 cells [46]. After treatment with ethaselen for 12 and 24 h, cells were harvested and washed twice with ice-cold PBS (pH 7.2). Then the cells were resuspended in PBS buffer containing 10 μM DCFH-DA dye (Sigma). After incubation for 20 min at 37 °C in the dark, the cells were washed twice with ice-cold PBS (pH 7.2). The intracellular fluorescence was measured immediately with a FACS (fluorescence-activated cell sorting) Calibur platform (BD Biosciences) at an excitation wavelength of 495 nm and an emission wavelength of 530 nm.

Results

Design of an organoselenium compound (ethaselen) targeting the Cys–Sec redox pair in mammalian TrxR1

Because mammalian TrxR1 has a unique and crucial Cys–Sec redox pair at the C-terminal active site, we aimed at synthesizing a small inhibitor that can specifically recognize and bind to the Cys–Sec redox motif. Ethaselen, an organoselenium compound containing symmetrical di-1,2-benzisoselenazol-3(2*H*)-ones as pharmacophores, was developed from this notion (Fig. 1A). As demonstrated in previous studies, the Se–N bond in the benzisoselenazol ring is a strong electrophilic site for reacting with thiol and selenolthiol groups of proteins [47]. Thus, based on the symmetrical structure of ethaselen, we expected that ethaselen could interact with the C-terminal Sec–SeH and Cys–SH of mammalian TrxR1 to form both an intermolecular diselenide bond (Se–Se) and an intermolecular selenenylsulfide (Se–S) bond with the protein. Molecular dynamics simulation was employed to study the proposed mechanism of interaction. As shown in Fig. 1B, ethaselen can readily gain access to the C-terminal active site, which is exposed to the protein surface [14,15]. Because

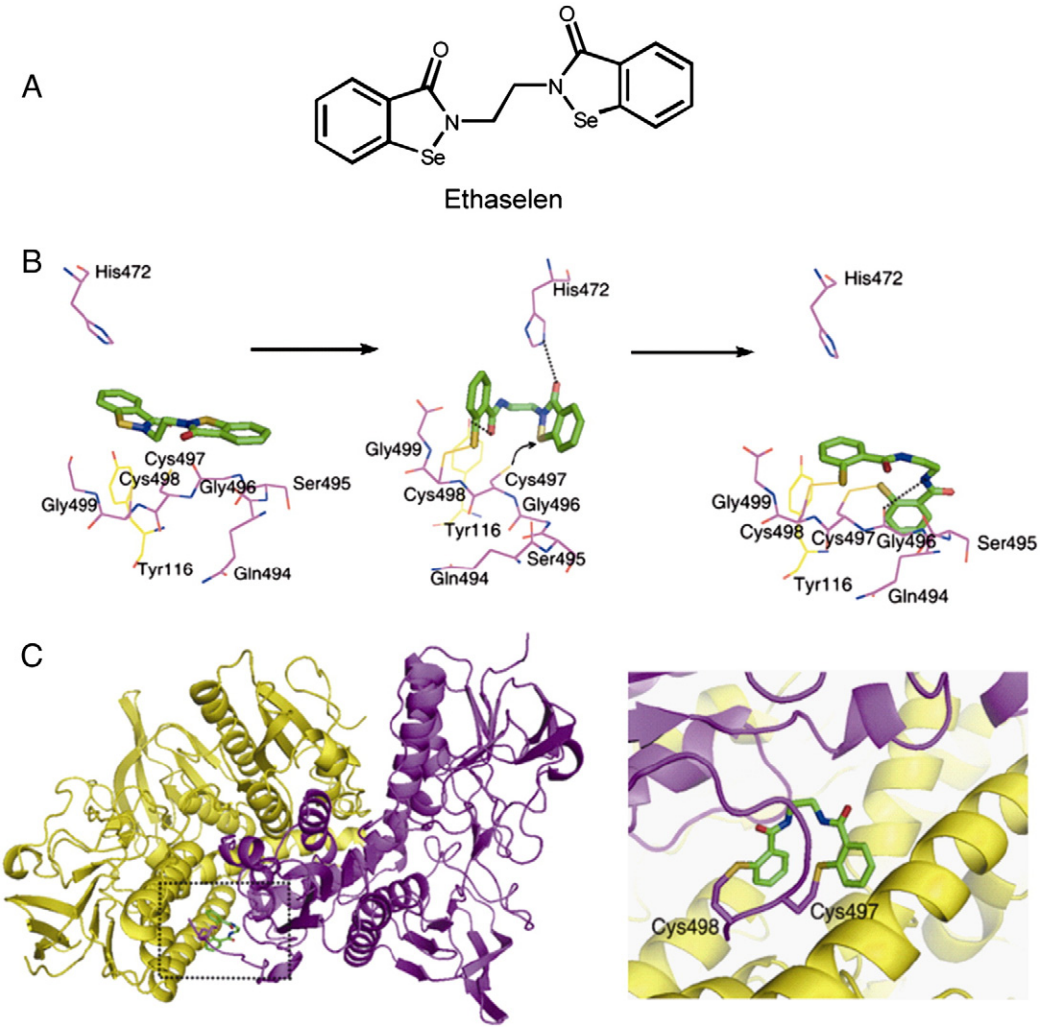

Fig. 1. Molecular dynamic simulation of ethaselen targeting the C-terminal active site of mammalian TrxR1 (rat, PDB ID: 1H6V). (A) Chemical structure of ethaselen. (B) Molecular dynamic simulation and mechanistic optimization of the interaction of ethaselen with the C-terminal active site of TrxR1 (arrows indicate the process). Ethaselen first approaches Cys497/Cys498 (Cys497/Sec498 in the wild-type enzyme) (left). One benzisoselenazol ring is initially attacked by the nucleophilic Cys498 (Sec498 in the wild-type enzyme), forming an intermolecular S–Se bond (Se–Se in the wild-type enzyme). Owing to the first benzisoselenazol ring being opened, ethaselen becomes more flexible and can find a position to interact with Cys497 with its second benzisoselenazol ring. This facilitates the nucleophilic attack by Cys497 (middle) and finally leads to the second S–Se bond between the enzyme and ethaselen (right). (C) Overview of the predicted ethaselen–TrxR complex. The two TrxR subunits are shown in purple and yellow (left). The right shows an enlargement of the TrxR C-terminal redox center, where ethaselen forms two covalent bonds with the active-site residues Cys497 and Cys498 (Cys497 and Sec498 in the wild-type enzyme).

Sec has a higher nucleophilicity compared to Cys under physiological conditions [16], Sec498 preferably attacks the Se–N bond of ethaselen and forms the first intermolecular bond with ethaselen, a diselenide bond (Se–Se). The opening of the benzisoselenazol ring confers a higher flexibility to the ethaselen molecule, allowing ethaselen to get closer to Cys497 (within a distance of 3.0 Å between the Se atom of ethaselen and the S atom of Cys497) (Fig. 1B). Models of mammalian TrxR1 suggest that the C-terminal Cys497 can interact with the N-terminal Cys59 to form a disulfide within a distance of 3 Å [14]. Therefore we speculated that the thiol group of Cys497 might have the potential to attack the other Se–N bond of ethaselen within a distance of 3.0 Å, thereby forming the second intermolecular bond with ethaselen, this time a selenenylsulfide bond (S–Se). Additionally, molecular dynamics simulation showed that during the binding process ethaselen potentially interacts with the residues His472 and Tyr116 through the formation of hydrogen bonds. Both residues (His472 and Tyr116) were shown to play important roles in the catalytic mechanism of TrxR1 (Fig. 1B) [48,15]. The complex of ethaselen bound to TrxR1 via intermolecular Se–Se and S–Se bonds is shown in Fig. 1C. Thus, the proposed reaction mechanism for ethaselen is to block simultaneously the adjacent C-terminal active site residues Cys and Sec of TrxR1, which is expected to effectively suppress TrxR1 activity.

Ethaselen potently inhibits isolated mammalian TrxRs

The direct inhibitory effects of ethaselen on mammalian TrxR1 were studied in the DTNB reduction assay, which reflects the disulfide reduction activity of TrxR1 [37]. When prereduced wild-type TrxRs (human placental TrxR1 and rat liver TrxR1) were incubated with various concentrations of ethaselen for 5 min, the DTNB-reducing activity of TrxRs decreased in a concentration-dependent manner (Fig. 2A). Under these conditions, the IC_{50} values were determined to be 0.5 and 0.35 μM for the wild-type human TrxR1 and rat TrxR1, respectively. However, oxidized mammalian TrxR1 without NADPH preincubation remained comparatively insensitive to ethaselen (Supplementary Fig. 1). In a time-dependent inhibition study, human placental TrxR1 was incubated with various concentrations of ethaselen for 15, 30, and 60 min, followed by measuring the enzyme activity both with the DTNB and with the Trx reduction assay. We found decreasing enzyme activity in both assays with increasing incubation time (Fig. 2B). This result indicates that ethaselen also inhibits mammalian TrxR1 in a time-dependent manner possibly by forming a covalent Se–S bond with Cys497 of TrxR (Fig. 1B). Interestingly, this inhibition was >80% reversible by ultrafiltration (data not shown), which might be partially induced by the reduction of the proposed intermolecular Se–S bond by free TrxR1 molecules when the inhibitor is removed. This observation is consistent with our results showing that ethaselen binds reversibly to the thiol group of free cysteine (Supplementary Fig. 2).

To investigate the initial inhibition of TrxR1 by ethaselen, we carried out enzyme kinetic studies on human TrxR1 in the presence of the inhibitor. As shown in Fig. 2C, ethaselen exhibits a mixed-type initial inhibition of human TrxR1 with respect to DTNB. The inhibition constants for ethaselen binding to free enzyme (K_i) and the enzyme–substrate complex (K_{is}) were determined to be 0.022 and 0.087 μM, respectively.

Characterization of TrxR1 substrate properties of ethaselen

Because mammalian TrxR1 has a broad substrate spectrum including many selenium compounds [49], it is of interest to explore the properties of ethaselen as a substrate for mammalian TrxR1. The NADPH oxidation assay was used as a standard method [42]. Only when ethaselen was incubated with high concentrations of human TrxR1 (20 and 40 nM) were decreases in absorbance at 340 nm

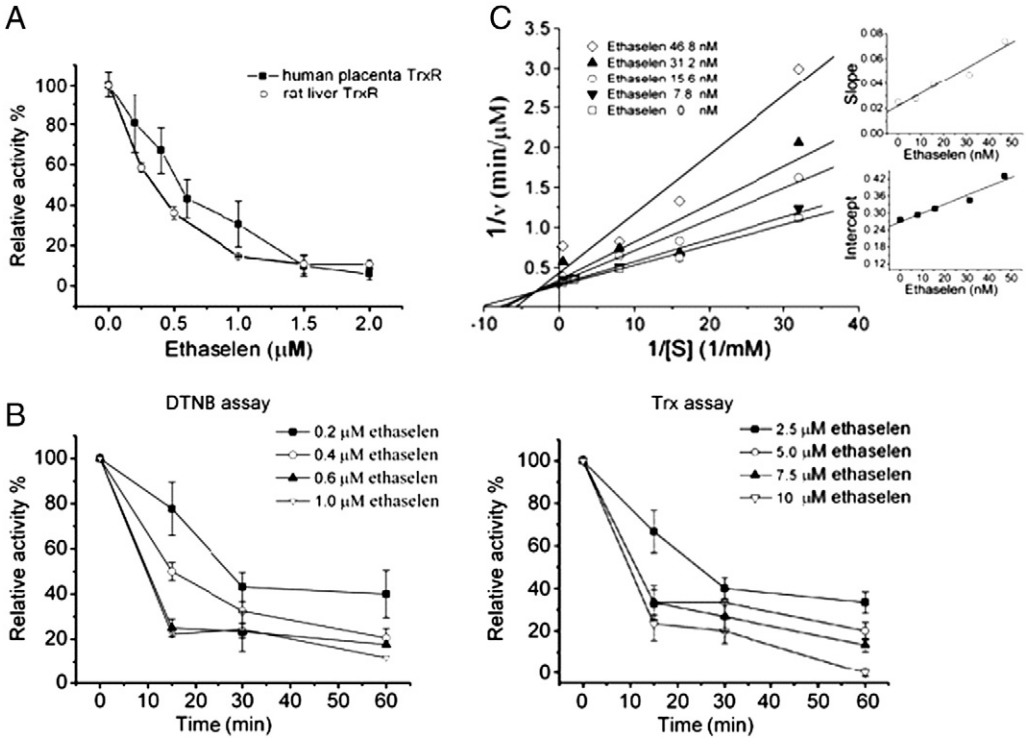

Fig. 2. Mammalian TrxR inhibition by ethaselen. (A) Concentration-dependent inhibition of isolated mammalian TrxRs by ethaselen. NADPH-prereduced human placental TrxR1 and rat liver TrxR1 were incubated with various concentrations of ethaselen for 5 min, followed by the determination of TrxR activity using the DTNB reduction assay. (B) Time-dependent inhibition of isolated human placental TrxR1 by ethaselen. NADPH-prereduced human placental TrxR1 was incubated with various concentrations of ethaselen for various times (15, 30, and 60 min). The remaining enzyme activity was evaluated by both the DTNB reduction assay (left) and the Trx reduction assay (right). (C) Influence of ethaselen on the activity of human TrxR1. The mixed-type inhibition is derived from Lineweaver–Burk plots. The inset graphs show the secondary plots of either slope or intercept of the primary plot versus the concentration of ethaselen for determining the inhibition constants K_i and K_{is}.

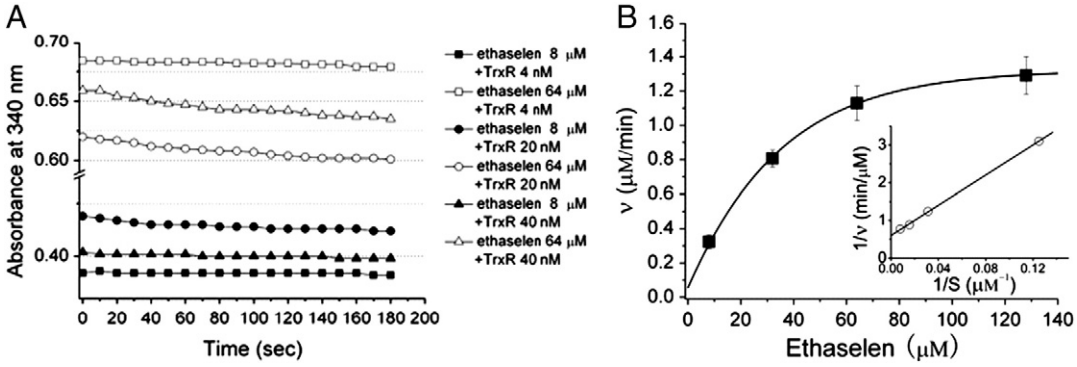

Fig. 3. Ethaselen is a poor substrate for human TrxR1. (A) NADPH oxidation by human TrxR1 in the presence of ethaselen. Various TrxR (4, 20, 40 nM) and ethaselen (8 and 64 μM) concentrations were combined in the assays. The absorbance decrease at 340 nm was detectable only at high concentrations of enzyme and ethaselen. The graph combines data from three independent experiments. (B) The steady-state kinetic analysis of ethaselen as a substrate of human placental TrxR1. The inset graph shows the corresponding Lineweaver–Burk plot. Data are shown as mean values ± SD of three independent experiments.

observed (Fig. 3A). A direct reaction between NADPH and ethaselen at the concentrations used in this experiment was ruled out. As shown in Fig. 3B, ethaselen theoretically exhibits a K_m value of 33.2 μM and a k_{cat} value of 415 min^{-1}; the k_{cat}/K_m value was calculated to be $0.21\times10^6\ M^{-1}\ s^{-1}$. As reported in previous studies, thioredoxin, the native substrate of TrxR, and other well-known selenium-containing TrxR substrates have lower K_m values (2.5–18 μM) and higher k_{cat}/K_m values ($0.778–20\times10^6\ M^{-1}\ s^{-1}$) compared to ethaselen (Supplementary Table 1).

To study if indeed reduced ethaselen was produced in the above assays, we adapted a DTNB-coupled assay to spectrophotometrically detect its existence (see Materials and methods, Enzyme assays). However, we did not observe significantly different absorbances of samples compared with controls, even in the sample with the highest concentrations of ethaselen and human TrxR1 and 60 min incubation. This indicates that there is no detectable free selenothiol pool after the incubation of ethaselen with human TrxR1 in the presence of NADPH. Thus, the postulated reduced forms of ethaselen are not identified under these conditions. Of course, we cannot rule out the possibilities that the reduced forms of ethaselen exist transiently during their binding to mammalian TrxR1 or that the reduced forms of ethaselen are not stable. As discussed below, we attribute the phenomenon of ethaselen-induced NADPH oxidation to an enhanced NADPH oxidase activity of TrxR at the N-terminal active site and/or the FAD that is induced by the presence of the inhibitor.

The C-terminal active site of mammalian TrxR1 is targeted by ethaselen

Mammalian TrxR1 has two redox-active sites, one is located at the N-terminus (Cys59/Cys64) and the other at the C-terminus (Cys497/Sec498) [14,15]. Reducing equivalents are picked up at the N-terminal redox-active site by the redox center of the C-terminal arm, which then reduces the substrates [15]. Therefore, in principle, blocking either the N-terminal or the C-terminal active site could lead to inactivation of the enzyme.

We studied the inhibitory properties of ethaselen on two human (h) TrxR1 mutants and on human glutathione reductase in comparison to wild-type TrxR1 to characterize the inhibitory specificity of ethaselen and determine its target site. The following recombinant enzymes were tested: (i) a hTrxR1 (Sec498 → Cys), (ii) a hTrxR1 mutant truncated by the last two amino acids (Sec–Gly truncated), and (iii) wild-type human GR (Fig. 4). In the case of the hTrxR1 Sec498 → Cys mutant, only very high concentrations of ethaselen (more than 80 μM incubated for 10 min) inhibited the DTNB reduction activity of this protein. This indicates that the Sec498 → Cys hTrxR1 mutant is much less sensitive to ethaselen compared to the wild-type hTrxR1 (Fig. 2A) and implies that the Sec residue is important for the inhibitory mechanism of ethaselen on mammalian wild-type TrxR1. The Sec–Gly truncated hTrxR1 mutant lacks C-terminal catalytic activity but can reduce DTNB via the intact N-terminal active site [33]. Ethaselen does not inhibit DTNB reduction activity of the truncated hTrxR1 mutant, proving that the N-terminal active site is not involved in the inhibitory mechanism of ethaselen on TrxR1. This is further supported by the finding that human GR, which lacks the 16 amino acids at the C-terminus of mammalian TrxR but retains the N-terminal active site [12,13], is not inhibited in the presence of ethaselen at concentrations up to 120 μM. In addition to enzyme inhibition studies, mass spectrometry analysis of ethaselen binding to mammalian TrxR1 has substantiated that the C-terminal active site of mammalian TrxR1 is the targeting site of ethaselen (Supplementary Fig. 3). Taken together, these results suggest that ethaselen specifically targets the C-terminal redox-active site of mammalian TrxR1.

Ethaselen suppresses A549 cell viability and specifically inhibits intracellular TrxR1 activity

The influence of ethaselen on the intracellular TrxR/Trx system and its anticancer effects were investigated in the human lung adenocarcinoma epithelial cell line A549, which is characterized by an elevated TrxR1 expression level and enhanced TrxR1 activity [50]. As shown in Fig. 5A, ethaselen suppressed A549 cell viability in

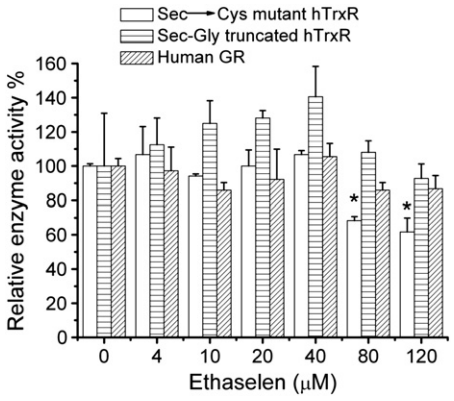

Fig. 4. Inhibitory specificity of ethaselen. 4 nM human GR, 0.1 μM recombinant TrxR1 (Sec498→Cys) and 0.1 μM Sec–Gly truncated human TrxR1 were prereduced by NADPH and incubated with various concentrations of ethaselen for 10 min. The activity of the human TrxR1 variants and GR was measured by the DTNB reduction assay and the GSSG reduction assay, respectively. All data points are shown as means ± SD of three independent experiments. Data for wild-type hTrxR are not included in the diagram because the enzyme is inhibited by >99% at the lowest ethaselen concentration used here. *Statistically significant difference, $P<0.05$.

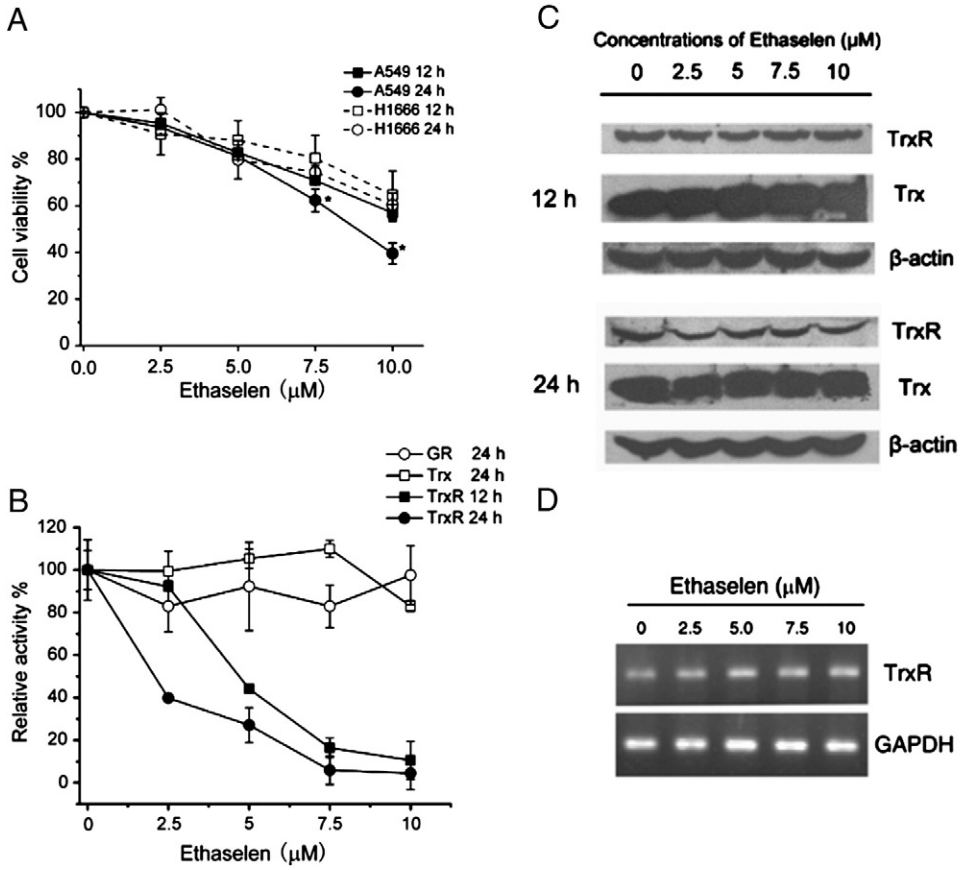

Fig. 5. Ethaselen suppresses A549 cancer cell viability and specifically inhibits intracellular TrxR1 activity. (A) A549 cells and H1666 cells (control, with low TrxR1 expression) were cultured in the presence of various ethaselen concentrations for 12 and 24 h. Cell viability was determined at the end of the incubation time by the MTT assay. *Statistically significant difference between A549 and H1666 cell lines incubated with ethaselen for 24 h ($P<0.05$) (B) Determination of intracellular TrxR1 and GR activities as well as the disulfide reduction capability of Trx in ethaselen-treated A549 cells. The intracellular TrxR activity was measured by the Trx-dependent insulin reduction assay in cells exposed to ethaselen for 12 or 24 h. GR activity was measured by the GSSG reduction assay, and the disulfide reduction capability of Trx was determined by the insulin reduction assay in 24-h ethaselen-treated cells. (C) Western blot analysis of cellular TrxR1 and Trx expression in A549 cells treated for 12 and 24 h with ethaselen. β-Actin was used as control. (D) The mRNA level of TrxR1 in ethaselen-treated A549 cells. Glyceraldehyde-3-phosphate dehydrogenase (GAPDH) was set as the control. All data points are shown as a mean ± SD of three independent experiments.

a both concentration- and time-dependent manner. In direct comparison with the A549 cells, another human lung cancer cell line, namely H1666, which has considerably lower TrxR1 expression levels compared to A549 cells [51], was less susceptible to 24 h treatment with ethaselen. This result indicates that the suppression of cell viability by ethaselen is indeed related to the inhibition of TrxR1 activity.

In parallel, we determined the intracellular TrxR1 activity in the corresponding A549 cells using the Trx-dependent insulin reduction assay [38]. As expected, ethaselen inhibited the intracellular TrxR1 activity in a concentration- and time-dependent manner, with IC_{50} values of 4.2 and 2 μM for 12- and 24-h treatments, respectively (Fig. 5B). The strong inhibitory effect of ethaselen on intracellular TrxR1 activity is consistent with the observations on isolated TrxR1 reported above (Fig. 2). Because ethaselen reacts with cysteines (Supplementary Fig. 2), the inhibitory effect of ethaselen on Trx, which uses a CxxC redox motif to reduce downstream molecules [45], was also measured to fully evaluate the effects of ethaselen on the intracellular TrxR/Trx system. By using a TrxR-dependent insulin reduction assay (see Materials and methods), we found that in the presence of additive active TrxR, the disulfide reduction capability of intracellular Trx was not significantly influenced by the exposure of A549 cells to ethaselen for 24 h (Fig. 5B). This result suggests that the intracellular Trx pool remains intact during ethaselen treatment. In fact, only around 20% insulin-reduction activity was lost in the sample treated with 10 μM ethaselen (Fig. 5B). In addition to the TrxR/Trx system, the intracellular glutathione reductase activity was measured in the ethaselen-treated A549 cells. In agreement with the results reported above on isolated glutathione reductase, intracellular glutathione reductase activity was not inhibited by ethaselen in concentrations up to 10 μM (Fig. 5B).

Furthermore, Western blot analysis was used to investigate the protein levels of TrxR1 and Trx in response to ethaselen treatment of A549 cells. We found that the protein amounts of TrxR1 and Trx were unchanged after both 12 and 24 h of drug treatment (Fig. 5C). The mRNA level of TrxR1 did not show significant alteration in ethaselen-treated A549 cells, either (Fig. 5D). Taken together, these results confirm that ethaselen inhibits intracellular TrxR1 activity by directly targeting the protein and not by changing levels of transcription or translation or by enhancing degradation of the enzyme.

Ethaselen causes intracellular Trx oxidation

The downstream effects of the TrxR system are largely dependent on the reduced form of Trx, which is maintained by intact TrxR in vivo [1]. Therefore it is critical to investigate the intracellular Trx redox status in response to ethaselen treatment. First, A549 cells were cultured for 1 to 24 h in the absence (control) or presence of 10 μM ethaselen (a concentration that markedly reduces cell viability and intracellular TrxR1 activity). Then we analyzed the amount of reduced and oxidized Trx in cell extracts by redox Western blots. In the untreated sample we detected a strong signal representing the

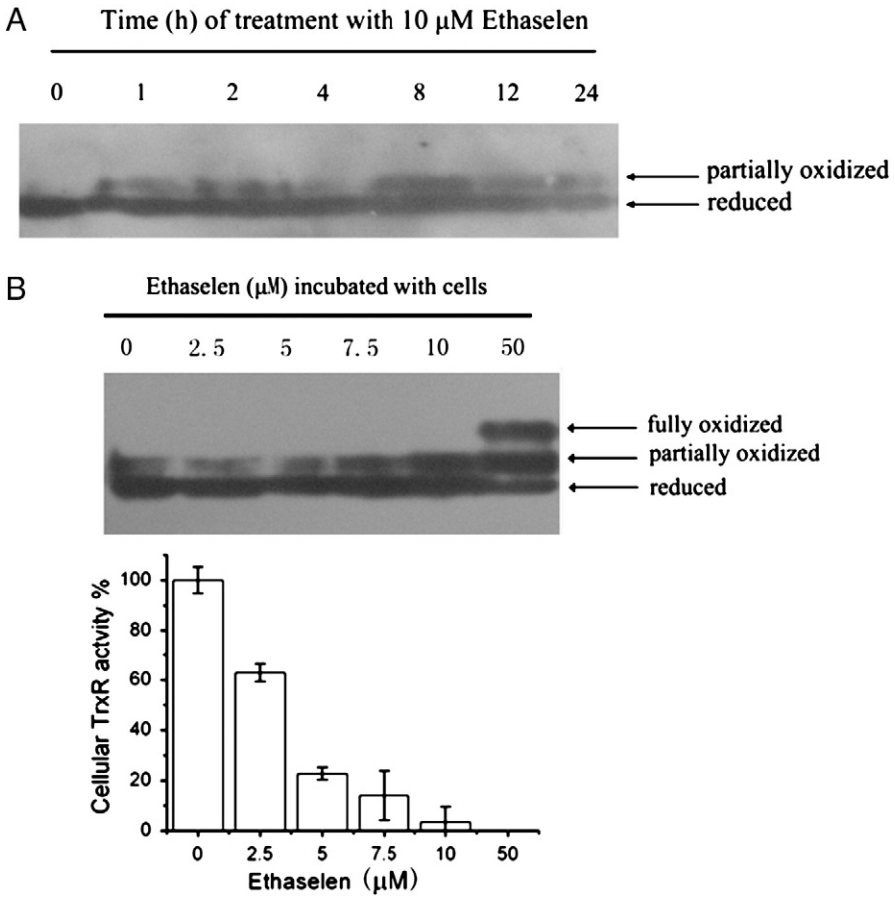

Fig. 6. Ethaselen causes intracellular Trx oxidation in A549 cancer cells. Redox Western blots were used to detect the reduced, partially oxidized (oxidation at Cys32/Cys35), and fully oxidized (oxidation at Cys32/Cys35 and Cys62/Cys69) Trx. (A) Trx oxidation in A549 cells caused by exposure to 10 μM ethaselen for 1 to 24 h. (B) Intracellular Trx is dose-dependently oxidized by ethaselen when A549 cells are incubated with increasing concentrations of ethaselen (0–50 μM) for 2.5 h. Below the Western blot, the inhibitory effects of ethaselen on intracellular TrxR1 activity in the corresponding A549 cells are shown.

reduced form of Trx (Fig. 6A). For cells treated with 10 μM ethaselen, partially oxidized Trx could be detected in all samples independent of the time of exposure to ethaselen (Fig. 6A). This indicates that ethaselen rapidly causes Trx oxidation in A549 cells. Furthermore the dose effect of ethaselen on Trx oxidation was investigated by treating A549 cells with various concentrations of ethaselen for 2.5 h. As shown in Fig. 6B, the ratio of reduced Trx to partially oxidized Trx clearly decreases together with an increase in the concentration of ethaselen. In cells treated with the highest concentration of ethaselen (50 μM), the third (highest) band represents fully oxidized Trx (Fig. 6B). These data indicate that ethaselen causes intracellular Trx oxidation in a concentration-dependent manner.

To explore the role of TrxR1 inhibition in ethaselen-induced cellular Trx oxidation, the intracellular TrxR1 activity was measured in A549 cells with identical drug treatment (same concentrations, 2.5 h incubation). The results clearly show that TrxR1 is inactivated by ethaselen in a concentration-dependent manner in parallel with Trx oxidation (Fig. 6B). Thus, it is likely that the observed accumulation of oxidized Trx in ethaselen-treated cells is indeed a downstream effect of TrxR1 inhibition by ethaselen.

Ethaselen enhances formation of ROS in A549 cells

The TrxR/Trx system plays an important role in the defense against oxidative stress [3,4]. It is therefore of interest to study whether ethaselen influences the level of ROS in cancer cells. A549 cells were incubated with 5 or 10 μM ethaselen for 12 or 24 h and then the ROS levels were determined by a fluorescence method using DCFH-DA. We detected a clear concentration-dependent increase in ROS levels in ethaselen-treated cells compared to untreated cells (Fig. 7), indicating that ethaselen increases ROS levels in A549 cells.

Discussion

In recent years, numerous studies have been conducted in the effort to identify new effective mammalian TrxR1 inhibitors for cancer treatment [9–11,17]. In the present work, we identified the anticancer agent ethaselen as the first selenium-containing inhibitor of mammalian TrxR1, thus extending the scope of mammalian TrxR1 inhibitors. Ethaselen shows a strong inhibitory effect on isolated wild-type mammalian TrxRs with submicromolar IC_{50} values and inhibition constants (Fig. 2). In fact, the inhibitory properties of ethaselen on mammalian TrxRs are comparable with those of some metal-based compounds and alkylating agents that have been reported as TrxR1 inhibitors [17]. Even more importantly, we found that inhibition of mammalian TrxR1 by ethaselen is achieved through specific targeting of the C-terminal active-site residues (Fig. 4). The accessible C-terminal redox site with its adjacent amino acids Cys and Sec provides an excellent target for the development of specific TrxR inhibitors in mammals [4,9]. We proved that ethaselen targets the C-terminal active site of hTrxR1 by showing that hTrxR mutants lacking the selenocysteine, as well as human GR, *E. coli* TrxR, and human glutathione peroxidase (GSH-Px; isolated from erythrocytes), are comparatively insensitive to ethaselen treatment (Fig. 4, data for *E. coli* TrxR and GSH-Px not shown). Human GR is very similar to

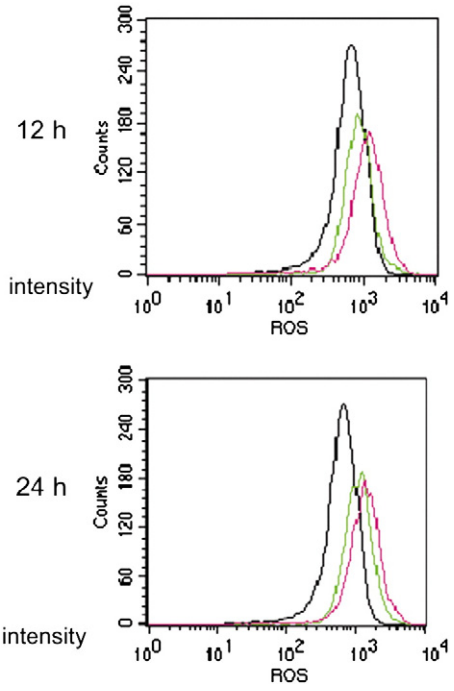

Fig. 7. ROS levels are increased in ethaselen-treated A549 cancer cells. A549 cells were cultured in the presence of 5 and 10 μM ethaselen for 12 and 24 h. The intracellular ROS levels were measured by flow cytometry using the intracellular fluorescent dye DCFH-DA. Black, control (without addition of ethaselen); green, cells treated with 5 μM ethaselen; pink, cells treated with 10 μM ethaselen. Graphs summarize data of three independent experiments.

human TrxR in structure and function but lacks the C-terminal arm with the Sec-containing redox center. Also *E. coli* TrxR, a low-molecular-weight TrxR, utilizes only Cys residues in its active site. GSH-Px is another important human selenoprotein that possesses Sec in the active site but not in a Cys–Sec redox motif [52]. Taken together the data support the notion that the unique hTrxR1 Cys–Sec redox motif is crucial for effective enzyme inhibition by ethaselen.

This study on ethaselen provides evidence for a novel anticancer mechanism of selenium compounds based on mammalian TrxR1 inhibition. It is known that selenium metabolism, mainly regulated by mammalian TrxR1, plays a central role in the anticancer and chemopreventive effects of selenium compounds [49,53]. For example, well-studied chemopreventive selenium compounds such as selenite, selenodiglutathione, and methylseleninate, are excellent substrates of mammalian TrxR1 [54–56]. The resulting reactive selenium metabolites (e.g., CH_3–SeOH) play important roles in selenium-induced cytotoxicity and apoptosis in cancer cells, but also have toxic side effects on normal cells [23,49]. Although there is an assumption that some selenium compounds probably inhibit mammalian TrxR1 by forming a transient Se–Se bond with Sec498 [53], those selenium compounds have only a weak inhibitory effect on TrxR1 activity [49,56]. In fact, it is even more likely that these selenium compounds enhance TrxR1 expression and activity by their incorporation into selenoprotein biosynthesis [53]. In contrast, here we provide evidence that ethaselen exerts its anticancer effects mainly through direct TrxR1 inhibition and not through its metabolism by TrxR1 as reported for other chemopreventive selenium compounds. This is most likely achieved through the unique structural features of ethaselen, combining two reaction sites in one molecule. The two reaction sites offer the potential that once an intermolecular Se–Se bond is formed between Sec498 of TrxR1 and the first pharmacophore of ethaselen, the second pharmacophore of ethaselen can gain close access to Cys497, forming a second bond (Se–S) with the enzyme. Binding of ethaselen to both the attacking and the resolving C-terminal active-site residues of TrxR1 ensures that TrxR1 cannot resolve the binding to ethaselen as easily as in the case of other selenium substrates (Fig. 1); thus ethaselen triggers significant TrxR1 inhibition (Fig. 2). Moreover, the proposed interaction of ethaselen with both C-terminal active-site residues of TrxR1 provides an explanation for its special inhibitory features: the thiol group (–SH) of Cys497 exhibits a lower nucleophilicity compared to the selenol moiety (–SeH) of Sec498, so that the formation of the intermolecular selenylsulfide bond (S–Se) between Cys497 and ethaselen should be much slower compared to the formation of the intermolecular diselenide bond (Se–Se) [16,47]. This hypothesis is supported by the time-dependent inhibition of TrxR1 by ethaselen (Fig. 2B). In the initial TrxR1 inhibition assays, ethaselen was shown to be a mixed-type inhibitor rather than a pure competitive inhibitor, although it interacts with the active site of mammalian TrxR1 (Fig. 2C). This phenomenon might be explained by the involvement of the above-mentioned covalent interaction of ethaselen with TrxR1. This interaction adds to the complexity of the kinetics of the initial TrxR1 inhibition. Furthermore, the hypothesis is in accordance with the fact that the binding of ethaselen to TrxR1 shows some reversibility (Fig. 3). According to this hypothesis Cys497 has the potential to break the Se–Se bond before an intermolecular bond between Cys497 and ethaselen is formed. This would lead to the release of ethaselen. In addition, free TrxR molecules might contribute to the reduction and the release of ethaselen.

Concerning the putative substrate properties of ethaselen it should be taken into account that ethaselen inhibits TrxR1 at nanomolar concentrations; thus it is unlikely that ethaselen acts as a real substrate at the C-terminal redox center. One must rather hypothesize that the enzyme activity detected in the presence of higher micromolar ethaselen concentrations is based on a nonspecific reduction at the N-terminal active site and/or an enhanced NADPH oxidase activity induced in TrxR by the inhibitor. This phenomenon has been previously observed for TrxR inhibitors binding to the C-terminal redox center [33].

In A549 cells, ethaselen can effectively suppress cell viability and specifically inactivate intracellular TrxR1 without influencing GR activity and the disulfide reduction capability of Trx (Figs. 5A and B). There was the concern that the highly abundant glutathione (GSH) in cancer cells may alleviate the inhibitory effects on TrxR1 because of the reactivity of ethaselen toward cysteine (Supplementary Fig. 2). However, we observed that ethaselen retains about 80% of its TrxR1 inhibition potential in the presence of 1 mM GSH in a cell-free system (data not shown). Taking this together with our results on GR and Trx in vivo, it seems that the interaction between ethaselen and TrxR1 in complex cellular systems is highly selective and specific. Supporting this, the results show that in A549 cells ethaselen maintains its low IC_{50} values for effective intracellular TrxR1 inhibition (4.2 and 2 μM for 12 and 24 h treatment, respectively). We also ruled out the possibility that ethaselen reduces TrxR1 activity in A549 cells through alterations in TrxR1 expression (Figs. 5C and D), further supporting our hypothesis that ethaselen directly inhibits the intracellular TrxR1 activity. It should, however, be mentioned that in a recent comparative study ethaselen down-regulated TrxR1 mRNA transcript levels and protein expression in poorly differentiated colorectal RKO cells; in moderately differentiated colorectal LoVo cells this phenomenon was not observed [57]. This observation has been linked to a potential additional mechanism of action affecting the cell growth of poorly differentiated cells [57].

It is noteworthy that we detected rapid oxidation of Trx in ethaselen-treated human lung cancer A549 cells. The intracellular Trx pool was detected to be partially or even fully oxidized in A549 cells along with TrxR1 inactivation in a concentration-dependent manner (Fig. 6). We noticed that under high concentrations of ethaselen that completely inhibit TrxR1 activity, intracellular Trx is still partially in reduced form. A similar phenomenon has been reported for HeLa cancer cells in which intracellular TrxR1 was

knocked down or pharmaceutically inactivated [58]. One possible reason for this observation is that there might be alternative, e.g., glutathione-dependent, Trx-reducing pathways in the cells, as proposed previously for *Arabidopsis* [59]. Because reduced Trx is an essential redox regulator of many key cellular proteins that control important biological functions, a decrease in the reduced Trx pool will, in principle, disturb the downstream effects of the TrxR/Trx system [1]. For example, a recent study showed that ethaselen induces cell apoptosis through the nuclear factor-κB (NF-κB) signaling pathway in A549 cells [44]. It is known that the DNA-binding activity of NF-κB is activated under the redox control of Trx by forming a complex with reduced thioredoxin through an intermolecular disulfide bond between Cys62 of NF-κB and Cys32 of thioredoxin [60]. Accumulation of oxidized Trx in ethaselen-treated A549 cells may therefore lead to a deficiency of NF-κB activation, subsequently triggering NF-κB-dependent apoptosis. This mechanism was proposed to be important for the in vivo antitumor effect of ethaselen observed for the A549-grafted nude mouse model [30]. Another recent work reported that loading ethaselen into polymeric micelles improves the accumulation of ethaselen in tumor tissues, which adds to the in vivo efficacy of ethaselen [61]. Considering that many tumor cells depend on elevated TrxR1 activity for their rapid proliferation [1,7,8], together with the facts that ethaselen is a specific TrxR1 inhibitor and that it can be targeted to tumor tissue, ethaselen shows promising properties that could be used in cancer therapy.

In this study, ethaselen was also shown to increase the intracellular ROS levels in A549 cells (Fig. 7). Recently, it was reported that selenium-deficient TrxR1 variants (e.g., formed by modification of the Sec residue with Sec-specific inhibitors) that retain an active N-terminal active site (called SecTRAPs) can markedly increase ROS levels in cancer cells and induce apoptosis [33]. As described above, ethaselen selectively blocks the C-terminal active site of mammalian TrxR1 without affecting the N-terminal active site (Fig. 4), and therefore it is possible that the increase in cellular ROS levels detected after ethaselen treatment in A549 cells is due to the generation of SecTRAPs from TrxRs by ethaselen. Furthermore, it was suggested that the antioxidant enzyme TrxR1 confers protection on cancer cells against oxidative stress (e.g., ionizing radiation)-induced cell death by scavenging intracellular ROS [62,63]. Thus several studies have focused on TrxR1 as a clinically relevant target of radiosensitizers for cancer radiotherapy [64,65]. A very recent study supports this point of view, showing that pretreatment of two non-small-cell lung cancer (NSCLC) cell lines, A549 and H1299, with ethaselen lowered the TrxR1 activity and enhanced the radioactive sensitivity both in vivo and in vitro [51]. Therefore, ethaselen might also be useful as a radiosensitizer in the treatment of NSCLC.

In conclusion, this is the first time a selenium-containing inhibitor of mammalian TrxR1 has been described and thoroughly characterized. We provide evidence that ethaselen specifically inhibits mammalian TrxR1 and thus blocks the cellular TrxR/Trx system in vivo, finally leading to the observed anticancer effects. In this work we also present a model of a novel interaction mechanism of a selenium compound with mammalian TrxR1. Taken together, our results provide evidence that selenium compounds targeting mammalian TrxR1 could be promising drug candidates for cancer chemotherapy and with ethaselen we provide a template for future drug design approaches.

Acknowledgments

We thank the Drug Design Center for high-performance computing at the Peking University Health Science Center. This work was supported by the National Natural Science Foundation (30472036) of China and the Deutsche Forschungsgemeinschaft (Be 1540/11-1 to K.B.).

Appendix A. Supplementary data

Supplementary data to this article can be found online at doi:10.1016/j.freeradbiomed.2011.11.034.

References

[1] Arnér, E. S.; Holmgren, A. The thioredoxin system in cancer. *Semin. Cancer Biol.* **16:** 420–426; 2006.
[2] Selenius, M.; Rundlöf, A. K.; Olm, E.; Fernandes, A. P.; Björnstedt, M. Selenium and the selenoprotein thioredoxin reductase in the prevention, treatment and diagnostics of cancer. *Antioxid. Redox Signal.* **12:**867–880; 2010.
[3] Williams Jr., C. H. Lipoamide dehydrogenase, glutathione reductase, thioredoxin reductase, and mercuric ion reductase—a family of flavoenzyme transhydrogenases. In: Müller, F. (Ed.), Chemistry and Biochemistry of Flavoenzymes, vol. 3. CRC Press, Boca Raton,pp. 121–211; 1992.
[4] Arnér, E. S. Focus on mammalian thioredoxin reductases—important selenoproteins with versatile functions. *Biochim. Biophys. Acta* **1790:**495–526; 2009.
[5] Gromer, S.; Urig, S.; Becker, K. The thioredoxin system—from science to clinic. *Med. Res. Rev.* **24:**40–89; 2004.
[6] Eriksson, S. E.; Prast-Nielsen, S.; Flaberg, E.; Szekely, L.; Arnér, E. S. High levels of thioredoxin reductase 1 modulate drug-specific cytotoxic efficacy. *Free Radic. Biol. Med.* **47:**1661–1671; 2009.
[7] Yoo, M. H.; Xu, X. M.; Carlson, B. A.; Gladyshev, V. N.; Hatfield, D. L. Thioredoxin reductase 1 deficiency reverses tumor phenotype and tumorigenicity of lung carcinoma cells. *J. Biol. Chem.* **281:**13005–13008; 2006.
[8] Yoo, M. H.; Xu, X. M.; Carlson, B. A.; Patterson, A. D.; Gladyshev, V. N.; Hatfield, D. L. Targeting thioredoxin reductase 1 reduction in cancer cells inhibits self-sufficient growth and DNA replication. *PLoS One* **2:**e1112; 2007.
[9] Pennington, J. D.; Jacobs, K. M.; Sun, L.; Bar-Sela, G.; Mishra, M.; Gius, D. Thioredoxin and thioredoxin reductase as redox-sensitive molecular targets for cancer therapy. *Curr. Pharm. Des.* **13:**3368–3377; 2007.
[10] Smart, D. K.; Ortiz, K. L.; Mattson, D.; Bradbury, C. M.; Bisht, K. S.; Sieck, L. K.; Brechbiel, M. W.; Gius, D. Thioredoxin reductase as a potential molecular target for anticancer agents that induce oxidative stress. *Cancer Res.* **64:**6716–6724; 2004.
[11] Tonissen, K. F.; Di Trapani, G. Thioredoxin system inhibitors as mediators of apoptosis for cancer therapy. *Mol. Nutr. Food Res.* **53:**87–103; 2009.
[12] Arscott, L. D.; Gromer, S.; Schirmer, R. H.; Becker, K.; Williams Jr., C. H. The mechanism of thioredoxin reductase from human placenta is similar to the mechanisms of lipoamide dehydrogenase and glutathione reductase and is distinct from the mechanism of thioredoxin reductase from Escherichia coli. *Proc. Natl. Acad. Sci. U. S. A.* **94:**3621–3626; 1997.
[13] Zhong, L. W.; Arnér, E. S.; Holmgren, A. Structure and mechanism of mammalian thioredoxin reductase: the active site is a redox-active selenolthiolyselenenylsulfide formed from the conserved cysteine–selenocysteine sequence. *Proc. Natl. Acad. Sci. U. S. A.* **97:**5854–5859; 2000.
[14] Sandalova, T.; Zhong, L. W.; Lindqvist, Y. L.; Holmgren, A.; Schneider, G. Three-dimensional structure of a mammalian thioredoxin reductase: implications for mechanism and evolution of a selenocysteine-dependent enzyme. *Proc. Natl. Acad. Sci. U. S. A.* **98:**9533–9538; 2001.
[15] Cheng, Q.; Sandalova, T.; Lindqvist, Y.; Arnér, E. S. Crystal structure and catalysis of the selenoprotein thioredoxin reductase 1. *J. Biol. Chem.* **284:**3998–4008; 2009.
[16] Arnér, E. S. Selenoproteins—what unique properties can arise with selenocysteine in place of cysteine? *Exp. Cell Res.* **316:**1296–1303; 2010.
[17] Urig, S.; Becker, K. On the potential of thioredoxin reductase inhibitors for cancer therapy. *Semin. Cancer Biol.* **16:**452–465; 2006.
[18] Zeng, H. H.; Wang, L. H. Targeting thioredoxin reductase: anticancer agents and chemopreventive compounds. *Med. Chem.* **6:**286–297; 2010.
[19] Hashemy, S. I.; Ungerstedt, J. S.; Avva, F. Z.; Holmgren, A. Motexafin gadolinium, a tumor-selective drug targeting thioredoxin reductase and ribonucleotide reductase. *J. Biol. Chem.* **281:**10691–10697; 2006.
[20] Fang, J.; Lu, J.; Holmgren, A. Thioredoxin reductase is irreversibly modified by curcumin: a novel molecular mechanism for its anticancer activity. *J. Biol. Chem.* **280:**25284–25290; 2005.
[21] Chew, E. H.; Lu, J.; Bradshaw, T. D.; Holmgren, A. Thioredoxin reductase inhibition by antitumor quinols: a quinol pharmacophore effect correlating to antiproliferative activity. *FASEB J.* **22:**2072–2083; 2008.
[22] Lu, J.; Chew, E. H.; Holmgren, A. Targeting thioredoxin reductase is a basis for cancer therapy by arsenic trioxide. *Proc. Natl. Acad. Sci. U. S. A.* **104:**12288–12293; 2007.
[23] Brozmanová, J.; Mániková, D.; Vlčková, V.; Chovanec, M. Selenium: a double-edged sword for defense and offense in cancer. *Arch. Toxicol.* **84:**919–938; 2010.
[24] Shi, C.; Yu, L. Z.; Yang, F. G.; Yan, J.; Zeng, H. H. A novel organoselenium compound induces cell cycle arrest and apoptosis in prostate cancer cell lines. *Biochem. Biophys. Res. Commun.* **309:**578–583; 2003.
[25] Zhao, F.; Yan, J.; Deng, S.; Lan, L.; He, F.; Kuang, B.; Zeng, H. H. A thioredoxin reductase inhibitor induces growth inhibition and apoptosis in five cultured human carcinoma cell lines. *Cancer Lett.* **236:**46–53; 2006.
[26] Xing, F.; Li, S.; Ge, X.; Wang, C.; Zeng, H. H.; Li, D.; Dong, L. The inhibitory effect of a novel organoselenium compound BBSKE on the tongue cancer Tca8113 in vitro and in vivo. *Oral Oncol.* **44:**963–969; 2008.

[27] Peng, Z. F.; Lan, L. X.; Zhao, F.; Li, J.; Tan, Q.; Yin, H. W.; Zeng, H. H. A novel thioredoxin reductase inhibitor inhibits cell growth and induces apoptosis in HL-60 and K562 cells. *J. Zhejiang Univ. Sci. B* **9:**16–21; 2008.
[28] Lin, F.; Zhou, L. N.; Liang, Y.; Lv, L. A study of long term (12 weeks) toxicity test on rats with ethaselen. *J. Basic Clin. Oncol.* **21:**369–373; 2008.
[29] Fu, J. N.; Li, J.; Tan, Q.; Yin, H. W.; Xiong, K.; Wang, T. Y.; Ren, X. Y.; Zeng, H. H. Thioredoxin reductase inhibitor ethaselen increases the drug sensitivity of the colon cancer cell line LoVo towards cisplatin via regulation of G1 phase and reversal of G2/M phase arrest. *Invest. New Drugs* **29:**627–636; 2011.
[30] Tan, Q.; Li, J.; Yin, H. W.; Wang, L. H.; Tang, W. C.; Zhao, F.; Liu, X. M.; Zeng, H. H. Augmented antitumor effects of combination therapy of cisplatin with ethaselen as a novel thioredoxin reductase inhibitor on human A549 cell in vivo. *Invest. New Drugs* **28:**205–215; 2010.
[31] Gromer, S.; Arscott, L. D.; Williams Jr., C. H.; Schirmer, R. H.; Becker, K. Human placenta thioredoxin reductase: isolation of the selenoenzyme, steady state kinetics, and inhibition by therapeutic gold compounds. *J. Biol. Chem.* **273:** 20096–20101; 1998.
[32] Urig, S.; Lieske, J.; Fritz-Wolf, K.; Irmler, A.; Becker, K. Truncated mutants of human thioredoxin reductase 1 do not exhibit glutathione reductase activity. *FEBS Lett.* **580:**3595–3600; 2006.
[33] Anestål, K.; Prast-Nielsen, S.; Cenas, N.; Arnér, E. S. Cell death by SecTRAPs: thioredoxin reductase as a prooxidant killer of cells. *PLoS One* **3:**e1846; 2008.
[34] Bücheler, U. S.; Werner, D.; Schirmer, R. H. Generating compatible translation initiation regions for heterologous gene expression in Escherichia coli by exhaustive periShine–Dalgarno mutagenesis: human glutathione reductase cDNA as a model. *Nucleic Acids Res.* **20:**3127–3133; 1992.
[35] Zhang, H.; Cao, D.; Cui, W.; Ji, M.; Qian, X.; Zhong, L. Molecular bases of thioredoxin and thioredoxin reductase-mediated prooxidant actions of (−)-epigallocatechin-3-gallate. *Free Radic. Biol. Med.* **49:**2010–2018; 2010.
[36] Case, D. A.; Cheatham III, T. E.; Darden, T.; Gohlke, H.; Luo, R.; Merz Jr., K. M.; Onufriev, A.; Simmerling, C.; Wang, B.; Woods, R. J. The Amber biomolecular simulation programs. *J. Comput. Chem.* **26:**1668–1688; 2005.
[37] Luthman, M.; Holmgren, A. Rat liver thioredoxin and thioredoxin reductase: purification and characterization. *Biochemistry* **21:**6628–6633; 1982.
[38] Söderberg, A.; Sahaf, B.; Rosén, A. Thioredoxin reductase, a redox-active selenoprotein, is secreted by normal and neoplastic cells: presence in human plasma. *Cancer Res.* **60:**2281–2289; 2000.
[39] Millet, R.; Urig, S.; Jacob, J.; Amtmann, E.; Moulinoux, J. P.; Gromer, S.; Becker, K.; Davioud-Charvet, E. Synthesis of 5-nitro-2-furancarbohydrazides and their cis-diamminedichloroplatinum complexes as bitopic and irreversible human thioredoxin reductase inhibitors. *J. Med. Chem.* **48:**7024–7039; 2005.
[40] Li, Z. C.; Chen, L. H.; Yu, X. J.; Hu, Y. H.; Song, K. K.; Zhou, X. W.; Chen, Q. X. Inhibition kinetics of chlorobenzaldehyde thiosemicarbazones on mushroom tyrosinase. *J. Agric. Food Chem.* **58:**12537–12540; 2010.
[41] Wang, Y. M.; Qiao, M.; Mieyal, J. J.; Asmis, L. M.; Asmis, R. Molecular mechanism of glutathione-mediated protection from oxidized low-density lipoprotein-induced cell injury in human macrophages: role of glutathione reductase and glutaredoxin. *Free Radic. Biol. Med.* **41:**775–785; 2006.
[42] Lu, J.; Papp, L. V.; Fang, J.; Rodriguez-Nieto, S.; Zhivotovsky, B.; Holmgren, A. Inhibition of mammalian thioredoxin reductase by some flavonoids: implications for myricetin and quercetin anticancer activity. *Cancer Res.* **66:** 4410–4418; 2006.
[43] Bradshaw, T. D.; Matthews, C. S.; Cookson, J.; Chew, E. H.; Shah, M.; Bailey, K.; Monks, A.; Harris, E.; Westwell, A. D.; Wells, G.; Laughton, C. A.; Stevens, M. F. Elucidation of thioredoxin as a molecular target for antitumor quinols. *Cancer Res.* **65:**3911–3919; 2005.
[44] Lan, L. X.; Zhao, F.; Wang, Y.; Zeng, H. H. The mechanism of apoptosis induced by a novel thioredoxin reductase inhibitor in A549 cells: possible involvement of nuclear factor-κB-dependent pathway. *Eur. J. Pharmacol.* **555:** 83–92; 2007.
[45] Watson, W. H.; Pohl, J.; Montfort, W. R.; Stuchlik, O.; Reed, M. S.; Powis, G.; Jones, D. P. Redox potential of human thioredoxin 1 and identification of a second dithiol/disulfide motif. *J. Biol. Chem.* **278:**33408–33415; 2003.
[46] Sun, Y.; Rigas, B. The thioredoxin system mediates redox-induced cell death in human colon cancer cells: implications for the mechanism of action of anticancer agents. *Cancer Res.* **68:**8269–8277; 2008.
[47] Sakurai, T.; Kanayama, M.; Shibata, T.; Itoh, K.; Kobayashi, A.; Yamamoto, M.; Uchida, K. Ebselen, a seleno-organic antioxidant, as an electrophile. *Chem. Res. Toxicol.* **19:**1196–1204; 2006.
[48] Gromer, S.; Wessjohann, L. A.; Eubel, J.; Brandt, W. Mutational studies confirm the catalytic triad in the human selenoenzyme thioredoxin reductase predicted by molecular modeling. *Chembiochem* **7:**1649–1652; 2006.
[49] Lu, J.; Berndt, C.; Holmgren, A. Metabolism of selenium compounds catalyzed by the mammalian selenoprotein thioredoxin reductase. *Biochim. Biophys. Acta* **1790:**1513–1519; 2009.
[50] Soini, Y.; Kahlos, K.; Näpänkangas, U.; Kaarteenaho-Wiik, R.; Säily, M.; Koistinen, P.; Pääakkö, P.; Holmgren, A.; Kinnula, V. L. Widespread expression of thioredoxin and thioredoxin reductase in non-small cell lung carcinoma. *Clin. Cancer Res.* **7:** 1750–1757; 2001.
[51] Wang, L.; Fu, J. N.; Wang, J. Y.; Jin, C. J.; Ren, X. Y.; Tan, Q.; Li, J.; Yin, H. W.; Xiong, K.; Wang, T. Y.; Liu, X. M.; Zeng, H. H. Selenium-containing thioredoxin reductase inhibitor ethaselen sensitizes non-small cell lung cancer to radiotherapy. *Anticancer Drugs* **22:**732–740; 2011.
[52] Lu, J.; Holmgren, A. Selenoproteins. *J. Biol. Chem.* **284:**723–727; 2009.
[53] Ganther, H. E. Selenium metabolism, selenoproteins and mechanisms of cancer prevention: complexities with thioredoxin reductase. *Carcinogenesis* **20:** 1657–1666; 1999.
[54] Kumar, S.; Björnstedt, M.; Holmgren, A. Selenite is a substrate for calf thymus thioredoxin reductase and thioredoxin and elicits a large non-stoichiometric oxidation of NADPH in the presence of oxygen. *Eur. J. Biochem.* **207:**435–439; 1992.
[55] Björnstedt, M.; Kumar, S.; Holmgren, A. Selenodiglutathione is a highly efficient oxidant of reduced thioredoxin and a substrate for mammalian thioredoxin reductase. *J. Biol. Chem.* **267:**28030–28034; 1992.
[56] Gromer, S.; Gross, J. H. Methylseleninate is a substrate rather than an inhibitor of mammalian thioredoxin reductase. *J. Biol. Chem.* **277:**9701–9706; 2002.
[57] Yin, H.; Li, J.; Xiong, K.; Wang, L.; Wang, T.; Tan, Q.; Fu, J.; Ren, X.; Zeng, H. Novel mechanism of ethaselen in poorly differentiated colorectal RKO cell growth inhibition: simultaneous regulation of TrxR transcription, expression and enzyme activity. *Differentiation* **81:**49–56; 2011.
[58] Watson, W. H.; Heilman, J. M.; Hughes, L. L.; Spielberger, J. C. Thioredoxin reductase-1 knock down does not result in thioredoxin-1 oxidation. *Biochem. Biophys. Res. Commun.* **368:**832–836; 2008.
[59] Reichheld, J. P.; Khafif, M.; Riondet, C.; Droux, M.; Bonnard, G.; Meyer, Y. Inactivation of thioredoxin reductases reveals a complex interplay between thioredoxin and glutathione pathways in Arabidopsis development. *Plant Cell* **19:**1851–1865; 2007.
[60] Matthews, J. R.; Wakasugi, N.; Virelizier, J. L.; Yodoi, J.; Hay, R. T. Thioredoxin regulates the DNA binding activity of NF-kappa B by reduction of a disulphide bond involving cys62. *Nucleic Acids Res.* **20:**3821–3830; 1992.
[61] Liu, M.; Fu, J.; Li, J.; Wang, L.; Tan, Q.; Ren, X.; Peng, Z.; Zeng, H. Preparation of triblock copolymer micelles loading novel organoselenium anticancer drug BBSKE and study of tissue distribution of copolymer micelles by imaging in vivo method. *Int. J. Pharm.* **391:**292–304; 2010.
[62] Lim, H. W.; Hong, S.; Jin, W.; Lim, S.; Kim, S. J.; Kang, H. J.; Park, E. H.; Ahn, K.; Lim, C. J. Up-regulation of defense enzymes is responsible for low reactive oxygen species in malignant prostate cancer cells. *Exp. Mol. Med.* **37:**497–506; 2005.
[63] Karimpour, S.; Lou, J.; Lin, L. L.; Rene, L. M.; Lagunas, L.; Ma, X.; Karra, S.; Bradbury, C. M.; Markovina, S.; Goswami, P. C.; Spitz, D. R.; Hirota, K.; Kalvakolanu, D. V.; Yodoi, J.; Gius, D. Thioredoxin reductase regulates AP-1 activity as well as thioredoxin nuclear localization via active cysteines in response to ionizing radiation. *Oncogene* **21:**6317–6327; 2002.
[64] Javvadi, P.; Hertan, L.; Kosoff, R.; Datta, T.; Kolev, J.; Mick, R.; Tuttle, S. W.; Koumenis, C. Thioredoxin reductase-1 mediates curcumin-induced radiosensitization of squamous carcinoma cells. *Cancer Res.* **70:**1941–1950; 2010.
[65] Rockwell, S.; Donnelly, E. T.; Liu, Y.; Tang, L. Q. Preliminary studies of the effects of gadolinium texaphyrin on the growth and radiosensitivity of EMT6 cells in vitro. *Int. J. Radiat. Oncol. Biol. Phys.* **54:**536–541; 2002.